MOVPE Growth and Characterization of Group-III Nitrides Using In Situ Spectroscopic Ellipsometry

vorgelegt von
Diplom-Physiker
Torsten Schmidtling
aus Berlin

Von der
Fakultät II
-Mathematik und Naturwissenschaften-
der Technischen Universität Berlin
zur Erlangung des akademischen Grades

Doktor der Naturwissenschaften

genehmigte Dissertation

Parts of this work have already been published:

T. Schmidtling, S. Peters, U. W. Pohl and W. Richter, J. Appl. Phys. Vol. **98**(3), 33522 (2005): *In situ spectroscopic ellipsometry study of GaN nucleation layer growth and annealing on sapphire in metalorganic vapor phase epitaxy*

P. Ruterana, M. Morales, F. Gourbilleau, P. Singh, M. Drago, W. Richter, T. Schmidtling, phys. stat. sol. (a) Vol. **202**, No.5, 781 (2005): *Effects of annealing and low temperature buffer layer on the properties of InN layers grown by MOVPE*

M. R. Phillips, M. H. Zareie, O. Gelhausen, M. Drago, T. Schmidtling, W. Richter, J. Crys. Growth **269**, 106 (2004): *Scanning tunneling and cathodoluminescence spectroscopy of indium nitride*

M. Drago, T. Schmidtling, U. W. Pohl, S. Peters, W. Richter, phys. stat. sol. (c) Vol. **0**, 2842 (2003): *InN metalorganic vapour phase epitaxy and ellipsometric characterisation*

T. Schmidtling, M. Drago, U. W. Pohl, W. Richter, J. Crys. Growth **248**, 523 (2003): *Spectroscopic ellipsometry during metalorganic vapor phase epitaxy on InN*

M. Drago, T. Schmidtling, U. W. Pohl, W. Richter, EW-MOVPE *X* (Lecce, Italy) ISBN **88-8305-007-X**, (2003): *MOVPE Growth of InN layers and spectroscopic ellipsometry characterization*

C. Cobet, T. Schmidtling, M. Drago, N. Wollschläger, N. Esser, W. Richter, R. M. Feenstra, T. U. Kampen, J. Appl. Phys. Vol. **94**, 6997 (2003): *Surface termination during GaN growth by metalorganic vapor phase epitaxy determined by ellipsometry*

C. Cobet, T. Schmidtling, M. Drago, N. Wollschläger, N. Esser, W. Richter, R. M. Feenstra, phys. stat. sol. (c) Vol. **0**, 2938 (2003): *In-situ ellipsometry: identification of surface terminations during GaN growth*

S. Peters, T. Schmidtling, T. Trepk, U. W. Pohl, J.-T. Zettler, W. Richter, J. Appl. Phys. Vol. **88**, 4007 (2000): *In-situ monitoring of GaN metal-organic vapor phase epitaxy by spectroscopic ellipsometry*

Abstract

MOVPE Growth and Characterization of Group-III Nitrides Using In Situ Spectroscopic Ellipsometry

von

Torsten Schmidtling

Das Ziel dieser Arbeit ist die Untersuchung der Wachstumsmechanismen der Gruppe III-Nitride GaN und InN in der metallorganischen Gasphasenepitaxie (MOVPE) mittels spektroskopischer Ellipsometrie (SE) *in situ*. Dabei ermöglicht SE einen direkten Zugang zu den Materialparametern wie Bandlückenenergie, Bandlückenverbreiterung, Schichtdicken- oder Rauhigkeitsentwicklung bereits während des Wachstumsprozesses. Das Verfolgen der Änderungen dieser Materialparameter in direkter Abhängigkeit der gewählten Wachstumsparameter erlaubt ein tieferes Verständnis der zugrunde liegenden Wachstumsmechanismen und eine gezielte Steuerung des Wachstumsprozesses.

Beim Wachstum von GaN auf Saphir mit einer Gitterfehlanpassung von 16 % hängt die Qualität der epitaktischen Schicht stark von der Präparation des Substrates und der Nukleationsschicht ab. Hier zeigt SE, daß der Nitridierungsprozeß des Saphirs unter Ammoniak bereits bei 800 °C beginnt und sich nach etwa 10 min bei 1060 °C eine kristalline, 4 nm dünne Schicht AlN gebildet hat. Das Nukleationsschichtwachstum selbst kann sehr sensitiv auf die kristalline Zusammensetzung in Abhängigkeit der Wachstumsrate und des V/III Verhältnisses gesteuert werden. Bei der thermischen Nachbehandlung der Nukleationsschicht zum Erreichen der Wachstumstemperatur für die Epitaxieschicht (annealing) wird mit SE eine Phasenumwandlung von kubischem zu hexagonalem GaN beobachtet. Diese ist allerdings mit Erreichen der Schichtwachstumstemperatur abgeschlossen. Eine Langzeitbehandlung verschlechtert die Qualität, die Nukleationsschicht desorbiert. Auch ermöglicht SE die Einflüsse von Umgebungsparametern wie z. B. der Reaktorbelegung zu quantifizieren und die dadurch veränderte Wachstumsrate der Nukleationsschicht zu korrigieren. GaN Epitaxieschichten, die auf so optimierten Nukleationsschichten gewachsen werden, zeigen niedrige Röntgen-Halbwertsbreiten, ausgeprägte Photolumineszenz gebundener und freier Excitonen sowie atomar glatte Oberflächen. Sie sind von hoher Qualität.

Die Untersuchungen des Wachstumsprozesses von InN auf Saphir mittels spektroskopischer Ellipsometrie offenbart deutliche, prinzipielle Schwierigkeiten der InN-Epitaxie. Durch die niedrige Bindungsenergie von InN und die hohe Bindungsenergie des Precursors Ammoniak ensteht ein nur sehr kleines Wachstumsfenster im Bereich von 500 °C unter extrem hohem V/III Verhältnis. Außerdem führt die sehr hohe Gitterfehlanpassung von fast 30 % bereits während der Epitaxie zu spannungsinduzierten Defekten. Diese Defektbildung und die damit verbundene kritische Schichtdicke werden in Folge des Übergangs vom 2-dimensionalen Schichtwachstum zu 3-dimensionalem Inselwachstum bereits in situ durch eine drastische Änderung der Wachstumsrate beobachtet. Schließlich zeigt die effektive dielektrische Funktion von epitaktisch gewachsenem InN eine Absorptionskante bei 1,05 eV sowie drei intensive Strukturen, die höheren Interbandübergängen im Bereich von 4,85 eV, 5,40 eV sowie 6,17 eV zugeschrieben werden. Diese Werte entsprechen in guter Näherung theoretischen Berechnungen der Energien der Übergänge an Symmetriepunkten der Brillouinzone des InN.

Contents

i

Introduction

This work deals with the epitaxial growth and growth characterization of the binary group-III nitrides gallium-nitride (GaN) and indium-nitride (InN) using Spectroscopic Ellipsometry (SE) for growth monitoring. As epitaxial growth is usually performed in metal-organic vapor phase epitaxy (MOVPE) on highly lattice mismatched substrates, a detailed analysis of the growth mechanisms and the growth process requires *in situ* optical techniques. SE is the method of choice here which allows determination of epitaxial layer properties during growth from the sub-nm to micrometer scale. To completely understand the results attained in MOVPE, SE is used for comparison to other growth techniques. Additional experiments are performed in plasma-assisted molecular beam epitaxy (PA)MBE in a vacuum environment to access to the structural properties of the sample surfaces during growth via electron based characterization methods.

The outstanding performances of nitrides such as AlN, GaN and InN has been of major interest to researchers all over the world. They cover a vast spectral range in their band gap energy from 6.2 eV (200 nm) down to approx. 0.7 eV (1770 nm) through alloying making them promising candidates for all kind of optical applications while the "classical" III-V materials as well as the II-VI compounds are limited in their spectral range as shown in Figure 1. For example the use of blue laser diodes in data storage led to an increase in DVD capacity up to 50 GB as demonstrated by Sony corporation this year [1]. Additionally their strong ionicity resulting in high binding energy together with high saturation drift velocities and breakdown voltages enables high power, high frequency operation under extreme conditions up to 300 °C [2, 3]. For more detailed information on III-nitride properties and their applications several comprehensive review articles and textbooks exist [4–10] which also show the steady improvement in material and device quality.

But many questions still have to be solved in the field of III-nitrides growth and their fundamental properties. This concerns the growth mechanisms in heteroepitaxy on highly mismatched substrates such as for the well established material, GaN, grown on sapphire and control of the growth process as well as the determination of the fundamental properties of the "new" material InN. For the latter the energetic position of the band edge is still a subject of discussion. The change from formerly assumed values of 1.8-2.1 eV [11] to the nowadays more accepted 0.6 to 0.8 eV [12, 13] is mostly due
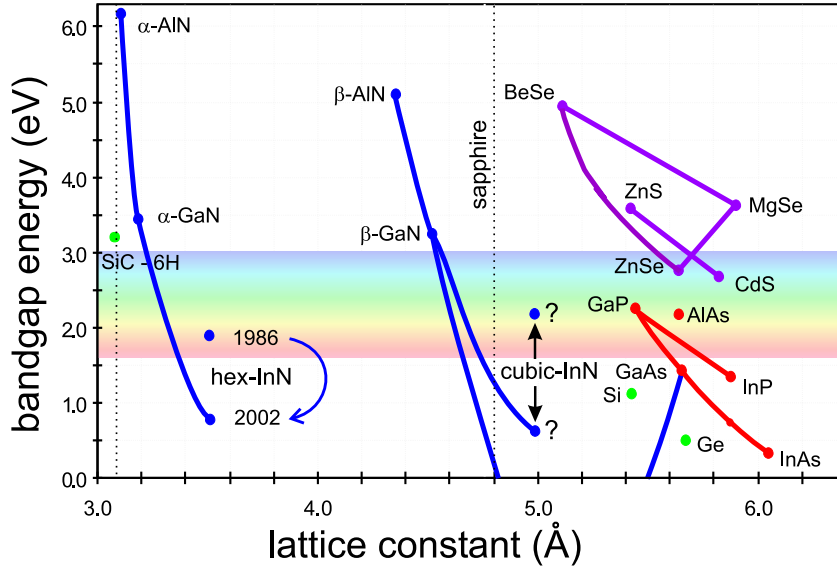
Figure 1: Survey of the most commonly used semiconductors and their fundamental band gap energy vs. lattice constant. While the II-VI compounds cover a spectral range with its centre in the UV, the "classical" III-V´s are more dedicated to the vis-IR range. The group III-nitrides have the capability to do both with InN in the center of interest obviously having a fundamental band gap energy in the IR. Commonly used substrates for nitride heteroepitaxy like SiC and sapphire are included, too. For details of the sapphire lattice and band gap parameters and the epitaxial relationship see chapter 1.

to drastic improvements in epitaxial growth techniques setting oxygen incorporated during growth as the most likely candidate for the large discrepancies [14, 15]. But the layer grown are still highly defective and the situation is reminescent of the early nineties when GaN growth was improving every day.

Additionally the search for non-harmful materials with variable band gap energies for e. g. solar cell applications [16] drives the research in this field. But epitaxial growth problems like the existing miscibility gap in nitride alloying have to be solved to achieve this aim. These unsolved questions and their related problems are the motivation for the work to be done: understanding and thereby improving the nitride growth in MOVPE through gaining detailed insight into the processes on a microscopic to atomic scale and determining the exact material properties, as in the case of InN. Therefore the use of an optical instrument like spectroscopic ellipsometry is one way to observe and investigate the growth in a gaseous environment like MOVPE where electron based methods, such as RHEED or LEED used in MBE, fail. It has been already shown from Nakamura in the early 90's that the use of in-situ techniques for device growth leads to drastic improvements [17, 18] resulting in a world leading position in GaN and InGaN based LED's and LD's growth.

This work is divided in three parts:

The first part gives a short overview on the specialities of group-III nitride growth. Spectroscopic Ellipsometry (SE) as a technique for measuring thin film properties and its application to the growth setup will be described and the evaluation of the measured effective dielectric function will be highlighted with some examples.

In the second part detailed investigations during GaN growth are performed with in-situ SE to analyze the GaN growth procedure. Furthermore SE is used to determine surface conditions in MOVPE via a direct comparison with (PA)MBE growth allowing a detailed insight into surface stoichiometry in MOVPE.

The last part is dedicated to the "novel" material, InN, where again ellipsometry reveals its capability to improve epitaxial growth while simultaneously determining fundamental material properties with high precision.

Finally the fundamental results which can be drawn from *in situ* ellipsometry are summed up.

Chapter 1

Epitaxial growth techniques for group III-Nitrides

Metal Organic Vapor Phase Epitaxy (MOVPE) is the method of choice for high quality mass production of group III-nitrides. This is caused by several reasons: just like MBE MOVPE is capable of growing layer with atomically flat surfaces, sharp interfaces and thicknesses in the range of monolayers. The main advantage beyond MOVPE is the possibility of nearly unlimited up-scaling of the growth environment. While in MBE the molecular beam diameter sets the limits for the maximum wafer size this can be easily expanded in MOVPE. The precursor flux transported through the gas phase can be enhanced while the reactor chamber is enlarged only under consideration of thermodynamic calculations ensuring the suitable temperature profile and decomposition ratio of the precursor. MOVPE growth setups for $95 \times 2''$ wafer size are commercially available [19]. Further advantages are the higher growth rate in MOVPE in the range of 1 to $5\,\mu$m/hour and the easy wafer loading into the reactor compared to the ultra-high vacuum environment in MBE. All this can improve yield in MOVPE easily by an order of magnitude.

Since up to now no homoepitaxial substrates for GaN growth are available for reasonable prices and in useful sizes heteroepitaxy has to be performed on alternative substrates with a high lattice mismatch. That is why the growth method requires a special procedure depending on the substrate used as it is described in more detail in chapter 4. The resulting layer still suffer from a high dislocation density in the range of 10^8/cm^2 (or even more in the case of silicon substrates). The dislocation density cannot be reduced below 10^7/cm^2 even with great epitaxial expenses like low temperature multi-buffer approaches [10, 20] or much below 10^6/cm^2 using epitaxial lateral overgrowth (ELOG, LEO) [21] or PENDEO-epitaxy [22, 23] (which is a similar approach as ELOG but starting from the side walls of a micro structure on the substrate). For comparison: dislocation densities on GaAs or silicon homoepitaxy are as low as 10^2 to

$10^4/cm^2$ or almost zero (F. A. Ponce in [4], p.123). Despite these handicaps the nitrides convince with high optical output, low resistivity and high electron mobility which is mainly due to their high ionicity and small excitonic radii which allow radiative recombination even in the presence of high defect density.

For successful growth of III-nitrides several alternative substrates are available. These are mainly the cheap but non-conductive sapphire (Al_2O_3), conductive silicon-carbide (SiC-6H) or since a few years Si(111) which can be either isolating or p- or n-doped. The main problem besides the lattice mismatch when using silicon as substrate is to prevent the meltback-etching during nitride epitaxy. This can be done by inserting an appropriate inter layer like e.g. AlN or grained Al_2O_3 which both can be achieved by either nitriding or oxidizing a thin AlAs epilayer deposited on the silicon substrate. A recent review to overcome the problems in GaN epitaxy on silicon is given in [24]. The most perfect substrate regarding lattice mismatch could be the lithium-gallate ($LiGaO_2$). Unfortunately its thermal stability is limited, favoring GaN epitaxy with alternative nitrogen precursors at reduced growth temperatures. Unfortunately lower growth temperatures still produce epilayers of lower crystalline quality [25]. In case of InN growth the search for alternative substrates revealed GaP(111)B as a possible alternative but still a nucleation layer has to be grown prior to the epilayer because of the 8 % lattice mismatch [26]. In Table 1.1 an overview is given for the common substrates together with their respective structural data and their lattice mismatch compared to GaN. At the end of this table AlN and InN structural data are shown for completeness. In this work growth of GaN and InN will be performed solely on hexagonal (0001) sapphire since this is still the standard substrate for device production.

Material	Lattice const. a (Å)	Lattice const. c (Å)	Mismatch (%)	Therm. exp. (10^{-6}/K)	Enthalpy (ΔH)
GaN	3.189	5.185	–	5.59	-1.08
Al_2O_3	4.758	12.991	-33.0	7.5	–
SiC - 6H	3.08	15.12	+3.5	4.2	–
Si (111)	3.804	3.804	-17.0	2.59	–
LiGa0$_2$	A=5.4, B=6.4	5.007	+0.1	A=11.0, B=1.7	–
AlN	3.111	4.180	+2.5	4.2	-3.13
InN	3.54	5.704	-11.0	3.4	-0.21

Table 1.1: Comparison of the substrates typically used for III-nitride growth and their respective lattice mismatch to GaN after [24]. Thermal expansion is averaged for a and c. Additionally the Gibbs free energy of formation for the nitrides AlN, GaN and InN is given after [27].

Furthermore the Gibbs free energy of formation ΔH for the nitrides is given show-

ing thermal stability decreasing from AlN over GaN to InN. This is one explanation for the problems in successfully growing InN epilayer. Comparing the lattice constants of GaN and sapphire the relative difference appears to be 33%. The actual lattice mismatch from only 16.1 % is due to the fact that the epitaxial orientation between substrate and epilayer favors a 30 ° rotation in the plane perpendicular to the c-axis direction leading to a drastic decrease in mismatch. The epitaxial relationship then is:

$$[0001]_{GaN} \parallel [0001]_{sapphire} \text{ and } [01\bar{1}0]_{GaN} \parallel [\bar{1}2\bar{1}0]_{sapphire}$$

as depicted in Figure 1.1. Of course the same relationship occurs for growth of AlN and InN on sapphire leading to reduced mismatch, too. This is shown in table 1.2 were the respective mismatch is shown for AlN, GaN and InN with and without rotation in the plane perpendicular to the c-axis.

Material	$[01\bar{1}0]_{III-N} \parallel [\bar{1}2\bar{1}0]_{sapph.}$	$[11\bar{2}0]_{III-N} \parallel [11\bar{2}0]_{sapph.}$
AlN	+13.3	-34.6
GaN	+16.1	-33.0
InN	+29.2	-25.4

Table 1.2: Lattice mismatch in % for AlN, GaN and InN growth on sapphire with and without rotation in the plane perpendicular to the c-axis (after [28]).

However, this mismatch which occurs for GaN/sapphire with the unit cells ordered $[01\bar{1}0]_{III-N} \parallel [\bar{1}2\bar{1}0]_{sapph.}$ is still too high for epitaxial growth. A possible explanation can be the formation of a so-called "coincidence lattice" where only every 8th plane of the film fits to every 9th plane of the substrate. Then the remaining mismatch is below 3%. For InN/sapphire growth this in-plane rotation leads to a slightly increased lattice mismatch. Additionally growth can be performed on other planes of the sapphire

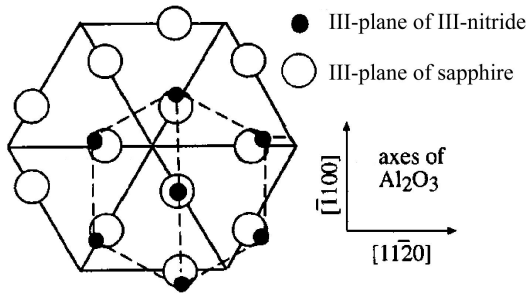Figure 1.1: Epitaxial orientation between Sapphire substrate and GaN epilayer. A rotation of 30 ° of the unit cells in the c-plane leads to significant reduction in lattice mismatch for GaN and AlN.

substrate as shown in Figure 1.2. This can be used either for tuning the piezoelectric fields in thin AlGaN/GaN lattices for transistor structures or for improved cleavage of the nitride structures in laser device production.
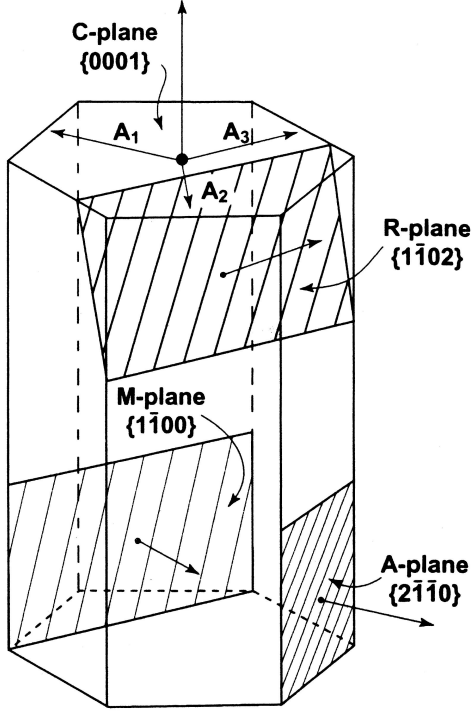
Figure 1.2: Epitaxial growth planes on sapphire substrate. Usually growth is performed on c-plane (top) but other planes (like e. g. R-plane) allow for easy and improved cleavage of laser facets.

1.1 MOVPE growth of GaN

For MOVPE growth of group III nitrides ammonia (NH_3) is used as a standard nitrogen precursor and trimethylgallium (TMGa) as a gallium precursor for GaN. This combination has produced high quality GaN layers [29] and at least the use of NH_3 is considered a standard [5]. Park et al. [30] showed that TMGa can be considered fully decomposed at 575°C in ammonia ambient with a V/III ratio of 3. 300. The same authors showed that an increase of the ammonia flow promotes the pyrolysis of TMGa. Under non equilibrium conditions (as in MOVPE), ammonia is decomposed only up to 4% at 950°C [31]. At this temperatures ammonia gets cracked catalytically at the GaN surface [32]:

$$NH_3 \rightleftharpoons \frac{1}{2}N_2 + \frac{3}{2}H_2 \tag{1.1}$$
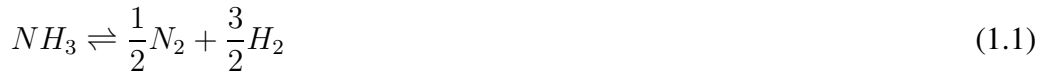
Another effect under these conditions is the surface stabilization of GaN. Under typical MOVPE growth conditions the N_2 equilibrium pressure is of the order of hundreds of bars [33]. This should result in the decomposition of GaN into liquid gallium and molecular nitrogen:

$$GaN \rightleftharpoons Ga_{liq} + \frac{1}{2}N_2 \tag{1.2}$$

Combining equations 1.1 and 1.2 yields:

$$NH_3 + Ga_{liq} \rightleftharpoons GaN + \frac{3}{2}H_2 \tag{1.3}$$

From this, one can see that ammonia prevents the decomposition of the surface through enforcing the reaction of liquid Ga to GaN. All this explains why ammonia is the preferred nitrogen precursor for growth of GaN. Growth with alternative precursors (non symmetric) Dimethylhydrazine (UDMHy) [34] or Tertiarybutylhydrazine (TBHy) [25, 35–37] has been reported, too. However, the quality of GaN layers grown with these precursors is far from the quality obtained by ammonia. The advantage of much lower decomposition temperatures around 400 °C is compensated by high carbon incorporation into the layer in the case of UDMHy. Furthermore reduced surface mobility of the adatoms at low growth temperatures would lead to an increase of the structural defect density. A short characterization of such GaN layer grown with UDMHy is given in chapter 4.5. These alternative precursors are more favorable and already successfully used in growth of diluted ternary or quaternary nitrides like GaAsN [38] or InGaAsN [39] for long wavelength emitting devices. Here NH_3 does not lead to significant nitrogen incorporation between 500 and 600 °C growth temperature.

1.2 MOVPE growth of InN

Since growth of high quality InN epilayers is a new and interesting field for many researcher here a short introduction shall be given in recent approaches and developments. In the 80's growth and characterization mainly took place using rf-sputtering processes of pure indium in either nitrogen or nitrogen/argon gas atmosphere [11, 14]. Glass substrates were used on which polycrystalline thin films were deposited. The properties of these films like the band edge of 1.89 eV (now the term 'band edge´ is more useful in this context since only absorption measurements were performed) and the lattice constants a_0=3.5480 and c_0=5.760 Å were clouded by very high carrier concentrations in the $10^{20} cm^{-3}$ range and the fact that these films consisted of needle-like polycrystalline but oriented crystals of several-nm in diameter [11]. The composition analysis revealed a high oxygen concentration of 11 % [14] but the origin and its influence on the layer properties remained unclear. Later an even larger oxygen content of up to 30% was revealed by XPS [15] and it could be shown that also the size of InN nanorods strongly effects the optical properties of such films resulting in a wide variation of the InN band edge position [40].

Then successfully MOVPE of InN has been reported since the late 90´s from several groups using either ammonia [41, 42] or rf-cracked nitrogen [43, 44]. But the layer grown on sapphire were very thin and they suffered from poor crystallline quality as indicated by Raman line width [42]. The only lattice properties reported so far from

XRD measurements were in agreement with the results from the sputtered material and absorption measurements from Chen et al. showed a band edge of around 1.9 eV [42]. With improvement in MBE growth by migration enhanced epitaxy (MEE) in the beginning of 2000 [45] together with metal-organic MBE (MOMBE) growth [46, 47] a drastic improvement in InN layer quality was achieved. This made a much more precise determination of the material properties possible leading to contradictory results mostly for the band edge energy: unexpectedly the InN band edge appeared far below 1 eV [47–49] and the so called "band edge discussion" was started and it is still going on. Behind these results the interest in InN epitaxy grew drastically and several groups succeeded in growing MOVPE InN with improved quality namely Yamamoto et al. [50], Keller et al. [51], and Briot et al. [52] all of them using trimethylindium (TMIn) and ammonia (NH$_3$) as precursors. The remaining dissimilarities in the optical properties reported so far are expected to result from the high residual carrier concentration either related to crystal defects or impurities like for example oxygen. The latter is supported by the fact that InN grown with rf-excited nitrogen plasma exhibits broad orange luminescence around 2 eV [53]. This luminescence could be attributed to oxygen vacancies in the In$_2$O$_3$ sublattice formed through oxygen incorporation in the InN.

At the same time the choice of the optimum growth process, the ideal substrate and the respective growth parameters in MOVPE are still under discussion. Several groups reported tremendous progress by use of reactive nitrogen through plasma excitation of N$_2$ [43, 53, 54] while others used NH$_3$ at very high V/III ratios up to 10^5[50, 55]. This seems to be necessary due to the high ammonia stability at the low InN growth temperatures at around 500°C. But even with relatively low V/III ratios of several thousands high quality layer could be obtained as shown by the group of Briot et al. in the more recent past [56]. The whole situation reminds one of the late 80´s / early 90´s when drastic improvements in GaN layer quality and new results for understanding growth mechanisms were published nearly every week.

For growth of InN similar argumentation for surface stabilization like for GaN can be done using trimethylindium (TMIn) as the group III precursor. The relatively low binding energy of InN (see also table 1.1) leads to distinct lower decomposition temperature of bulk InN and thus the epitaxial requirements for MOVPE growth are even more extreme. The best way to achieve high quality epitaxial layer will be highlighted in more detail in chapter 6.

1.3 (PA)MBE growth of GaN

Understanding the spectroscopic ellipsometry (SE) results during epilayer growth in MOVPE requires a comparison to the well known and established GaN plasma assisted MBE ((PA)MBE) growth process since SE does not give a detailed insight into the real, atomic structure and composition of the surface. Surface analysis methods have to be

carried out additionally which require an UHV environment. The most surface science results on GaN are achieved with (PA)MBE grown GaN [57–62] which allows for a direct surface symmetry and composition determination using electron based methods like LEED, RHEED, STM and AES. Thus the experimental (PA)MBE setup will be briefly described with respect to the specific growth details and the ellipsometry setup used for *in situ* growth monitoring. In situ ellipsometry is used here to compare the surfaces produced by (PA)MBE to those under MOVPE conditions. Also the widely accepted results of the (PA)MBE experiments from literature are highlighted. This is fundamental for comparison of the MOVPE and (PA)MBE results described in chapter 5 and therefore we start with a short overview into the known GaN surface properties.

Polarity of GaN-(PA)MBE surfaces

In contrast to for example GaAs the wurtzite structured materials like GaN or AlN have no mirror symmetry with respect to the (0001) plane. There exists no symmetry operation that can relate the [0001] and [000$\bar{1}$] direction of GaN. In the usual convention the (0001) surface is called Ga-face, terminated with gallium atoms and the (000$\bar{1}$) surface is called N-face, terminated with nitrogen atoms [60, 63] as shown in figure 1.3. This phenomenon is also called "polarity", i. e. Ga-polar or N-polar. One should keep in mind that this definition of polarity is related to the bulk properties and of course the N-face side of GaN can be Ga-terminated, as we will see. This and the fact that polar surfaces heavily influence the properties of nitride based devices like for example field effect transistors [64] makes the polarity determination indispensable for interpretation of surface properties. In former times there was much confusion about nitride polarity and their respective surfaces and contradictory results for GaN polarity measurements could be found [63]. For understanding the results of the comparative (PA)MBE experiments and their exact interpretation as described later in chapter 5 a short excursion into the world of polar nitride surfaces is necessary. This will demonstrate the related problems and give insight into the usual surface properties of epitaxial MOVPE grown GaN especially on sapphire. When in 1988 Sasaki et al. [65] examined MOVPE grown GaN on 6H-SiC using XPS they found the C-face grown GaN to be oxidized easily and thus it must be Ga-face. This was the first study supposed to determine GaN polarity. In 1993 Khan et al. [66] used AES studying GaN/AlN/sapphire and deduced from the detected N/Ga-ratio that these surfaces had to be N-face. Of course these procedures are useful and necessary for surface chemistry determination as we will see later but those attempts were not able to give insight into the lattice termination. Later more reliable consistent results were obtained by Seelmann-Eggebert et al. [67] using X-Ray photoelectron diffraction (assisted by a chemical etching using KOH) and Ponce et al. [68] using HRTEM, respectively. They gave insight into the relative atom positions finding
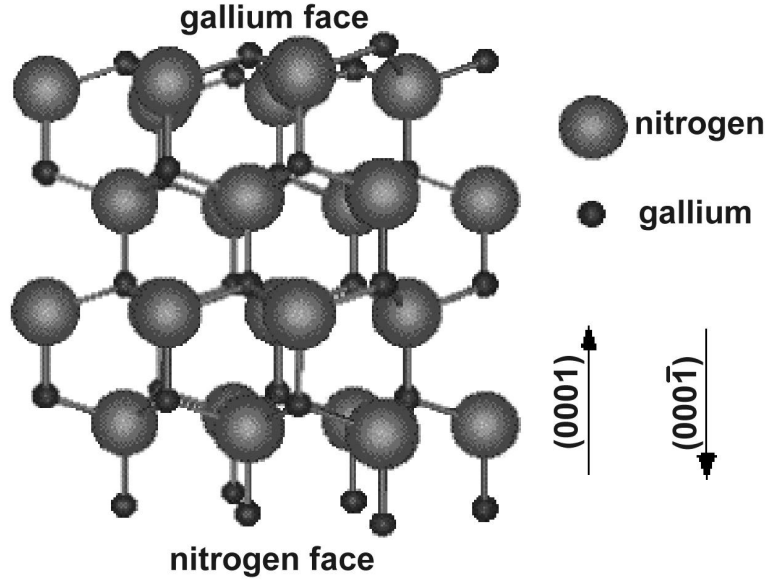
Figure 1.3: The wurtzite crystal structure of GaN leading to highly polar surfaces called gallium face and nitrogen face for the [0001] and [000$\bar{1}$] direction, respectively. The sizes of the atoms illustrate their ionic radii. In diagrams using the covalent radii the gallium's are bigger than the nitrogen's (after [63]).

smooth, Ga-face MOVPE GaN on sapphire and Al-face AlN on Si-face SiC which both were contradictory to the previous publications of Sasaki and Khan [65, 66]. More detailed CBED electron diffraction studies in 1996 from Ponce et al. [69] on MOVPE GaN/sapphire with low temperature GaN nucleation layer showed that smooth surfaces tend to be Ga-face while direct growth on sapphire forms hexagonal pyramids with flat tops containing many inversion domains being mostly N-face. Finally the polarity of MOVPE GaN/sapphire strongly depends on the nucleation layer used and how it is treated prior to growth [70, 71] and the way the substrate was prepared (nitridation or not [72]). But using the standard GaN low temperature nucleation layer with a short annealing time under nitrogen rich conditions only Ga-face reconstructions should occur [70, 71]. Thus smooth, high quality MOVPE grown GaN on sapphire is determined to be Ga-face [63, 69]. This discussion finally ended up in a huge number of publications from Smith and coworkers concerning the different reconstructions formed on the two faces of GaN under various V/III ratios in (PA)MBE. Standard electron based diffraction methods like LEED and RHEED together with STM allowed a precise characterization of the surface symmetry of the [0001] side [57–60] and the [000$\bar{1}$] side [59–61] as well together with the atomic termination responsible therefore. Resuming their results the following can be stated for the [0001]-side of MOVPE grown GaN on sapphire (which is solely investigated here) under (PA)MBE conditions according to

[62]: In (PA)MBE growth takes place under gallium rich conditions to achieve smooth
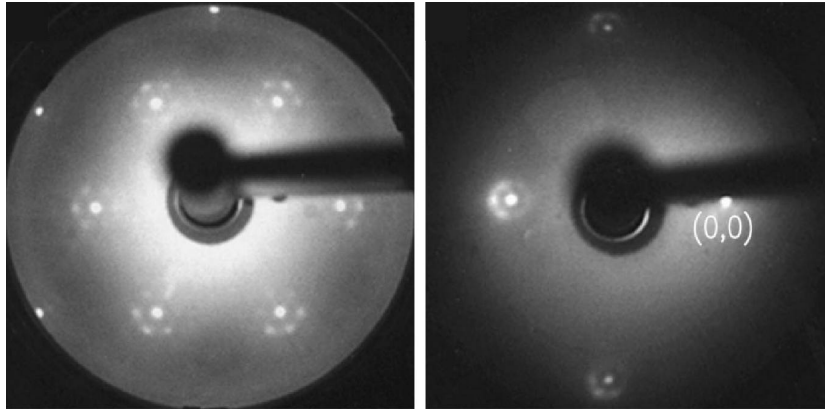

Figure 1.4: LEED pattern for gallium rich GaN(0001) MOVPE templates under (PA)MBE conditions. During cooling additional spots as a ring around the (0,1) spot appear. Their ring radius is approx. 1/6 of the (0,1) spot distance (left). While cooling to room temperature the distance decreases to 1/12 (right). These structures are induced by the fluid-like Ga-bilayer formed on top of the (0001)GaN surface (after [59]).

surfaces through 2-dimensional growth while a decrease of the gallium flux (equivalent to an increase in N/Ga-ratio) leads to unwanted immediate roughening of the surface. Switching off the nitrogen and gallium sources during growth with instantaneous cooling of the sample from growth temperatures of typically 800-900 °C to room temperature the surface can be frozen in a gallium rich state. In this case the respective LEED pattern reveals a "1x1"-like symmetry with additional spots around the (0,1) spot (left image in figure 1.4) having a radius of 1/6 of the (0,1) spot distance. They are due to the formation of a gallium-bilayer on the Ga-side of GaN which is contracted relatively to the GaN unit cell by 6/7 because of the gallium lattice constant being slightly smaller but close to that of the GaN lattice constant (2.75 nm instead of 3.19 nm). Finally at room temperature the pattern changes again showing a decrease of the ring diameter to 1/12 (right image in figure 1.4). Thus the structures are called "1+1/6"and "1+1/12", respectively. These LEED pattern will be discussed later in more detail in the PAMBE section of chapter 5.

As Smith et al. [60] have shown, all stable GaN surface reconstructions on both sides ([0001] and [000$\bar{1}$], also called A and B) depend more or less on the amount of gallium on the surface leading to all the different reconstruction patterns observed. Stable nitrogen rich reconstructions could not be found. If N-rich reconstructions occurred in vacuum they were destroyed with rising temperature, at least at 800 °C [73]. Theoretical considerations also show the tendency of GaN to develop Ga-rich surfaces even under N-rich conditions [74]. This can be explained by the difference between the binding energy of Ga-bulk ($\approx$3 eV) and the N_2 molecule (equaling "N-bulk") ($\approx$5 eV)

which is quite high compared to other III-V materials (e.g GaAs with a binding energy of As-bulk of ≈ 2.9 eV). Therefore the system prefers Ga to N adatoms to the surface. The small lattice constant of GaN being close to that of Ga-bulk gives rise to metallic Ga-Ga bonds at the surface which also makes a Ga-adlayer more favorable [75].

Only a slightly different number of gallium adatoms are responsible for the different reconstructions within a long range order. Therefore the classical electron counting rule will not explain surface stability like in most cases of the conventional III-V´s. Moreover the surface adatoms are in a metallic like state. Thus one should not neglect the presence of residual gases like for example hydrogen atoms being included in the formation of different reconstructions, too [76]. This behavior has been previously reported to explain the differences in surface reconstructions occurring for cubic GaP grown in MBE and MOVPE [77].

1.4 Experimental setup

In the following the two different epitaxial growth setups which were used for the experiments in this work are briefly introduced. For the MOVPE setup several upgrades were carried out for growth of III-nitrides. The (PA)MBE setup just needed to be equipped with the ellipsometer and the plasma source.

MOVPE setup

In Figure 1.5 the principal setup of the used low pressure (LP) Epigress MOVPE system is shown. The standard horizontal reactor was equipped with three optical windows for in-situ monitoring [78]. The one mounted vertical is used either for reflectometry measurements or in case of ellipsometric investigations an alignment laser detects the sample position to measure and eventually correct the angle of incidence of the ellipsometer. The side windows are mounted under an angle of 65 ° which is close to the brewster angle of GaN (which is indeed 69 °). This angle was chosen as an acceptable compromise to allow growth and ellipsometry investigations also for other materials (like GaAs or ZnSe) which formerly have been grown in this equipment and whose brewster angles are lower. For growth of group III-nitrides with ammonia several changes in the epitaxial setup were made. These changes result from the EPIQUIP machine formerly designed for III-phosphide and III-arsenide growth. The changes mainly include installation of a hydride-gas monitor and the respective safety switches as well as a special designed wet-scrubber with a high capacity for neutralization of the ammonia which has not dissociated during the growth process. This scrubber has to be capable to neutralize several liters of ammonia per minute and its overall capacity should be enough for at least one bottle (N10 equiv. 13.000 l) of ammonia. Therefore
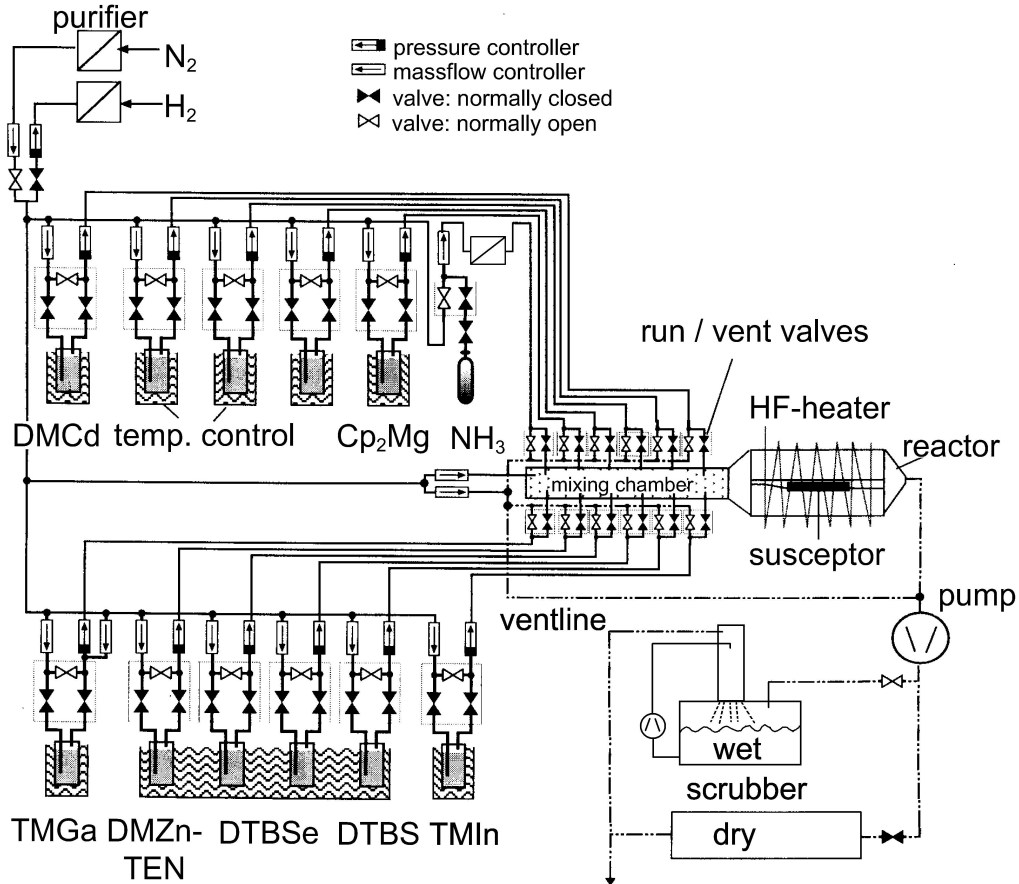
Figure 1.5: Scheme of the upgraded low pressure Epigress VP-50-RP MOVPE machine. The group III supply is given through trimethylgallium and -indium while reactive nitrogen is offered as gaseous ammonia. Many of the additionally mounted sources were used for former II-VI compound growth now serving as potential dopant sources. Additional ammonia purification for reduction of oxygen and moisture is achieved through a catalytic metal filter unit. The additional mounted liquid scrubber filled with diluted H_2SO_4 solution is used during III-nitrides growth instead of the conventional solid scrubber to reduce the amount of remaining non dissociated ammonia in the waste gas.

a container with 60 l sulfuric acid in a concentration of 30 % is used which is continuously pumped downstream in a high column while the used reactant gases flow upstream. To achieve high quality nitride epilayer one has to avoid the incorporation of oxygen resulting from moisture in the ammonia precursor. Even if the precursor is of highest purity available (6.0 equivalent to 99.9999 %) the use of 1 sl/min ammonia as standard epitaxy flow includes a high amount of residual foreign substances out of the ammonia. To overcome this problem a special ammonia purification unit consisting

of a catalytic metal filter has to be mounted in the gas lines. A significant reduction of oxygen incorporation in the epilayer is achieved this way. The rf-power supply for inductive heating of the graphite susceptor was equipped with 186 new, high quality, high voltage Darlington npn-transistors to ensure long-term operation under maximum power output for high temperature nitride growth.

(PA)MBE setup

While in typical MBE systems the group-III and group-V sources are solid and thermally evaporated from effusion cells (or so called "Knudsen cells") the growth of nitrides requires a modified setup due to the lack of solid nitrogen precursors. Nitrogen is provided either by ammonia which thermally decomposes on the growing surface thus providing reactive nitrogen (reactive MBE, RMBE) or by RF- or plasma-activated nitrogen radicals (plasma assisted, PAMBE). The latter is more common for UHV growth of nitrides and we use the (PA)MBE method for our comparative experiments, too.

The nitrogen gas passes through the plasma gun with a flux of 1-10 sccm activated by an excitation frequency of 13.67 MHz with a power of 200 W. The gaseous nitrogen radicals then enter the vessel from the same position where the Knudsen cells formerly have been mounted targeting directly on the sample surface. To achieve the highest flux of nitrogen radicals possible while keeping a low base pressure of around 5×10^{-5} mbar during growth an additional turbo molecular pump is mounted close to the plasma gun. This also ensures rapid pressure decrease after growth for quick transfer of the sample from the preparation vessel to the analysis vessel. The analysis vessel is equipped with a low energy electron diffraction (LEED) unit and Auger electron spectroscopy (AES) for surface reconstruction and stoichiometry analysis.

The ellipsometer is mounted directly to the ellipsometer window flanges which include an angle of only $51°$. This is far below the brewster angle of GaN (see also previous section) but the general vessel geometry did not allow for a higher angle. Thus the ellipsometer is additionally equipped with a light chopper on the lamp side and a lock-in amplifier for improved noise reduction. The overall measurement time for one spectrum increases to approx. 10 min achieving similar SNR as in MOVPE measurements. The whole setup including the vessel, the ellipsometer and the UHV analysis unit is shown in figure 1.6.
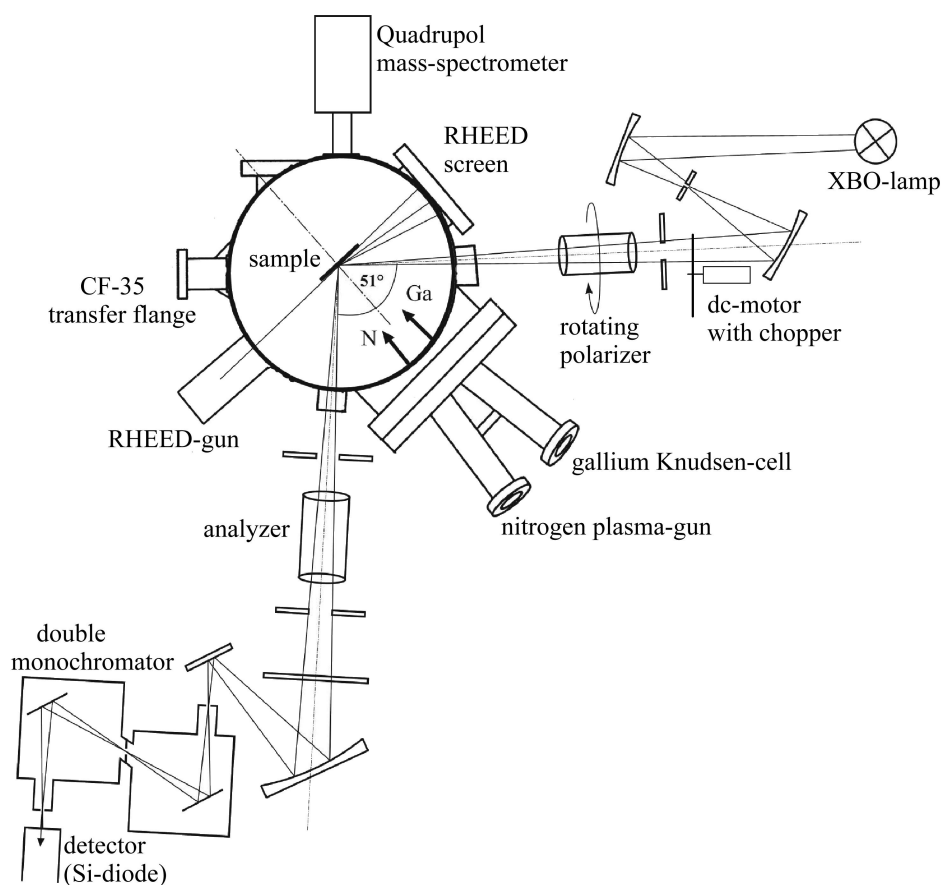
Figure 1.6: Cross section schematics of the (PA)MBE preparation vessel with the ellipsometer attached. Gallium is evaporated from a Knudsen cell and a plasma gun produces reactive nitrogen plasma. Optional a QMS or a beam flux controller and RHEED can be mounted to the preparation vessel. The CF35 transfer port on the left side allows for sample transfer to the analysis chamber equipped with AES and LEED.

Chapter 2

Spectroscopic ellipsometry

In this work mainly in situ processes are studied which occur during heteroepitaxy of hexagonal GaN and InN on sapphire in MOVPE in order to provide a basis for an efficient optimization of nitride epitaxy. Spectroscopic ellipsometry (SE) is the method of choice for in situ monitoring since the gas phase environment in MOVPE prohibits the use of electron based methods. RAS (or RDS) which is commonly used to study cubic materials during epitaxial growth including surface reconstructions and stoichiometry [79, 80] does not fulfill the requirements of the hexagonal nitrides. Here the measured anisotropy signal solely results from in-plane strain in the epitaxial layer and a tilt of the c-axis with respect to the surface normal. No surface related information can be deduced therefrom as proven by Rossow et al. [81]. Approaches monitoring the GaN growth process with more simple methods like in situ reflectometry [18, 82] or surface photoadsorption [83, 84] always suffer from the missing knowledge of complementary layer properties. This can be either the composition and thus exact dielectric properties in case of reflectometry or the layer structure (thickness, roughness) for SPA.

Spectroscopic ellipsometry measures the change of the state of polarization of the light after being reflected from a sample. Therefrom the imaginary part of the dielectric function (DF) $\epsilon(\omega) = \epsilon_1(\omega) + i\epsilon_2(\omega)$ can be extracted using an appropriate optical model (cf. chapter 3). Thus SE has clear advantages compared to conventional reflectance spectroscopy measurements which are in the need of Kramers-Kronig transform techniques and extrapolation beyond the measured spectral range to achieve ϵ_1 and ϵ_2 [85]. The measuring principle of ellipsometry is shown in Figure 2.1. When monochromatic, linearly polarized light is reflected from the sample under non-normal incidence ($\phi \neq 0$) the reflected electric field vector divided in components perpendicular (E_{rs}) and parallel (E_{rp}) to the plane of incidence can be written as:

$$E_{rs} = r_s \cdot E_{is} = \mid r_s \mid e^{i\delta_s} \cdot E_{is} \qquad , \qquad E_{rp} = r_p \cdot E_{ip} = \mid r_p \mid e^{i\delta_p} \cdot E_{ip} \qquad (2.1)$$

with r_s and r_p being the complex reflection coefficients given through the $FRESNEL$
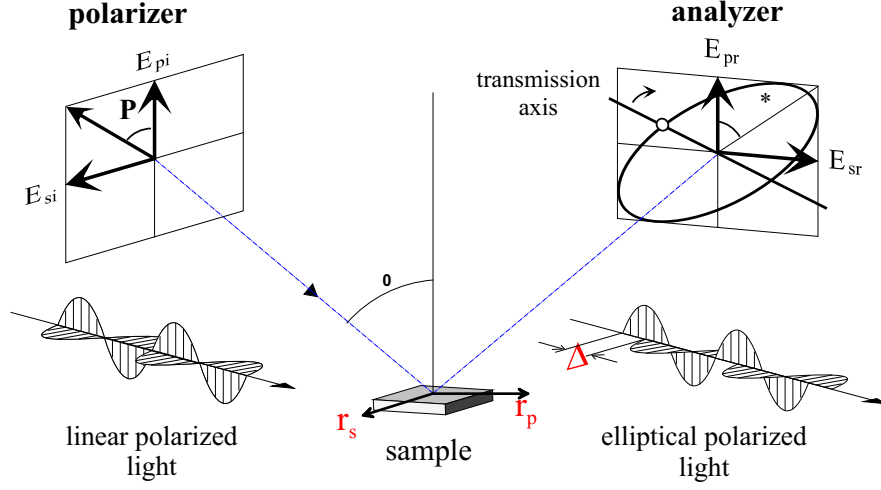
Figure 2.1: Scheme of the principles of ellipsometry. Linear polarized light is used for investigating the samples. The change of polarization through interaction with surface and bulk leads to a phase shift Δ and an ellipticity ψ which are analyzed via the intensity changes at the detector depending on the state of polarization.

equations

$$r_s = \frac{n\cos\phi - n_0\cos\phi_{refr}}{n\cos\phi + n_0\cos\phi_{refr}} \qquad , \qquad r_p = \frac{n\cos\phi - n_0\cos\phi_{refr}}{n\cos\phi + n_0\cos\phi_{refr}}. \qquad (2.2)$$

Here n and n_0 are the complex indices of refraction of sample and ambient, respectively related to the dielectric function ϵ as $n = \sqrt{\epsilon}$. With the ambient chosen to air or vacuum one usually defines $n_0 = 1$. Via Snell's law the angle of refraction ϕ_{refr} is given as

$$\sin\phi_{refr} = n_0/n \sin\phi. \qquad (2.3)$$

As shown in Figure 2.1 the incident light is linearly polarized with E_{is} and E_{ip} being in phase and their ratio determined by the angle of polarization χ

$$\frac{|E_{is}|}{|E_{ip}|} = \tan\chi \qquad (2.4)$$

while the reflected light in general is elliptically polarized. The ellipticity results from the phase difference Δ between E_{rs} and E_{rp} equal to the phase difference in r_s and r_p. The ratio of $|E_{rs}|/|E_{rp}|$ changes with respect to $|E_{is}|/|E_{ip}|$ and the ratio of E_{rs} and E_{rp} according to:

$$\frac{|E_{rs}|}{|E_{rp}|} = \frac{|r_s|}{|r_p|}\frac{|E_{is}|}{|E_{ip}|} = \frac{|r_s|}{|r_p|}\tan\chi \qquad (2.5)$$

Evaluating the polarization state of the light and defining the complex reflectance ratio $\rho := r_p/r_s$ it can be measured as:

$$\rho := \frac{r_p}{r_s} = \frac{\mid r_p \mid e^{i\delta_p}}{\mid r_s \mid e^{i\delta_s}} = \frac{\mid E_{rp} \mid}{\mid E_{rs} \mid}\frac{\mid E_{is} \mid}{\mid E_{ip} \mid}e^{i\delta_p - \delta_s} = \frac{\mid E_{rp} \mid}{\mid E_{rs} \mid}\tan\chi e^{i\delta_p - \delta_s} =: \tan\psi e^{i\Delta} \quad (2.6)$$

Here the angles ψ and Δ defined in eq. 2.6 are called the "ellipsometric angles". Now the calculation of ϵ proceeds as (after [86]):

$$\epsilon = \sin^2\phi(1 + \tan^2\phi(\frac{1-\rho}{1+\rho})^2) \qquad (2.7)$$

In practice the state of polarization is detected with a rotating polarizer/analyzer probing for the ellipticity $\xi = \arctan a/b$ (the ratio of the main axes) and the azimuth ψ. Then the modulated intensity at the detector behind the analyzer can be written as:

$$I(\alpha(t)) = I_0 + C_2\cos 2\alpha(t) + S_2\sin 2\alpha(t) = I_0(1 + c_2\cos 2\alpha(t) + s_2\sin 2\alpha(t)) \quad (2.8)$$

By means of Fourier analysis the normalized coefficients $c_2 = C_2/I_0$ and $s_2 = S_2/I_0$ can be evaluated from the measured intensity signal. Since SE measure relative intensities it is less sensitive to intensity fluctuations than for example reflectance measurements.

But one has to keep in mind the prerequisite of a simple two-layer model with only one reflection at the interface between ambient and the half-infinite substrate. For real, layered structures as investigated here more sophisticated models accounting for the reflections at each interface have to be considered (see chapter 3). Then the dielectric functions of each layer can be calculated separately instead of the *effective* dielectric function or *pseudo-dielectric* function $\langle\varepsilon\rangle$ of the whole layer stack. In this way SE allows for non-destructive probing the material properties providing more information about the fundamental properties such as the electronic structure as well as structural sample properties like surface roughness or layer thickness.

The measured values can be presented in different ways: either in terms of the ellipsometric angles ψ and Δ or in terms of $\tan\psi$ and $\cos\Delta$ (see eq. 2.6). Finally the presentation in terms of $\langle\varepsilon_1\rangle$ and $\langle\varepsilon_2\rangle$ or n and k can be used which are directly related to the material properties. All these presentations have in common that typical structures within the spectrum result from electronic transitions in the material and always appear at the same energetic positions. Thus a discussion of the characteristic features can be made in any of these representations.

Already in 1889 Paul Drude measured the optical properties of metals with a very simple but precise ellipsometry setup [87]. Since this time many technical improvements have been realized leading to several different types of ellipsometers [79, 80, 86]. With invention of the personal computer in the 80´s data aquisition and accuracy improved while the whole measurement was performed automatically in a few minutes.

Mostly rotating-analyzer-type ellipsometers are used nowadays where the polarization of the reflected light is analyzed by a rotating polarizer (thus called *analyzer*). It is also possible to use a fixed analyzer and a rotating polarizer which only makes differences in the calculation routine determining the dielectric function .

2.1   In situ ellipsometry

For monitoring the growth process the ellipsometer has to be attached to the MOVPE growth setup. The necessary requirements for such an in situ ellipsometer will be described in more detail in [88]. Here only the most important characteristics of the in situ ellipsometry setup are briefly summarized.

For in situ applications the ellipsometry setup has to be designed in a compact style to fit to the growth equipment as sketched in Figure 2.2. The compact setup is achieved
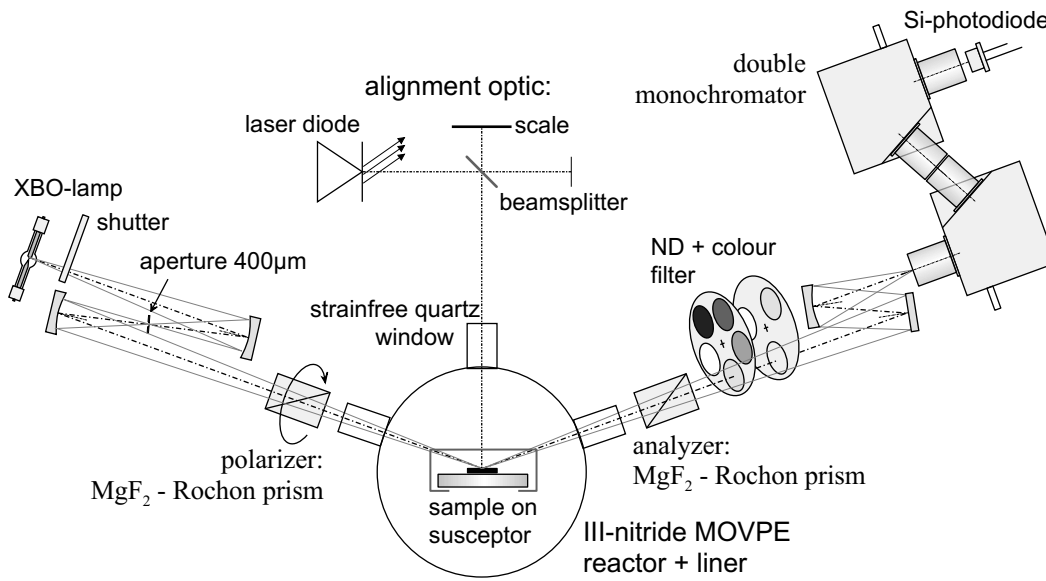

Figure 2.2: Setup of the ellipsometer used as in situ ellipsometer at the EPIQUIP VP50RP reactor. The incoming light is focused via mirrors onto the sample. Small slits of $5 \times 2mm^2$ in each side of the liner tube allow for unhindered projection and reflection. Strain-free quartz windows avoid polarization effects. Colour and gray filter wheels on the detector side are used for spectral and intensity corrections.

through folding the beams and projecting them via mirrors onto the sample and the monochromators, respectively. To achieve a precise adjustment both arms of the ellipsometer have to made adjustable in x, y and z direction as well as in the angle of incidence ϕ and the tilt axis normal to the sample surface. So necessary beam corrections can be made easily during epitaxy and only the change in ϕ has to be monitored.

This is done via an alignment optic consisting of laser, beam splitter, mirror and a mm scale. This alignment optic allows for ϕ-corrections in the range of $2/100°$ when sample movements occur through thermal expansion of reactor and/or susceptor during heating.

For investigation of group III-nitrides the extension of the measurement range into the UV region is necessary since the E_0 band gap from GaN already lies in the UV region (3.42 eV or 362 nm at room temperature). The wide spectral range was possible by using mirror optics instead of lenses which suffer from chromatic aberration and additionally using polarization elements made of MgF_2 instead of synthetic quartz. This material starts absorption at around 10 eV which allows for maximum light intensity until absorption onset from either ammonia (5.9 eV) or air (6.5 eV). Even if the E_1 transition located at 6.9 eV lies above the absorption edge of air this allows for comparison of sample qualities by comparison of the characteristic signal increase towards the E_1 transition (cf. Figure 3.6).

The effect of pre-polarization from the lamp is strongly reduced by focusing the center of the lamp arc onto a very small (400 μm diameter) aperture. This also leads to a more stable beam intensity. To avoid 2nd order effects a set of three color filters is integrated behind the analyzer cutting the light at the desired wavelength. For intensity adjustment (the maximum light intensity of the xenon arc lamp lies at 2.65 eV or 467 nm) a filter wheel with four gray filters avoids signal overload at the detector and reduces intensity up to 10^{-5}. The double monochromator setup reduces stray light originating from background radiation of the susceptor at high epitaxy temperatures above 850 °C.

For a typical spectrum consisting of 100 points (1.5 to 6.5 eV in 0.05 eV step width) approximately 90 s are needed. This is limited by the maximum frequency of the rotating analyzer which is 8 Hz and the need of accumulations during the measurement for noise reduction. Thus access to fast processes on a time scale of a few seconds is only possible with single wavelength transient measurements. The time resolution then is in the range of a few tenth of a second depending on the SNR limit chosen.

With this setup spectral information from fast processes can only be gained by measuring several transients with high time resolution at different energies. The spectral information can then be reconstructed by combining the transient values obtained at different energies for identical processes to the respective multi point spectra. One necessary prerequisite for this approach is the same starting point for each transient, i. e. the surface has to recover completely in between the different transient cycles. This procedure will be used to investigate the GaN surface termination during growth in chapter 5.

2.2   Ex situ DUV ellipsometry

For extended characterization of GaN with its higher interband transitions situated below 200 nm an ellipsometry setup with an extended spectral range is necessary. Therefor the in situ ellipsometer can be used ex situ, too covering a spectral up to 9 eV or 140 nm thus being called *deep UV* (DUV) ellipsometer. Several minor changes to the previous setup have to be made to access this spectral range as shown in Figure 2.3. A
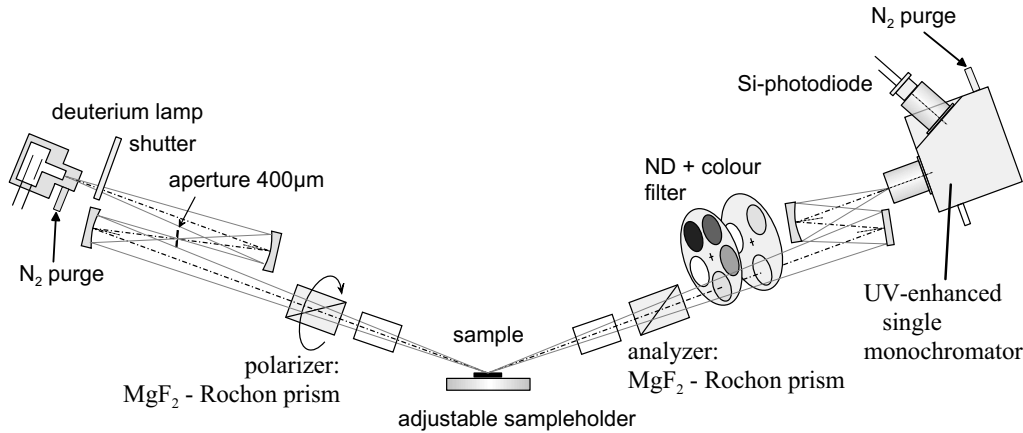

Figure 2.3: Setup of the ellipsometer used as ex situ ellipsometer for material characterization up to 9 eV. A deuterium lamp is used as light source, the single monochromator is specially designed for this wavelength region. A silicon photo diode without window covers the whole spectral range of the lamp. Constant pure nitrogen purge of the whole setup has to be ensured to avoid contamination of the optical surfaces through cracked carbon compounds.

deuterium lamp is used as light source with an emission range from 3 eV to 10 eV. A self-designed single UV enhanced monochromator was adapted instead of the Jobin-Yvon HC10-UV double monochromator since no high background radiation has to be suppressed (radiated from the graphite susceptor in the in situ setup at 1050 °C growth temperature). For light detection a standard silicon photo diode without glass window is used. To avoid light absorption mostly dominated by moisture the whole setup is purged for several hours with dry nitrogen before each measurement. This enhances the accessible maximum energy from 6.5 eV up to 9 eV (or 140 nm). During measurements a constant purge of the critical components (deuterium lamp and monochromator) with pure, dry nitrogen has to be ensured. Otherwise the DUV radiation leads to irreversible contamination of the sensitive optical surfaces with cracked carbon compounds resulting in a drastic loss of intensity. A detailed description of the ellipsometer setup and its development including beam path calculations and monochromator development is given in [88]. With this setup the ex situ ellipsometry characterization of several thick epilayer were performed as shown in chapter 3.3 in Figure 3.6.

Chapter 3

The dielectric function

In this chapter a brief introduction into the theory between the dielectric function and the electronic structure of "ideal" crystals is given. Additionally the influences of physical layer properties on the optical response of the material under investigation is discussed. This is of great importance since all ellipsometry measurements are performed on so called non-ideal materials. They always consist of a stack of different layers (stratified media) containing substrate, epilayer, interface(s) and overlayer(s) like roughness and/or oxide. Therefore the approaches which are used later to subtract these influences will be highlighted. They pave the way to achieve the materials dielectric function out of the measured pseudo-dielectric function and thereby determining the electronic properties of the ideal crystal. This includes also the Tanguy model function which is used later in chapters 4 and 7 for evaluating the energetic band edge position of the GaN NL and InN thin films. Finally a brief introduction into the optical models used for description of each single layer is given together with some examples on influences on the dielectric properties with respect to the GaN dielectric function .

3.1   Theoretical description

The dielectric function $\epsilon(\omega)$ is a macroscopic function which describes the linear response of matter to excitation by an electro magnetic wave with the field vector $\overrightarrow{E}$. The electric field of displacement $\overrightarrow{D}$ depends on the external electric field and is given by:

$$\overrightarrow{D}(\omega) = \epsilon_0 \underline{\epsilon}(\omega) \overrightarrow{E} \tag{3.1}$$

In general $\underline{\epsilon}(\omega)$ is a tensor of rank 2 with complex components. In the case of ideal cubic materials it can be reduced to one independent component and thus written as a scalar $\epsilon(\omega)$. Unfortunately the uniaxial hexagonal III-nitrides enforce us to pay attention for the directions parallel and perpendicular to the hexagonal c-axis. Thus $\underline{\epsilon}(\omega)$ has two

independent components $\epsilon_\perp(\omega)$ and $\epsilon_\parallel(\omega)$. To understand the microscopic origin of the dielectric function we will briefly discuss the imaginary part $\epsilon_2(\omega)$. Making several assumptions (like the one-electron approximation, after [89]) $\epsilon_2(\omega)$ can be treated as the sum of absorptions due to transitions from valence to conduction band states at various points in the Brillouin zone. ϵ_2 can thus be expressed by:

$$\epsilon_2(\omega) = \frac{1}{8\Pi^2\epsilon_0}\frac{\epsilon^2}{m^2\omega^2}\sum_{c,v}\int_{B.Z.}d^3kP_{cv}(\overrightarrow{k})\delta(E_c(\overrightarrow{k}) - E_v(\overrightarrow{k}) - \hbar\omega) \qquad (3.2)$$

were $P_{cv}(\overrightarrow{k})$ is the electric dipole transition matrix element

$$P_{cv}(\overrightarrow{k}) = |< \phi_v(\overrightarrow{k}) \mid e \cdot \overrightarrow{p} \mid \phi_c(\overrightarrow{k}) >|^2 . \qquad (3.3)$$

Here the valence and conduction band energies $E_{v,c}(\overrightarrow{k})$ as well as the electron wave functions $\phi_{v,c}(\overrightarrow{k})$ have to be taken from band-structure calculations. A transformation of the integration in reciprocal space (the Brillouin zone) into an integration over constant energy surface gives:

$$\epsilon_2(\omega) = \frac{1}{8\Pi^2\epsilon_0}\frac{\epsilon^2}{m^2\omega^2}\sum_{c,v}\int_{\hbar\omega=E_c-E_v}d^3kP_{cv}(\overrightarrow{k})\frac{dS_{\hbar\omega}}{\nabla_{\overrightarrow{k}}(E_c(\overrightarrow{k}) - E_c(\overrightarrow{k}))} \qquad (3.4)$$

Now we can interpret the result as follows. Considering $P_{cv}(\overrightarrow{k})$ as $\overrightarrow{k}$-independent and thus shifted in front of the integral large contributions of the integral are expected when the gradient of the energy difference is small or almost zero. This is the case when the bands are nearly parallel. The integral is then called the *joint density of states* and the energetic positions were the bands are parallel are called *band critical points* (or van-Howe-singularities of the joint density of states after [90]). This is helpful for the analysis of the dielectric function derived from a band-structure when plotting band differences to find points of the Brillouin zone where energy differences match to structures in ϵ_2. For GaN this is shown in Figure 3.1 together with the hexagonal GaN Brillouin zone. Here the transitions are labeled arbitrary (except for E_0, after [91–93]) in contrast to cubic materials where the transitions are labelled according to M. Cardona [94]. Usually E_0, E_1 and E_2 denote transitions at the Γ point, points along the [111] direction and the X point, respectively. Labels such as $E_0´$ and $E_1´$ are used for transitions to higher conduction bands. Since no direct assignment for the hexagonal structures has been done yet we just count the transitions according to their increase in energy difference.

For the calculation of the electronic band-structure several approaches exist. In former times the pseudo-potential method required optical measurements to fit some parameters [95]. Nowadays *ab initio* methods are established were no experimental input except the crystal structure is required for prediction of one-electron energies and

wave functions. Here the method of choice is the density functional theory (DFT) utilizing the local density approximation (LDA) for exchange and correlation. With this procedure the fundamental band gap E_0 is typically underestimated. Through a constant shift of all conduction bands ("scissors operator") with respect to experimental E_0 data a good agreement of the derived dielectric function in energetic positions to experimental values can be obtained. To overcome this problem of the underestimated gaps quasiparticle calculations have been performed. But even with these more expensive calculations the amplitude of the dielectric function do not match very well to the experimental data. This is mostly due to the strong electron-hole interaction in the III-nitrides which are not included and which also manifest in the observation of excitons in the dielectric function already at room temperature (this will be discussed in detail in the end of chapter 4). Only when these corrections are taken into consideration a reasonable agreement can be achieved between experiment and theory as shown in Figure 3.1 (right image) for the case of wurtzite GaN. The higher interband features E_1 to
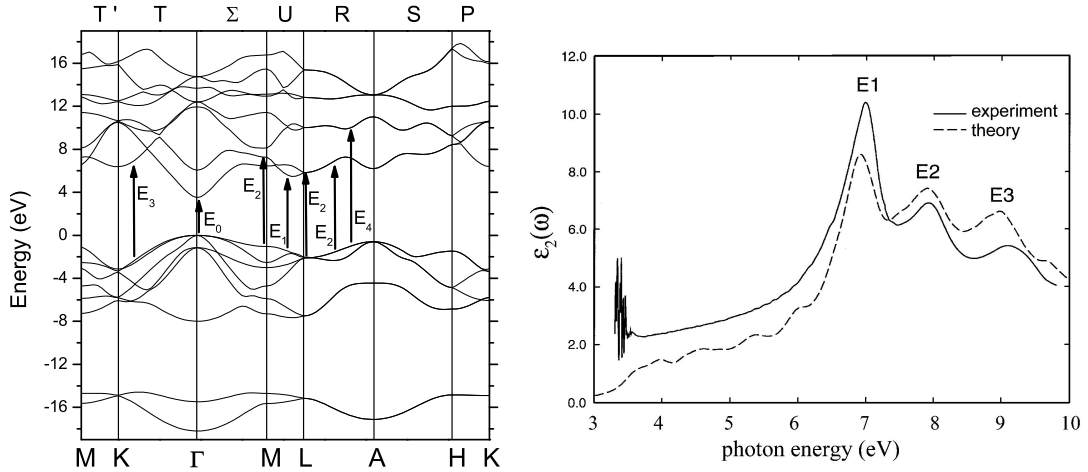

Figure 3.1: Left: calculated GaN band structure after [91, 92]. The bottom labels denote the points of high symmetry in the GaN Brillouin zone as partially depicted in the following Figure 3.2. Labels on top denote the connecting lines between the symmetry points. Arrows indicate the assigned transition energies. Right: the measured GaN dielectric function agrees well with the calculation showing the arbitrary assignment of the transitions E_1 to E_3 (after [93]).

E_3 originating from transitions along M, L and K-direction in the Brillouin zone are shown here in comparison between measurement (solid line) and theory (dashed line, after [93]). When including the electron-hole interaction the decrease of the transition intensities with higher transition energy are described similar to what is observed in the experiment. The points of high symmetry which are labeled in the band structure calculation Figure 3.1 (left image) are shown in the hexagonal Brillouin zone in Figure 3.2.

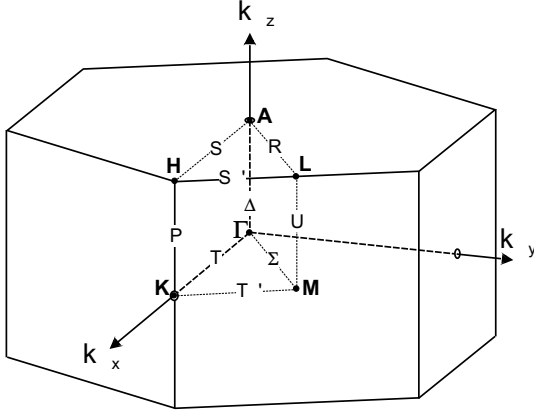Also the connecting lines between these symmetry points are depicted there.

Figure 3.2: GaN Brillouin zone with points of high symmetry. The connection lines between these correspond to the labeling in Figure 3.1.

3.2   Calculation of optical properties

As mentioned in the beginning the dielectric function measured is always an effective dielectric function depending on several layer influences. In this section the principles for calculation (better called "simulation") of the optical properties of the material systems investigated here will be briefly discussed. Therefore the optical layer models used for calculation and the dispersion relations used for the description of the different layers will be explained.

3.2.1   Optical layer models

For the virtual simulation of the measured optical parameters such as $\langle \varepsilon \rangle$ the complex reflectances have to be calculated. Two or three layer models can be solved analytically and in the case of multi-layer structures more complex models have to be solved.

Two phase model

For description of an isotropic and homogeneous substrate-like bulk material a two phase model is sufficient (Fig. 3.3). The reflectance, absorption, and transmittance are totally defined by the angle of incidence φ of the probing light and the material's dielectric function $\varepsilon = \varepsilon_1 + i\varepsilon_2$. Using the complex Fresnel equations (see eq. 2.2 or [86, 96]), the reflectances and transmittances parallel and perpendicular to the plane of incidence r_p, t_p, r_s and t_s can be calculated.
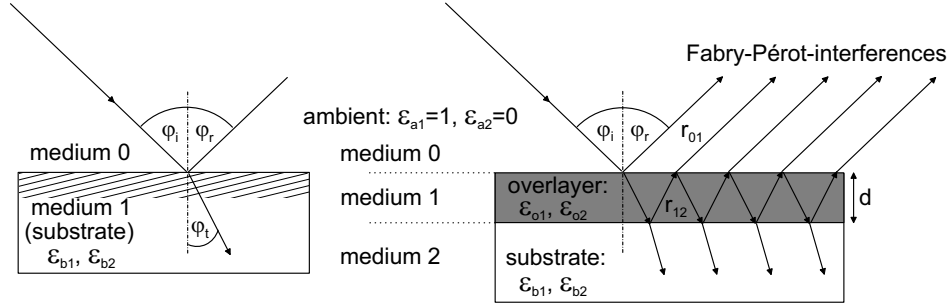
Figure 3.3: Left: two phase model consisting solely of ambient (vacuum, air) and substrate. Right: Three phase model including an additional layer between substrate and ambient.

Three phase model

In reality most of the structures under investigation include an overlayer with thickness d between the substrate and ambient. As long as the penetration depth of the light is larger than d the optical constants of all three media contribute to the optical response of the system leading to multiple beam interferences of the reflected light (Fig. 3.3). The reflectance can be calculated using the Airy-formula [79, 86] with j indicating the number of layers:

$$r = \frac{r_{01} + Z_1 r_{12}}{1 + Z_1 r_{01} r_{12}} \quad \text{with} \quad Z_j = e^{\left[2\Pi i \frac{2d_j}{\lambda/n_j^\perp}\right]} \quad \text{and} \quad n_j^\perp = \sqrt{\varepsilon_j - \varepsilon_a \sin^2 \varphi} \quad (3.5)$$

Defining an *effective* dielectric function $\langle \varepsilon \rangle$ the three-phase model can be reduced to a two-phase model with an integral description of layer and substrate.

Calculating multilayer structures - the Matrix formalism

Multilayer structures consisting of n layer can be described analytically in a mathematical approach using matrix methods [86]. Here the influence of each layer on the transmittance and reflectance (including the change in polarization) is represented by a matrix. The product of all matrices describes the propagation of the light through the whole layer stack.

Calculating multilayer structures - the Iterative model

Instead of the matrix method a step-by-step reduction of a three phase system to a two phase system is performed in the iterative model. Iteratively the n-layer stack is reduced to a (n-1)-layer stack as shown in Figure 3.4 (from left to right). Finally it can be reduced to a three phase system whose optical response can be calculated then. The

results of this procedure are equivalent to the matrix method [97] and often used from computer calculation programs.
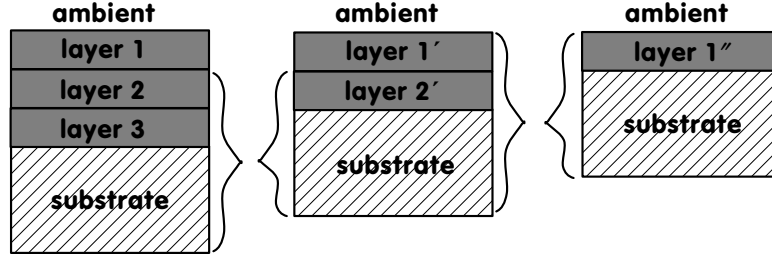

Figure 3.4: In the iterative model each four layers are reduced to three layers until only three remain (from left to right). This system can be solved then analytically.

3.2.2 Dispersion relations

Data arrays

To describe the dielectric function of semiconductor materials data arrays (tables) from clean, overlayer free substrates measured in vacuum or air are published like in for example [98, 99]. Meanwhile most of the standard and well investigated semiconductor materials are listed in this way. Even if these results are very precise (of course depending on the substrate preparation procedure) they often cannot be approximated by a single formula within the spectral range available. Therefore a computational efficient approach is to use the measured data tables interpolating between the measured data points. With this simple approach every dielectric material can be described as long as it is available as "thick", overlayer free substrate material.

Cauchy layer

A more flexible type of layer allows to use custom defined dispersion relations to describe each layer. An expression for the dielectric functions ε_1 and ε_2 or the complex refractive index n and k as a function of the wavelength (or photon energy) and other parameters is required. In the absence of the band gap or higher interband transitions this can be the Cauchy equation describing either absorbing or transparent materials in the measurement range near to a polynomial according to eqs. 3.6 and 3.7.

$$n(\lambda) = n_0 + C_0 \frac{n_1}{\lambda^2} + C_1 \frac{n_2}{\lambda^4} \tag{3.6}$$

$$k(\lambda) = k_0 + C_0 \frac{k_1}{\lambda^2} + C_1 \frac{k_2}{\lambda^4} \tag{3.7}$$

With $C_0 = 10^2$ and $C_1 = 10^7$

Here the coefficients C_0 and C_1 are used to avoid large numbers of n_1, k_1, n_2 and k_2 and their values shown here agree with most publications on Cauchy layers. An example is the sapphire substrate dielectric function in the measurement range from 1.6 to 6.5 eV. The sapphire band edge is expected to be around 8.7 eV [100] and thus the polynomial fit describes $\langle \varepsilon \rangle$ very well.

Lorentz Oscillator

When including the absorption edge or higher interband transitions in the energy range of the dispersion model one has to take into account at least one harmonic oscillator. In this basic dispersion model it can be imagined as an electron with the effective mass m oscillating in a parabolic potential. According to the Lorentz-model a dielectric function can be described by a linear combination of a set of harmonic oscillators. This allows for a very flexible way of simulating an unknown dielectric function but with a large amount of free parameters and thus many uncertainties. This is due to the fact that each harmonic oscillator has three parameters: its resonance frequency ω_0, its strength f, and the damping parameter Γ. Then the dielectric function can be described as:

$$\varepsilon_1 = 1 + \frac{Ne^2}{\varepsilon_0 m} \frac{\omega_0^2 - \omega^2}{(\omega_0^2 - \omega^2)^2 + \Gamma^2 \omega^2} \tag{3.8}$$

$$\varepsilon_2 = \frac{Ne^2}{\varepsilon_0 m} \frac{\Gamma \omega}{(\omega_0^2 - \omega^2)^2 + \Gamma^2 \omega^2} \tag{3.9}$$

with N indicating the density of the atoms in the material. Finally in complex notation using the Drude-equation a set of j harmonic oscillators is given as:

$$\varepsilon_2(\omega) = 1 + \frac{Ne^2}{\varepsilon_0 m} \sum_j f_j \frac{1}{(\omega_j^2 - \omega^2)^2 - i\Gamma_j \omega} \tag{3.10}$$

Tanguy model function

In all the previous descriptions no excitonic effects are considered even though their influence on the optical properties of semiconductors has been known for decades. Such an influence is particularly important in the vicinity of the band edge. Thus a more specific description of real semiconductor materials is given through the Tanguy model function. This is an approximation which provides an analytical expression of the dielectric function of weakly bound Wannier excitons. Herein the contributions of all bound and unbound states were taken into account, while simultaneously including a Lorentzian broadening of the energy levels of width Γ. This broadening allows for

numerical determination of the crystal quality of the investigated layer as an increase
in Γ is directly related to a reduction in carrier lifetime caused by defects or perturbed
crystalline structure. The respective equations are discussed in more detail in [101,
102]. Therefore the dependence of optical constants with temperature or any external
perturbation can be analyzed more detailed. However one has to keep in mind that this
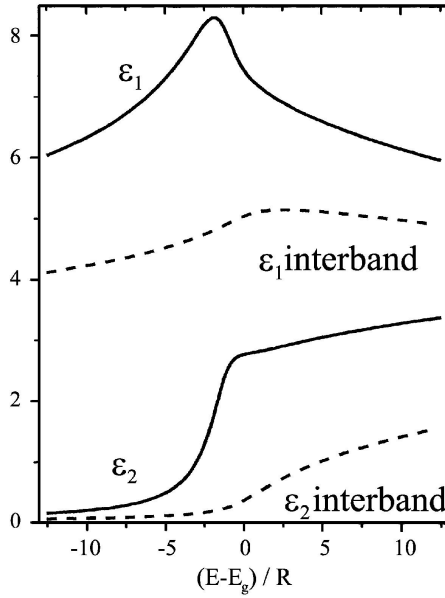model only works in direct vicinity of the band edge as shown in Figure 3.5.

Figure 3.5: Influence of excitonic effects on the real and imaginary part of the dielectric function in the vicinity of the band edge. Without excitonic effects the dashed line shows a broad absorption edge which gets much more pronounced including excitonic effects (solid line). The band edge is chosen to be 1.42 eV, R=0.004 and the broadening is very small with $\Gamma = 0.006$ (after [101]).

Effective medium approximation (EMA)

Finally, for the case that the material under investigation forms a boundary with its
neighbor the materials can penetrate each other. This leads to a mixture of both materi-
als on a microscopic scale which can be extended over several nm in thickness. In the
case that one of the media is vacuum (or air) this is the classical definition of an over-
layer roughness. An interface roughness can be treated accordingly as a mixture of the
two adjacent materials. Due to the fact that the light cannot resolve the precise structure
of the layer only an effective dielectric function $\langle \varepsilon \rangle$ will be sensed, an *effective medium
approximation* has to be used. However, this approximation is in the need of several
assumptions: the micro structural dimensions have to be large enough to avoid quan-
tum size effects. Otherwise the dielectric function will be changed significantly leading
to wrong results in layer properties. Then the micro structure has to be small enough
compared to the wavelength of the probing light ($< \lambda$) to avoid resonant scattering.

Different effective media approximations are described in literature [80, 103]. The
most useful for overlayer roughness description and also used in this work is according

to Bruggemann [104]. Through defining inclusions of a *guest* material ε_a in a *host* material ε_b the effective dielectric function $\langle\varepsilon\rangle$ can be calculated with the fraction *f* of the guest material as a free parameter:

$$f\frac{\varepsilon_a - \langle\varepsilon\rangle}{\varepsilon_a + 2\langle\varepsilon\rangle} + (1 - f)\frac{\varepsilon_b - \langle\varepsilon\rangle}{\varepsilon_b + 2\langle\varepsilon\rangle} = 0 \tag{3.11}$$

The validity of this approximation is limited to $f \approx 0.5$ meaning the fractions of both materials have to be comparable [80]. This assumption yields satisfactory results when analyzing the roughness development during GaN nucleation layer growth (see chapter 4) except for a linear scaling factor. In case of roughness formation through parasitic nucleation as it can be observed during growth of InN (this will be discussed in more detail in chapter 7) this assumption is problematic.

Nevertheless effective medium theory and its calculation results should be always treated with care because: the proper effective medium model for a given sample depends on its specific micro structure and therefore varies for each sample. The parameters determined are not necessarily quantitative for the above reasons and thus the inter layer dielectric response may be different to that from the real bulk.

3.3 Examples for influences of sample properties on the dielectric function

For interpretation of the in situ measurements of the effective dielectric function a detailed understanding of the different influences on the dielectric function is required. This allows a quick response of the grower already during growth through a phenomenological interpretation of the observed differences somehow "guide to the eye". Thus the main two different influences which occur during and after growth: temperature and overlayer effects, are briefly discussed here.

Overlayer effects

The so-called two-phase model previously described to calculate the dielectric function only gives correct values for semi-infinite, isotropic samples were just one reflection at the interface between the sample and the ambient has to be considered. In reality the samples measured are of a more complex, layered structure consisting of a film on a substrate covered with roughness or oxide over layers. The obtained effective dielectric function (*pseudo-dielectric function*) is no longer a material property but rather a sample property averaging over the dielectric responses of the layered system. Nevertheless it is a useful quantity to compare different sample characteristics like surface roughness (see Figure 3.6 below). Here two different GaN samples are measured ex

situ with the DUV ellipsometer setup several days after growth according to the procedure in chapter 4. As a reference GaN dielectric function we took the data set from
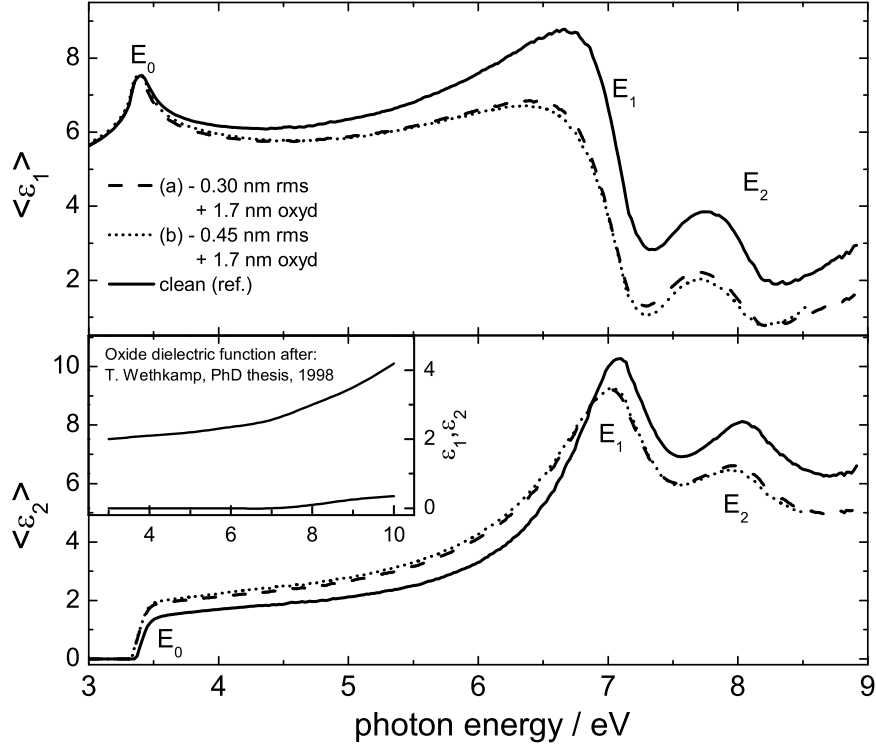

Figure 3.6: Influence of roughness and oxide overlayer on the effective dielectric function of two samples (1.2 μm GaN grown on sapphire) in the range from 3 to 9 eV. They reveal an oxide overlayer thickness of 1.7 nm and a roughness of 0.3 and 0.45 nm, respectively. The solid line shows the GaN DF corresponding to the literature data taken from [91] together with the GaN-oxide dielectric function (inset).

[91] (solid line). Obviously the sample properties differ a lot from the reference and they can be interpreted as follows: a numerical calculation leads to the assumption of an oxide overlayer of 1.7 nm and roughness overlayer thickness of 0.3 and 0.45 nm, respectively. The thicker the roughness overlayer the more the magnitude of the higher interband transitions is reduced. This is due to an increased damping caused by defects as described in [105], p. 111. The oxide overlayer formation took place during transfer in air and can also result from contamination with moisture. The DUV spectral range was chosen here for improved visibility of overlayer influences on the magnitude of the higher transitions. For improved visibility the Fabry-Pérot interferences below the GaN band edge are removed. More DUV investigations on III-nitrides with this special setup will be found in [88].

Whenever a pseudo dielectric function is used rather than a dielectric function of a

specific material it is indicated by angular brackets: $\langle \varepsilon \rangle$.

Temperature effects

Also changes of the temperature show significant changes within the line shape and energetic position of the structures appearing in the dielectric function. In Figure 3.7 this energetic shift accompanied by a dampening of the magnitude of the higher transitions in the effective dielectric function is shown for GaN at room temperature vs. 1030 °C. Therefore the GaN DF was measured in situ at room-temperature (black lines) and at
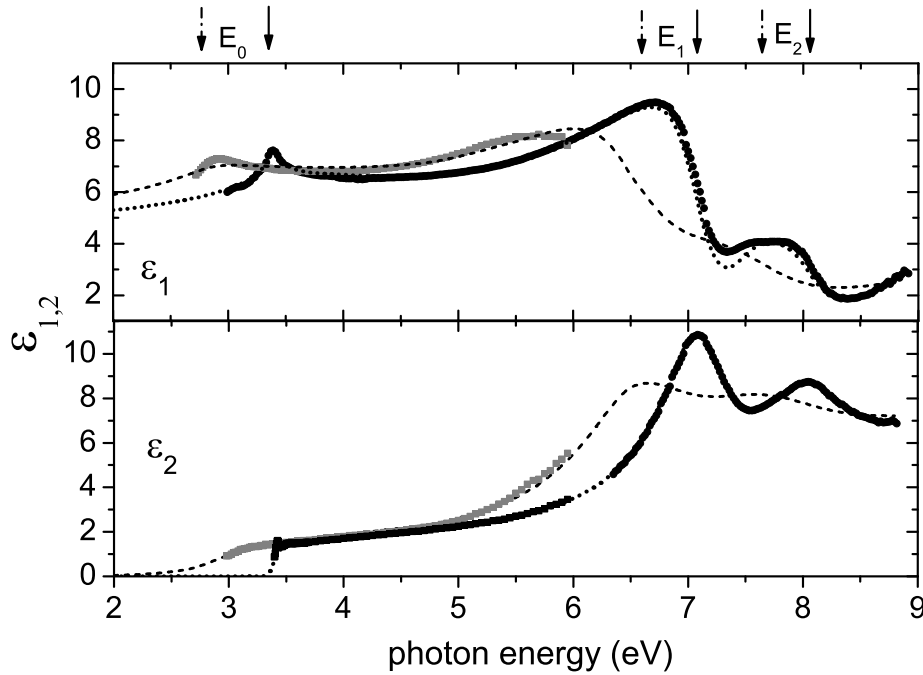
Figure 3.7: Comparison of the temperature influence onto the GaN DF at RT and 1030 °C. Arrows indicate the bulk critical points (BCP) and their shift with temperature. Black lines show ex situ measurements at room temperature while gray lines are measured in situ at growth temperature. The expansion of the high temperature dielectric function into the DUV region is achieved through a parametric dielectric function model according to [79, 106] shown in dotted lines.

1030 °C up to 6 eV (gray lines) and additionally ex situ up to 9 eV (black lines), also at room temperature. Using a temperature parametrisation model based on the observed temperature shift of the E_0 gap position and the E_1 transition (which can be

both clearly observed at temperatures around 1000 °C in the measurement range of the in situ ellipsometer) the shift of the higher interband transitions is calculated (dotted lines). Here the expansion of the high temperature dielectric function into the DUV region is achieved through a dielectric function model according to [79, 106] using a set of harmonic oscillators for the sharp transition features and a cubic spline interpolation for the relatively broad background. This model of course only describes the behavior of the dielectric function with temperature and does not include the entire physical interpretation except the reduced coulomb interaction with temperature. It allows for convenient determination of the optical properties of GaN at temperatures between room and growth temperature.

For InN such a model calculation still suffers from the knowledge of the exact dielectric properties of the material. Thus a comparable model can not be applied without high uncertainties and the respective growth rate calculations as presented in chapter 6 are based on the *in situ measured* high temperature dielectric function of InN.

Chapter 4

Epitaxial growth of GaN on sapphire (0001)

Since GaN substrates of sufficient quality and size are not yet available for reasonable prices, growth is still performed mostly on basal plane sapphire [29, 107]. Due to the large lattice mismatch and difference in thermal expansion coefficients as shown in Table 1.1 heteroepitaxy of GaN directly on sapphire leads to a poor film quality with broad FWHM of X-ray rocking curves and strong defect induced deep level yellow luminescence. Thus a quite sophisticated nucleation procedure prior to the epilayer growth was established allowing growth of well oriented thick high quality GaN layers [4, 29, 108]. The structural relation between substrate and epitaxial layer is already discussed in chapter 1. Although this nucleation process used is mature and was optimized in more than a decade it comprises several steps as sketched in Figure 4.1 which have to be controlled and understood.

- nitridation of the sapphire substrate

- low temperature deposition of a nucleation layer [1]

- a subsequent annealing step of this layer

- high temperature growth of the epitaxial layer

Therefore many parameters have to be adjusted to finally achieve a high quality epitaxial GaN layer. Most investigations on the properties and mechanisms at the nucleation layer growth have been made in the last decade. The aim was to understand the growth mechanisms in high mismatch epitaxy which could not be reached satisfactorily. It

---

[1]formerly the NL was called buffer layer [29], later this term was used for the typical 1-3 μm thick GaN layer grown prior to the active region of all kinds of devices to achieve maximum reduction in defect density.
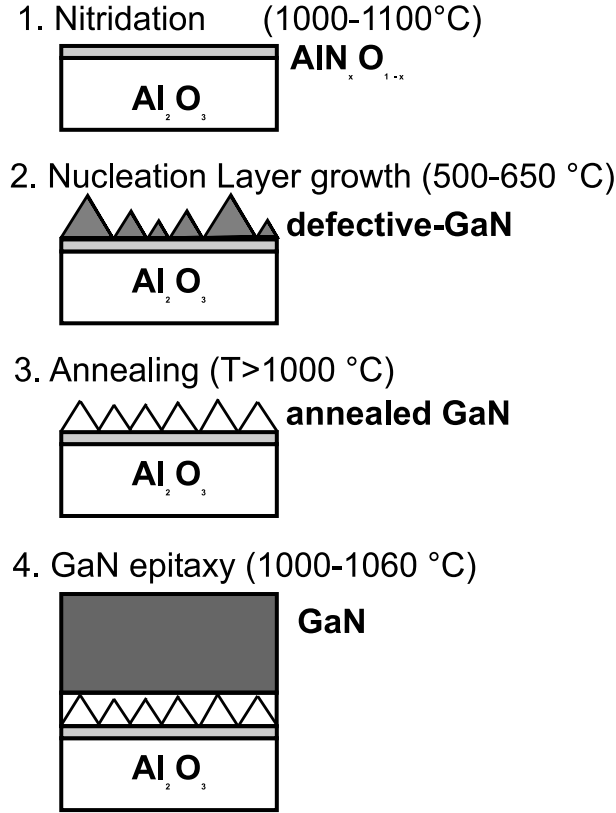
Figure 4.1: Scheme of the classical four-step growth procedure for GaN heteroepitaxy on sapphire. The nitridation (1) of the substrate at high temperature under hydrogen and ammonia flow is followed by low temperature nucleation layer growth (2) with a high gallium supersaturation. Ramping to growth temperature of the epilayer (annealing, 3) is done under reduced ammonia pressure to stabilize the nucleation layer and avoid etching while high temperature epilayer growth (4) is performed again at high ammonia flow.

turned out quickly that the nucleation layer (NL) was of poor crystal quality consisting predominantly of cubic GaN [109] with a high number of stacking faults [110–112]. A critical temperature for the formation of different crystalline phases during growth [113, 114] was reported, too. However the processes after nucleation layer growth are still subject of intense investigations [110, 115]. Most of these studies concentrated on the influence of nitridation, the nucleation layer growth itself and the subsequent annealing step on the quality of the epilayer grown afterwards [29, 116–118]. Therefore for example the nitridation time [117–119], NL growth temperature [113, 114], NL thickness [29, 120] and the annealing time and temperature [121–123] were varied in a wide range. In these investigations the resulting epilayer quality was checked with ex situ methods mostly using X-ray diffraction or photoluminescence as indicators. Al-

ready slight deviations from the optimum procedure resulted in worsening of structural and optical properties. Even when clear dependencies were found the physical mechanisms leading to the different results in epilayer quality often remained unclear. In situ characterizations have been used so far e. g. to investigate the formation process of the thin AlN layer through nitridation by use of electron diffraction methods in MBE [72, 124–126]. For MOVPE it was found that many of the processes and the optimum parameters of this empirical procedure depend on the specific growth setup and, moreover, on the actual condition of the reactor used [127]. Here in turn the nitride coating inside the reactor is supposed to reduced ammonia surface cracking which has to be compensated with an increase in NL growth temperature. Meanwhile several attempts on investigating the process of nucleation layer annealing utilizing in situ techniques like reflectance measurements have been performed also in MOVPE [115, 128–130] gaining insight into roughening and coalescence processes [128–130] and their respective activation and decomposition energies [115, 129, 130]. Therefore, these steps are investigated here in more detail using in situ spectroscopic ellipsometry as the method of choice. The aim is to track all changes in layer properties *in situ* during epitaxial growth in dependence of the growth parameters used.

In the following the nitridation process of the substrate is discussed, followed by a more detailed examination of the nucleation layer growth and annealing procedure. Finally growth of the actual epitaxial layer with respect to ellipsometry and ex situ characterization on optimized nucleation layers will be discussed.

Sample preparation

All samples were prepared in the horizontal EPIQUIP reactor described in chapter 1 on basal plane (00.1) Al_2O_3 substrates, using trimethylgallium (TMGa) and ammonia (NH_3) precursors. The substrates were first cleaned in organic solvents (acetone and isopropanol) to remove possible adhesives from the cutting process, then etched in a hot H_2SO_4:H_3PO_4 3:1 solution and finally rinsed for 2 min in deionized water. Prior to epitaxy they were thermally cleaned at temperatures of 1050°C for 10 min under hydrogen flow. The standard flux of 1 sl/min ammonia used for nucleation and epilayer growth corresponds to approx. 45 mmol/min. To prevent gallium droplet formation during NL growth always enough ammonia has to be supplied. Therefore TMGa was varied for variation of the V/III ratio at constant, high ammonia flow if nothing else is mentioned. This is a consequence of the low decomposition rate of ammonia at these temperatures. Either hydrogen or nitrogen were used as carrier gases at 100 mbar reactor pressure.

4.1   Nitridation of the sapphire substrate

A nitridation process of the sapphire substrate was recently reported by several groups to improve the optical and electronic properties of GaN layers grown in MOVPE [117–119] as well as in MBE [125], gas source MBE [72] and remote plasma enhanced MOCVD [131]. The nitridation is performed to substitute oxygen by nitrogen in a few top most mono layers of the sapphire substrate, thus forming an AlN_xO_{1-x} layer [132]. In order to obtain such a nitridation, we followed the procedure suggested in [4]. The nitridation process was then performed under an NH_3 flux of 1 sl/min (equiv. 45 mmol/min) using hydrogen as a carrier gas. Ellipsometric spectra were taken before and after the process while the changes were monitored at a transient energy of 5.5 eV during temperature increase. Ellipsometry spectra of the sapphire substrate, measured before (dash-dotted line, solid line, T = 550 °C), during (dotted line, T = 1060 °C) and after (dashed line, again T = 550 °C) the nitridation process, are shown in Figure 4.2. The first spectrum (0 in Figure 4.2) was taken on a "clean" sapphire
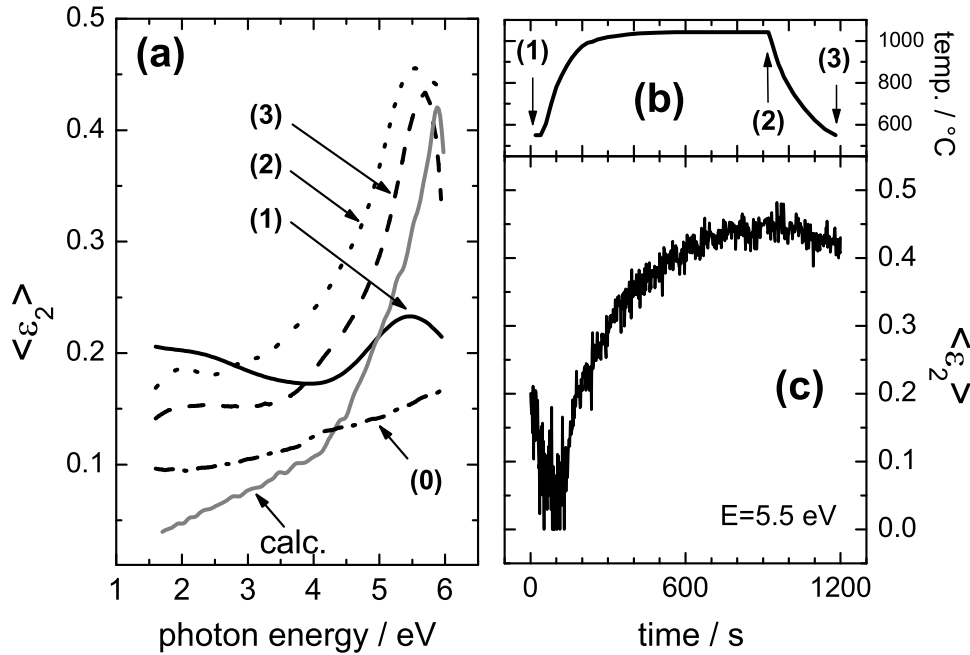

Figure 4.2: Nitridation of the Al_2O_3 substrate: (a) effective dielectric function spectra measured after high-temperature cleaning (1, solid line), during nitridation at 1060 °C (2, dotted line) and after (3, dashed line) the nitridation treatment again at 550 °C together with calculated absorption of a 4 nm AlN layer (calc. , gray line). The spectra before nitridation (0, dash-dotted) is already different from transparent sapphire ($\varepsilon_2 \simeq 0$) due to absorption from e. g. moisture. (b) Temperature ramp as applied during the nitridation procedure. (c) The transient taken at 5.5 eV illustrates the evolution with time of the whole process until formation of an AlN overlayer.

substrate after chemical cleaning at 550 °C under hydrogen gas carrier. The $\langle \varepsilon_2 \rangle$ signal of the initial surface is nearly flat in this spectral range (the band edge of crystalline γ-sapphire is reported to be 8.7 eV [100]). However, a weak structure is observable and the effective dielectric function of the sapphire is slightly different from zero as it should be for the transparent material. This is mainly due to adsorption of moisture and other contaminants during transfer into the reactor. After 10 min of high temperature cleaning at 1060 °C and cooling to 550 °C a small feature around 5.5 eV appears where the sapphire dielectric function should be without any features (1, solid line). Heating again to 1060 °C now with additional flux of 1 sl of ammonia a clear structure appears at around 5 eV (2, dotted line) which remains after cooling down to 550 °C but is shifted to a higher energy of 5.5 eV (3, dashed line). Due to the nitridation process at high temperature a characteristic absorbance signature is observed now which should be related to the nitridation process, some absorbing material formed on top of the substrate. In order to identify the origin of this modification of the sapphire surface the measured spectra are compared to calculated ones assuming AlN layer of different thickness on top of the substrate (calc., gray line).

Good agreement was found when a 4 nm thick AlN layer was assumed, as can be seen from the modeled spectrum in Figure 4.2(a, calc.). The energy shift between measured and modeled spectrum is due to the use of a room temperature AlN dielectric function being the only one available for modeling so far. Now the very small structure appearing at 5.5 eV in the "clean" sapphire signal (1, solid line) before nitridation can be easily explained: during the high temperature substrate cleaning procedure dissociated hydrogen has partially dissolved remaining GaN from former epitaxies inside the reactor/liner tube forming reactive ammonia again. This small amount of ammonia has then led to formation of a very thin nitridation layer on the substrate. This may be the reason why many researchers claim nitridation of the substrate as useless since it does not improve their epitaxial layer quality: during high temperature cleaning they have already nitrided the sapphire substrate.

From the ellipsometry transient monitored at 5.5 eV and the temperature ramping as shown in Figure 4.2(b) and (c) several conclusions can be drawn: during the first 100 seconds, between 550 °C and 830 °C, an apparent decrease in UV absorbance indicates the desorption of some adsorbate layer. Obviously the high temperature cleaning prior to nitridation did *not* prevent the surface from being covered with adsorbates, possibly from former epitaxies. Thereafter, the absorbance increases again indicating the start of the nitridation process at about 830 °C. After some exponentially developing exchange process, the nitridation can be considered as completed after 800 s, i.e. after about 600 s of a thermal treatment at 1060 °C under NH_3 purge where Hashimoto et al. [132] expected still an exponential increase in thickness for more than one hour of nitridation. But the final thickness of 4 nm achieved after nitridation is comparable to their results gained with ex situ XPS on differently prepared, long time nitrided

substrates. As the calculated ellipsometry spectra indicates a coverage of the substrate surface with several mono layers of AlN the nitridation with ammonia obviously leads to the formation of a real AlN layer instead of the previously assumed amorphous layer of Al-N-O [132]. This is in congruence with the results of sapphire nitridation with ammonia in MBE where TEM investigations revealed an abrupt sapphire/AlN interface with no evidence of formation of Al-N-O compounds [126].

Now, after preparation of the substrate, growth of the nucleation layer can be started.

4.2   Growth of GaN nucleation layer

Despite the fact that thermally activated ammonia dissociation has been reported to start at about $900\,^\circ\mathrm{C}$ [31] growth of a nucleation layer at temperatures far below is possible. Apparently the group III precursors used, their decomposition products ($\mathrm{TMGa(CH_3)}_n$) or the initially formed GaN crystals act as a catalyst for ammonia dissociation. This is supported by the fact that metals such as W or Pt are reported to act as catalysts for ammonia decomposition under non-equilibrium conditions [31]. Since no reports on the optical properties of such LT-grown GaN nucleation layers are available so far, in a first effort the use of ellipsometry for determining the optical properties during the growth process has been studied .

NL characterization

For two different NLs grown at $550\,^\circ\mathrm{C}$ with strongly different V/III ratios of 4,000 and 10,000 the respective effective dielectric functions have been measured in situ directly after growth in the reactor. From these layers the absorption-related imaginary part of the dielectric function ε_2 has been determined through a simple "scanning epsilon fit procedure" as shown in Figure 4.3. Disregarding overlayer effects and the exact layer thickness the NL dielectric function was determined in a trial-and-error way. Therefore the thickness was solely assumed to be in the range of some tens of nm and roughness effects were neglected. As a starting point a dielectric function similar to that of hexagonal GaN (compare chapter 3.3) was used and while varying this DF numerically a best fit result for the measured pseudo-dielectric function of the two NL could be obtained. Even if this procedure does not reflect the physical properties of the layers precisely it is possible to search either for similarities or big differences in their optical properties. In fact these two layers exhibit strong differences in their characteristic absorbance features. At high V/III ratios (10,000) the nucleation layer shows a well pronounced E_0 gap signature with an onset at around $3\,\mathrm{eV}$. For the nucleation layer grown with a distinctively lower V/III ratio (4,000) only a weak shoulder in the exponential absorbance tail of the respective $\langle\varepsilon_2\rangle$ spectrum can be seen at the E_0 gap position (Figure 4.3,
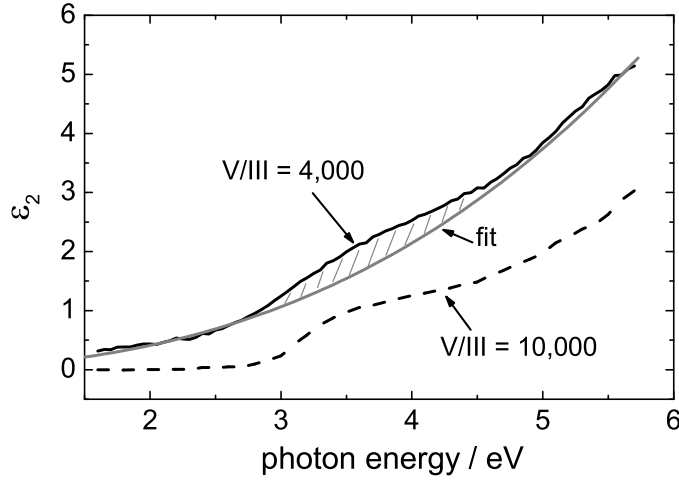
Figure 4.3: Imaginary part of the dielectric function for two NL layers grown with different V/III ratios evaluated through a simple "scanning epsilon" routine. At a high V/III ratio of 10,000 (dashed line) the layer shows a distinct E_0 gap structure around 3.2 eV while at lower ratio of 4,000 (solid, black line) this energy gap only appears as a weak shoulder (hatched area) in a more exponential like absorbance tail (referred to as "fit", gray line) and seems to be shifted in energy, too.

hatched area). For comparison an exponential absorbance spectrum is additionally depicted (Figure 4.3, "fit"). The energy shift of the band edge E_0 towards lower energy is attributed to the measurement directly after growth at slightly elevated temperatures.

Obviously the electronic and crystalline differences of thin GaN NL grown at low temperature with different growth parameters can be easily distinguished by ellipsometry. Since those differences observed are typical for layers with either a different, perturbed crystalline structure or an increased defect density a more detailed analysis shall give insight in the dependencies of the NL structure from the growth parameters. Therefore a systematic variation of the growth parameters will be performed and now the exact properties of the nucleation layer like overlayer roughness, thickness, etc. will be taken into account. Also the exact position of the band edge will play an important role for characterization of their properties and has to be determined precisely. But before this can be done the optimum NL thickness must be determined and cross-checked.

Optimization of NL thickness

As mentioned in the beginning one important criterion for an optimized epilayer growth which has to be controlled is the absolute thickness of the nucleation layer [4, 29, 108]. Thus at first this parameter had to be fixed for further investigations. Furthermore a first characterization of the GaN epilayer grown in our apparatus has to be given to ensure that the results gained in each growth step are close to what is state of the art. Therefore the nucleation layer thickness was varied simply by change of the growth time, holding the V/III ratio constant. Thereafter a $1\,\mu$m-epilayer was grown on each nucleation layer, again with a constant V/III ratio. The dependence of the epilayer quality from NL thickness was characterized via $\omega - 2\Theta$ XRD-scans of the symmetric GaN(0002) reflection [2] as shown in Figure 4.4. Obviously a nucleation layer growth time around
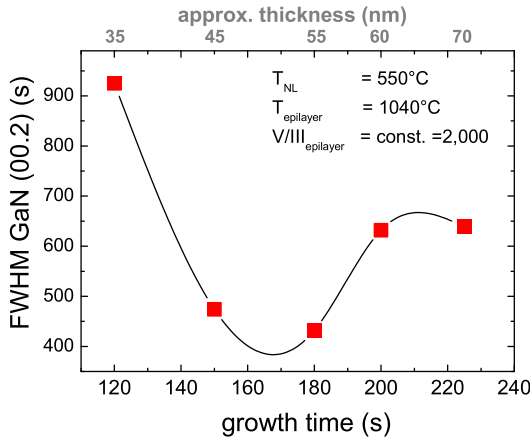
Figure 4.4: FWHM of XRD-Ω-scans (rocking curve) of the symmetric GaN(0002) reflex of $1\,\mu$m GaN epilayers grown on nucleation layers of different thickness. Variation in thickness was achieved through variation of NL growth time. The corresponding thickness values depicted on the top axis (gray) are derived from ellipsometric measurements. The spline is a guide to the eye.

$180\,$s (according to 45 nm as derived from the ellipsometric spectra and SEM images) leads to an epilayer with the narrowest FWHM of the (0002) reflection of around 400 " indicating a layer low in defects. Since the epilayer thickness is only $1\,\mu$m this FWHM value is acceptable for GaN grown in high mismatch epitaxy (compare [122]). Best values achieved are around 100 " for a layer thickness of more than $2\,\mu$m and less for laterally overgrown (LEO/ELOG) material.

4.2.1   Influence of the V/III ratio

With this experience a first systematic study on the nucleation layer properties grown under various conditions could be started. This is of importance since for example Kim

---

[2]A thorough investigation of all defect types, especially threading dislocations, would require additional XRD scans along asymmetric planes. For our purpose the symmetric scan along (0002) direction is sufficient.
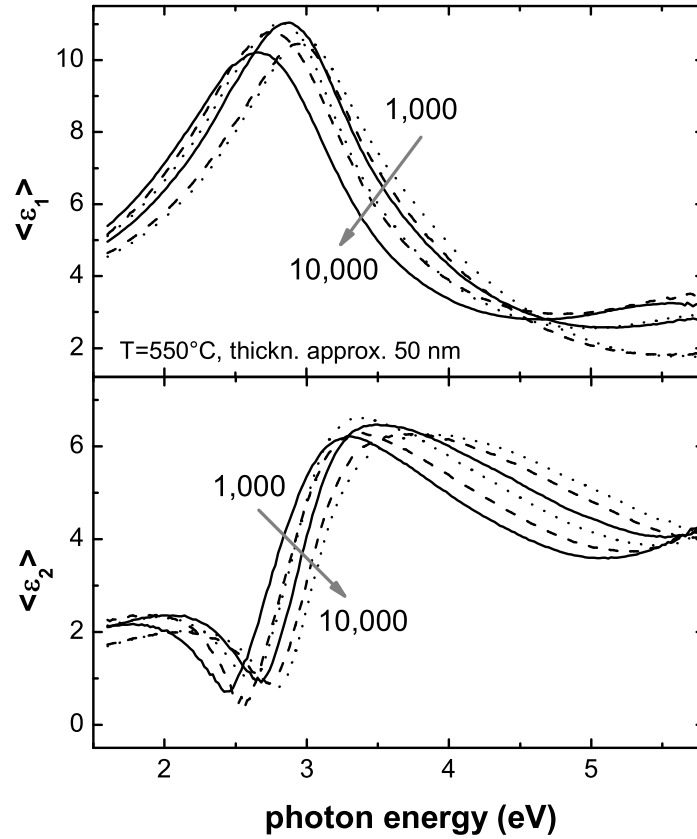
Figure 4.5: Real and imaginary part of the effective dielectric function of six as-grown GaN nucleation layers recorded after deposition under ammonia stabilization at 550 °C. The V/III ratio was changed from 1,000 to 10,000 by varying the gallium partial pressure while growth time was reciprocally adjusted to achieve layers of similar thickness. Therefore the interference related structures of all effective dielectric functions show apparent similarities.

et al. reported that a decreased V/III ratio achieved by an increase of the gallium flow leads to an increased growth rate. The increased NL growth rate reduces the dislocation density in the subsequently grown GaN epilayer and thus improves significantly the epilayer quality [133]. However, the authors have not given an explicit explanation for this behavior. Figure 4.5 shows the effective dielectric function $\langle \varepsilon \rangle$ of a set of six as grown GaN nucleation layers deposited at 550 °C under various V/III ratios in the reactor. The V/III ratio was varied by changing the gallium partial pressure, while the ammonia partial pressure was kept constant at 25 mbar (according to 45 mmol/min) to

provide sufficiently active nitrogen to the surface and hence suppress gallium droplet formation. All layers were grown at 550 °C. Because growth is limited through the gallium partial pressure the growth time was adjusted reciprocally to the gallium partial pressure with the aim to obtain nucleation layers with a comparable thickness. SE transients measured during growth allowed for growth control and similar transient line shapes guaranteed similar layer thickness. This can be seen in Figure 4.8. All $\langle \varepsilon \rangle$ spectra of the thin stabilized nucleation layers recorded after deposition are dominated by a broad interference contribution due to light penetration. The energetic positions of minima and maxima of the spectra are affected by both, thickness and optical density of the layers. Since they all appear similar their thickness is expected to be similar.

For a precise evaluation of the in situ measured ellipsometry data an optical model consisting of a multi layer stack was used consisting of a semi infinite sapphire substrate, a GaN layer, rough GaN and a vacuum approximating the gas ambient. The inset in Figure 4.6, top shows the respective layer stack assumed for complete description. The rough GaN on top accounts for the morphology of the nucleation layer. The pseudo dielectric function was then calculated for the entire stack in terms of an analytical model function described by the Tanguy approximation which provides an analytical expression of the dielectric function of weakly bound Wannier excitons. The contributions of all bound and unbound states were taken into account including a lorentzian broadening Γ of the energy levels (see also [101, 102] and chapter 3). This broadening allows for numerical determination of the crystal quality of the investigated layer. An increase in Γ is directly related to a reduction of the carrier lifetime caused by defects or a perturbed crystalline structure.

The parameters were adjusted to fit the calculated effective dielectric function to the measured data in the following two step procedure:
in the first step the band edge position E_0 and the respective broadening Γ are calculated while restricting the measured data to an energy range of 2 to 4 eV since the Tanguy approximation is only valid close to the band edge. Second, using the so determined values for E_0 and Γ the data range was extended to 6 eV to include the thickness related interference structures for exact determination of the NL thicknesses. The roughness on top was described by a Bruggemann effective medium approximation (EMA, see also chapter 3.2.2) assuming a 50 % mixture of GaN and voids [86] using the same optical constants as for the GaN NL below. In Figure 4.6 (top) the results are shown exemplarily for two nucleation layers. There the calculated pseudo dielectric function is given by the dotted curves, demonstrating the excellent description of the optical properties through the applied model with the measured ones (solid line). The corresponding bulk dielectric functions of four different NLs are also shown in Figure 4.6 (bottom). The band edges of all nucleation layers appear to be below but close to 3 eV (at 550 °C) and the adsorption edge is significantly broadened compared to what is usually observed for direct III-nitride semiconductors (compare e. g. [134]). Significant differences can
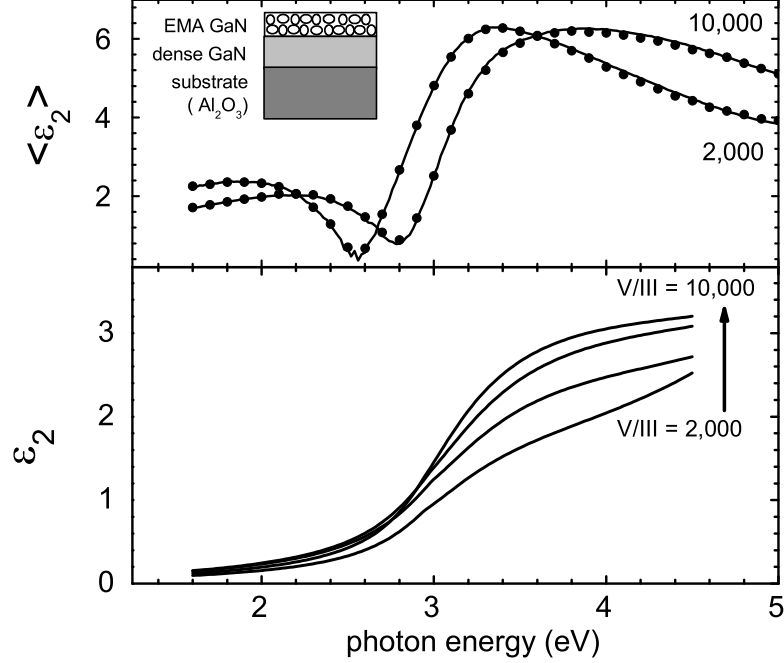
Figure 4.6: The top graph shows the measured effective dielectric function $\langle \varepsilon_2 \rangle$ of two as-grown GaN nucleation layer from Figure 4.5 (solid line) vs. the calculated effective dielectric function according to the model described in the text (dots). The results agree quite well. The inset shows the assumed sample structure for the model. Bottom: the corresponding bulk dielectric functions ε_2 determined from the $\langle \varepsilon_2 \rangle$ functions for four NL are shown.

be already distinguished from the line shapes giving rise to the assumption that the band edge is apparently most pronounced at high V/III ratios, i. e. for layers deposited with a low growth rate [120, 135]. Therein a tendency towards more cubic material is observed for thin NL and with increasing thickness hexagonal islands tend to form on top. As already mentioned the applied model allows to obtain values for the band edge position E_0 and the broadening Γ. From these results several conclusions can be drawn which are illustrated in Figure 4.7. Obviously the broadening parameter Γ decreases with decreasing growth rate (increase in V/III ratio) showing an increase of crystalline quality. This can be easily understood since lower growth rates allow for more surface ordering and thus a decrease in defect density. At the same time the NL band edge increases for lower growth rates showing a higher amount of hexagonal proportions in the NL. This is similar to the findings of Wu et al. [110, 112] where both phases, cubic and hexagonal are observed in TEM and the occurrence of the cubic phase in the NL is accompanied by a high density of stacking faults. The number of these stacking faults is reduced during subsequent annealing of the NL when additional hexagonal phases
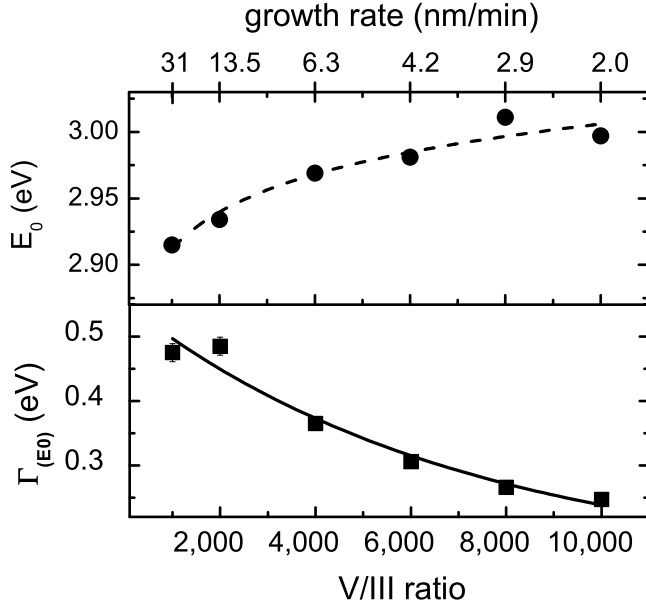
Figure 4.7: Energetic position of band edge E_0 and band edge broadening Γ (measured at 550 °C) for different NL grown with different V/III ratios. With decreasing growth rate (increase of V/III ratio) the NL band edge rises showing an increase in hexagonal structures while the band edge broadening is reduced.

are formed. It can therefore be concluded that changing the growth rate strongly affects the relation between the cubic and the hexagonal fraction in the NL. With an increase in growth rate the NL dielectric function shows a higher amount of cubic material in the layer.

The possibility of an increase of randomly oriented hexagonal crystals can be ruled out since this only leads to an increase of the broadening. No influence on the band edge should be observed then except for confinement effects. In case that the crystals formed during NL growth are small enough resulting in an increase in band gap energy similar shifts in energy should be observed. But Cheng et al. [113] found that the cubic phases always occur in grain boundary areas leading to a direct relation between the observed cubic proportion and the number of stacking faults together with grain sizes of more than 30 nm. This size is above what one would expect for confinement energy shifts. Additionally the existence of cubic phases can be derived from the absolute value of the E_0 position (see Figure 4.17) where a value much closer to that of cubic GaN than of hexagonal GaN is observed. This is also in congruence with the high cubic proportions found in NL from Wu et al. [111] and Munkholm et al. [109]. Since very low nucleation layer growth rates strongly influence (worsen) the quality of the subsequent hexagonal GaN epilayers [133] this must be related to the different crystalline phases occurring in the NL for the different growth rates. This will be explained later in more detail in the following section 4.3 with its consequences to the improvement in epilayer quality.

4.2.2   Influence of the reactor setup

Spectroscopic ellipsometry also allows to determine the growth rates of the NLs in situ during deposition by evaluating transients measured at a fixed photon energy. In Figure 4.8 growth transients recorded at a photon energy of 5 eV are shown. They are displayed as values of cosΔ and tanψ (see chapter 2) which allows improved visibility of the growth start. The value of 5 eV for the transient energy is a compromise between high optical absorption of the thin layer while at the same time measuring with nearly temperature independent $\langle \varepsilon_1 \rangle$ and $\langle \varepsilon_2 \rangle$ values located on a plateau of the optical dispersion below the steep incline to the next high energy transition E_1 (see chapter 3.3 for more details). The high absorption reduces the influence of growth oscillations in the transients but since the layer is very thin (some tens of nm) still enough light penetrates through it to observe thickness related interferences. A set of
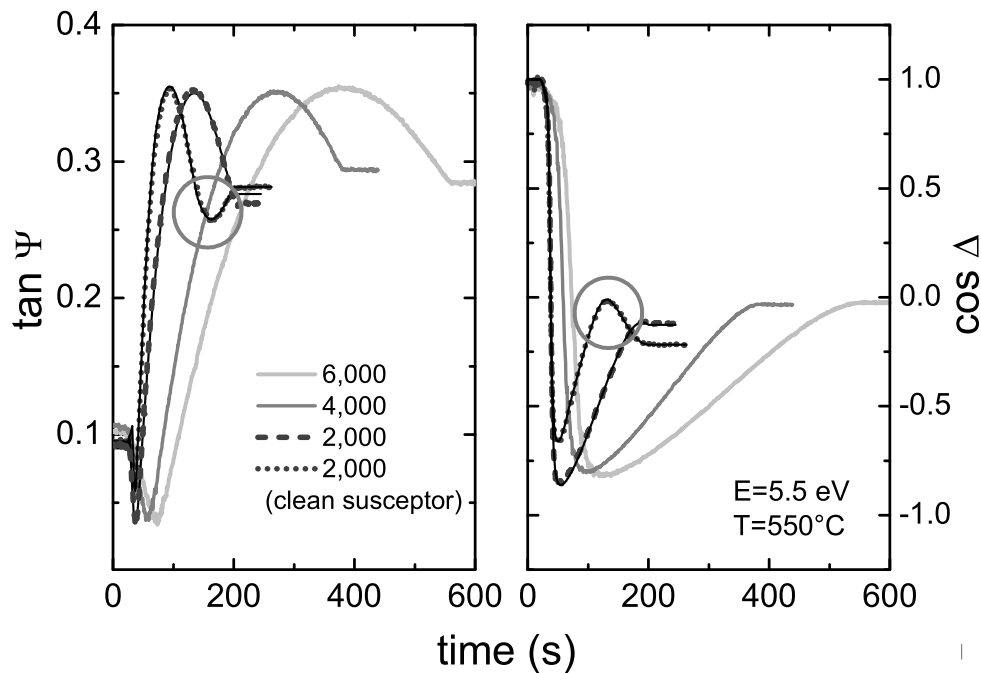
Figure 4.8: Growth transients of tanψ and cosΔ taken at 5 eV for four different nucleation layers. Variation of the V/III ratio (from 2,000 to 6,000) by a change in TMGa flow shows the expected change in growth rate while the general shape of the transients is similar. Additionally for the V/III ratio of 2,000 a different growth behaviour is found when the growth system (susceptor and reactor) is thermally etched under hydrogen prior to growth (denoted as "clean susceptor", dotted line). Solid lines for V/III ratio of 2,000 show the respective calculation of the transients and their agreement with the measurement (dotted/dashed).

as measured growth transients taken at 5 eV together with the respective calculated ones

(dotted/dashed curves) is shown in Figure 4.8. Since the aim was to grow NLs of comparable thickness through adjusting growth time reciprocal to the variation in gallium partial pressure all transients are similar in shape but stretched on the time scale. For the two NLs grown with a V/III ratio of 2,000 the line shapes differ significantly. While all layers grown in a GaN coated susceptor/liner tube setup show only one interference maximum (in $\tan \psi$) which appears after appprox. 30 nm layer thickness the one grown in a clean setup shows a second minimum (circles in Figure 4.8). In this case prior to nucleation layer growth the reactor and susceptor were thermally etched under hydrogen flow at 1040 °C for 15 minutes. Obviously the NL growth behavior is significantly different when a clean susceptor is used leading to significantly thicker NLs. To investigate these differences and their origin a detailed evaluation of the growth transients is necessary.

To achieve this, the time dependent evolution and formation of the multi layer stack described before in Figure 4.6 had to be evolved assuming a growth model similar to what has been observed by Degave and co-workers [120]: the growth is initialized by formation of a roughness (without any GaN related physical properties) which can be interpreted as a seed. Through growth and coalescence of these seeds a closed GaN nucleation layer is formed with some roughness on top. When growth proceeds the closed layer increases in thickness while the roughness remains nearly unchanged. This is sketched in Figure 4.9.
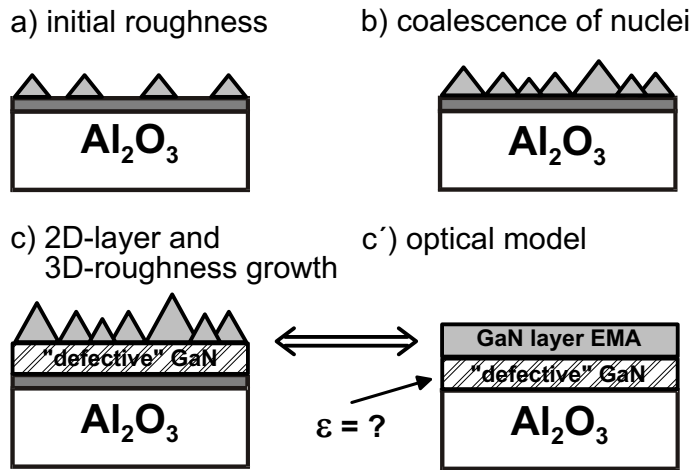

Figure 4.9: Growth model assumed for evaluating SE transients during NL growth. After formation of an initial roughness (a) the seeds start to coalesce (b) and a dense NL rich in defects forms (c). The model stack for final NL spectra calculation is shown in c'.

A proper description of the growth starting point requires the assumption of a nonlinear growth rate of the initial roughness formation on sapphire. This is similar to what has been observed for GaN growth in MBE. There, initial growth was reported to consist of two regimes, a highly nonlinear and a subsequent linear mode [124]. Therefore we used two EMA layer (see chapter 3) of the same optical properties with slightly different growth rates (separated by the dashed lines in Figure 4.11). The result of this

transient calculation is given in Figure 4.8 where the solid lines show the calculations together with the respective measured transients demonstrating the agreement between model and measurement. Thus the evolution in layer thickness can be estimated and NL growth rates can be determined easily. In Figure 4.10 the dependence of the growth rate on the gallium partial pressure at constant ammonia flow is given. For a susceptor coated with GaN from previous growth runs the growth rate is constant during deposition and scales approximately linear with the Ga partial pressure (black curve, Figure 4.10). Using a "clean" susceptor (obtained after a 15 min. bakeout at 1040 °C under hydrogen) a completely different growth behaviour is found: in the beginning the growth rate is increased nearly by a factor of two and decreases during the 3 min. deposition time approaching the same value obtained by using a GaN coated susceptor (grey curve, Figure 4.10). As these differences of the deposition conditions are already ob-
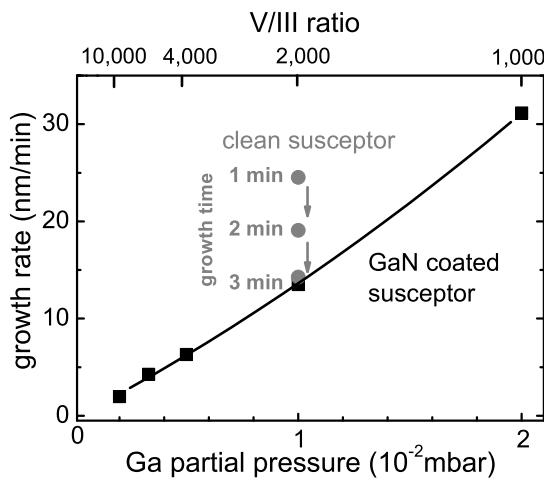
Figure 4.10: Growth rate of nucleation layers at 550 °C deposition temperature and constant ammonia flow depending on the Ga partial pressure for GaN coated susceptor (black rectangles) and hydrogen etched susceptor (gray circles). The drastic change of the growth rate during deposition is indicated with arrows. The data were determined from transients of $\cos\Delta$ and $\tan\psi$ shown in Figure 4.8.

served at the initial stages of growth they lead to significantly different layer thickness for the same deposition time. For identical gallium fluxes we obtain total thicknesses of 62 nm and 48 nm after 3 min. deposition time using a "clean" and a "GaN coated" susceptor, respectively. The detailed evolution of the nucleation layer thickness is given in Figure 4.11. To simulate the decrease of the growth rate for the "clean" susceptor we gradually approximated the temporal evolution with three different values (dotted lines in Figure 4.11, left image). We find a strongly nonlinear growth behavior similar to that already reported for MBE growth [124]. In both cases the onset of deposition is initially described by a rough layer only and the nuclei coalescence for formation of a dense layer is significantly delayed. In case of the clean susceptor it is 13 s instead of 9 s for the GaN coated one. In both cases the growth rate of the rough layer slows down immediately after the onset of coalescence leading to an almost constant thickness of the rough part of the NL during deposition with solely the dense layer growing.
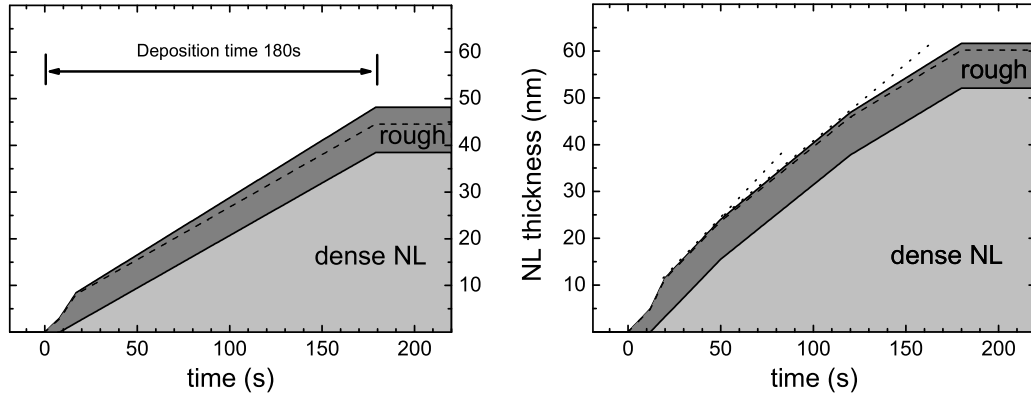
Figure 4.11: Evolution of the nucleation layer thickness for deposition on sapphire at 550 °C and V/III ratio of 2,000 using a coated (left) and a clean susceptor (right). The solid lines give the total layer thickness. The dashed line separates the parts of the rough layer with the different growth rates necessarily assumed to describe the nonlinear growth behavior at the onset of deposition. The change in growth rates in case of a clean susceptor (right) is indicated with the dotted lines to visualize the different slopes.

This growth behavior can be interpreted as a 3D → 2D growth mode transition when coalescence takes place. From the significantly different delay times (9 s vs. 13 s) for the coalescence onset it can be concluded that the nuclei density varies with the reactor and/or susceptor history.

In case of the clean susceptor the density may be either lower or the nuclei size is larger, something which can not be deduced from the ellipsometry transients only. But taking into account that during the previous nitridation experiments a quite thin AlN layer was already found on the sapphire after high temperature cleaning of the substrate in hydrogen carrier gas (see beginning of this chapter, Figure 4.2) we are able to understand the differences in coalescence delay: the substrate thermally cleaned in the GaN coated reactor has a very thin AlN overlayer which acts strain reducing with the consequence of smaller nuclei forming on the substrate surface but higher in density. The "pure" sapphire substrate instead increases strain in the GaN nuclei leading to larger grains of lower density. With larger nuclei coalescence is significantly delayed since their mutual distance is expected to be larger. Assuming the thin AlN over layer to be the so called "wetting layer" this can be interpreted as a Stranski-Krastanow growth mode while growth on the "really clean" sapphire proceeds in the Vollmer-Weber mode.

Subsequently, the total growth rate observed is much higher for the clean than for the GaN coated susceptor only aiming to a faster growth of the dense layer, see Figure 4.10. Obviously an already existing GaN coating acts as a trap for the dissociated

precursors and leads to significant depletion in the gas phase. This depletion is not observed in the early stages of growth in the clean system. Thus the dependence of the growth rate on the condition of the reactor has to be taken into account to achieve a well defined nucleation for the epitaxy of GaN on sapphire. Because the roughness develops nearly independently from the reactor conditions except for the coalescence delay at growth start it is clearly *not* the pure morphology influencing the subsequent epilayer growth and the quality of the epilayer as often cited in literature [122, 128]. Thus reproducible growth of high-quality, NL thickness sensitive GaN epilayers requires a growth setup which has to have comparable conditions for each growth run.

To confirm the roughness of the nucleation layer obtained in situ and thus confirming the assumed optical model we also measured the surface morphology post growth using atomic force microscopy. The dependence of the roughness determined by AFM on the Ga partial pressure and the associated growth rate is compared to the ellipsometry data in Figure 4.12 and Figure 4.13. The tendency of increasing roughness with
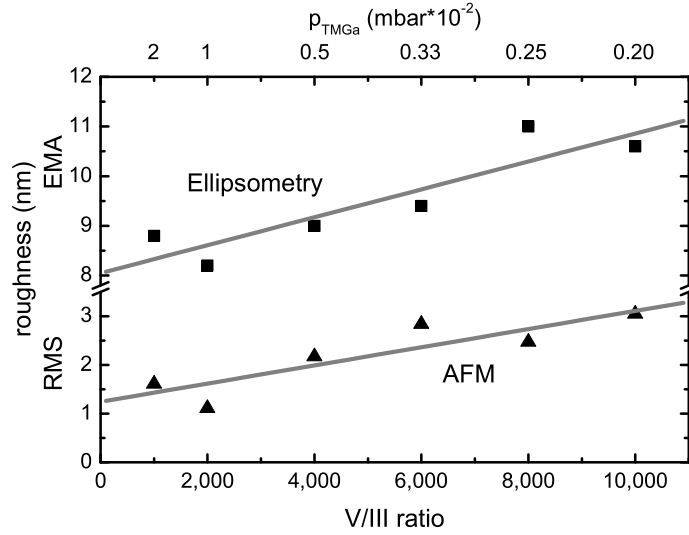

Figure 4.12: Comparison of NL roughness determined in situ using spectroscopic ellipsometry (upper graph) and post growth using atomic force microscopy (lower graph).

lower Ga partial pressure and hence decreased growth rate is observed in both, in situ and ex situ measurements, and was also reported in previous AFM studies [133, 135]. One explanation is the preferred growth of larger structures when less gallium species are offered and their mobility increases [133]. The differences in the absolute values and the slope of in situ and ex situ data originate from different definitions of the determined roughness. AFM determines a root-mean-square (rms) roughness which
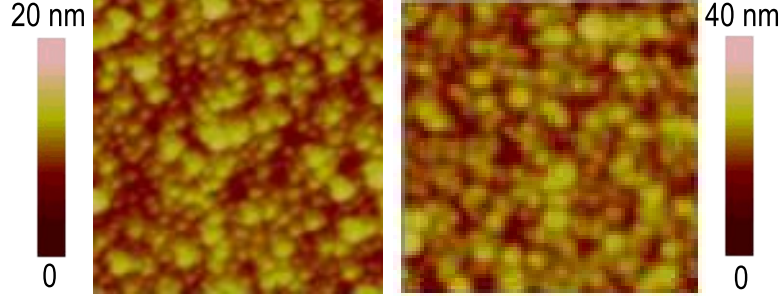
Figure 4.13: $1\mu m^2$ AFM images of the corresponding layers to Figure 4.12 for V/III ratio of 1,000 (left) and 10,000 (right) clearly showing the increase of island size with lower growth rates. The height scale is given in nm

depends on the size of the scan region and gives a weighted average. The minimum size of the measured structures and hence the rms roughnesses are also affected by size and geometry of the AFM tip. Ellipsometry yields a roughness based on the effective medium approximation which assumes idealized void inclusions in the layer and also gives the *total* thickness of this EMA layer. For 50 % voids inclusion in the host material this equals a factor of two. A more detailed description of EMA theory is given in chapter 3.2.2.

4.3   Annealing of the nucleation layer

Annealing of the nucleation layer is a crucial step in the GaN growth procedure. The necessary surface stabilization for in situ measurements was achieved through reduction of ammonia flow to 22 mmol/min which is half the value for NL growth while purging with nitrogen carrier gas. The whole annealing process was monitored measuring spectra in intervals of 90 s which is the limit of the apparatus for fast spectral measurements. The temperature ramping was chosen in the range of 1 °C/s for realistic epitaxy conditions. The layer morphology was additionally studied post growth using scanning electron microscopy (SEM) and atomic force microscopy (AFM). Using the four layer model given in the previous section to describe the in situ recorded pseudo dielectric function we find that a significant smoothing of the nucleation layer starts at temperatures of 800 °C (Figure 4.14). The smoothing proceeds through a decrease of the thickness of the rough layer while the thickness of the dense layer increases, maintaining a nearly constant total thickness. Hence GaN does not desorb during the temperature increase from 550 to about 1040 °C in N_2 and reduced ammonia pres-
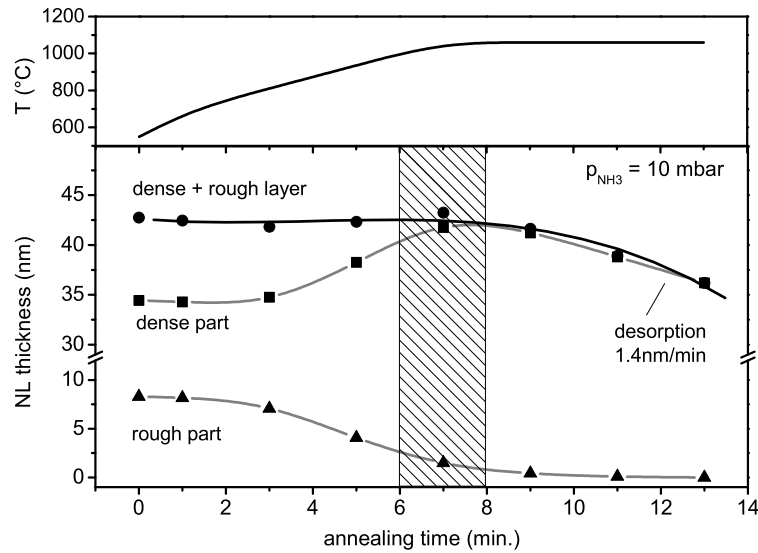
Figure 4.14: Gradual change of the dense and rough fraction in the nucleation layer during annealing as determined from the dielectric function model. The upper graph shows the temperature ramping. Layer desorption increases after structural transformation has taken place (rectangle region) with a final rate of 1.4 nm/s.

sure but is obviously redistributed. At 1040 °C after the nucleation layer is completely smoothed a slow desorption of it is observed with a rate of 1.4 nm/min. Under these conditions, the nucleation layer is completely desorbed after approximately 30 min. The effect of the annealing procedure monitored through the evolution of the layer thickness (Figure 4.14) can be also seen in the SEM image of the surface morphology shown in Figure 4.15. Here cross section images of two representative samples are shown taken under an angle of 85 °. The cross sectional view was achieved by simple cleavage of the substrate. Electrical conductivity of the NL was obtained by sputtering of a chromium layer of ≈2 nm in thickness. From the SEM images the thickness of the as grown NL can be estimated to approximately 50 nm in good agreement with the thickness as determined by ellipsometry. The annealed layer is much smoother with an apparently higher extent of island coalescence while its thickness seems not to be affected. The rms roughness, measured by AFM, is ≈3 nm for the as grown and 0.6 nm for the annealed sample.

At a first glance all this is strongly contrary to what has been found by ex situ AFM investigations from Lada et al. [115] and from Koleske et al. [129] were an increase of roughness during annealing was observed in AFM. But in both cases the authors stopped investigating the structural properties after their *ideal* annealing time. One year later a more detailed investigation, again from Koleske et al. [130], concluded that after
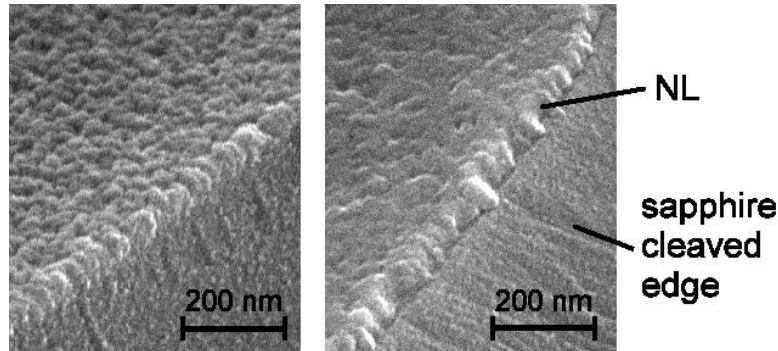
Figure 4.15: Surface morphology of as-grown (left) and annealed nucleation layer (right), imaged at a cleaved edge by scanning electron microscopy. The layer is obviously smoothed after annealing.

ripening and coalescence of nuclei on the NL surface at high temperatures decomposition of these nuclei takes place. This decomposition leads to a significant smoothing of the NL again. They also observed a material desorption with a maximum desorption rate of 0.36 nm/min under ammonia flow at 900 °C substrate temperature. This rate is significantly (almost four times) lower but it can be explained with the highly accelerated etching process through ammonia decomposition at increased temperatures (1060 °C instead of 900 °C).

During the temperature increase the change of the thickness ratio from dense to rough layer is already known to be accompanied by a structural change [109–111, 136] in the NL. TEM investigations revealed increase in grain sizes and ordering forming large hexagonal crystals in the sapphire/epilayer interface. This phenomenon can be clearly tracked within the ellipsometry spectra by the temperature dependent shift of the band edge energy E_0 of the NL during annealing. Here the temperature increase affects ellipsometry spectra in two ways: firstly, a thermal induced shift of the bulk critical points to lower energies originating from the combined effect of lattice expansion and electron-phonon interaction [89] is observed (see also chapter 3.3). Secondly, changes of the layer itself, e. g. re-crystallization lead to changes of E_0. For a detailed analysis of the influence of layer structure they have to be separated.

In the case of high temperatures (which means clearly above room temperature) the temperature dependence can be linearly approximated (Figure 4.16, right image). Comparing the absolute band edge position of the NL before and after annealing a difference of 0.12 eV (Figure 4.16, left image) is determined which has to be attributed to the thermally induced changes in the layer structure due to annealing. Taking this difference of 0.12 eV into account we calculate a temperature dependent slope of the E_0 shift of -6.6×10^{-4} eV/K in the range from 550 to 1060 °C. This is in reasonable agreement with the measured temperature shift for a hexagonal epilayer under ammonia stabi-
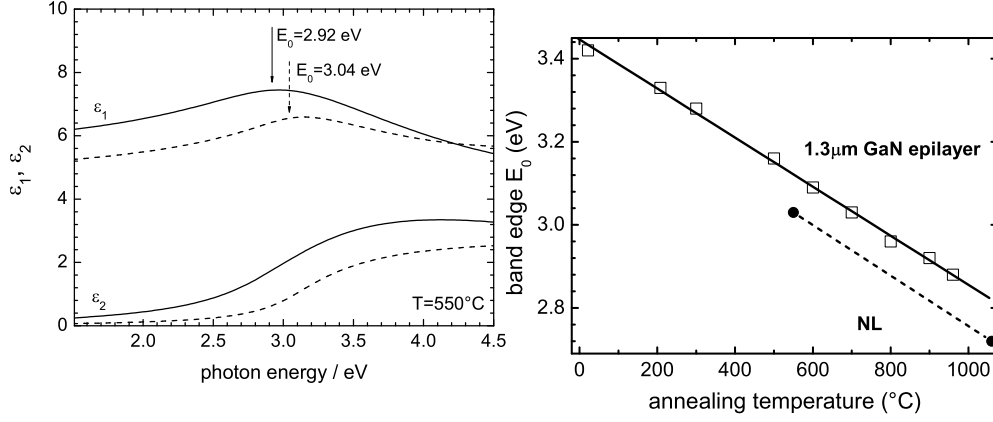
Figure 4.16: Left: energetic position of the band edge E_0 of the NL before (straight lines) and after annealing (dotted lines) measured at 550 °C. Arrows indicate the shift of 0.12 eV of the band edge position related to the structural changes in the layer. Right: annealing of a hexagonal GaN layer gives a temperature induced shift of the E_0 transition of -5.9×10^{-4} eV/K (squares) with no indication of a non-linear behavior. As similar shift is observed for the NL (circles) at high temperatures.

lization from room temperature up to 960 °C (Figure 4.16, right image). Here a linear slope of -5.9×10^{-4} eV/K is determined with no indication of a non-linear temperature behavior within the range of the error limits. [3] A similar linear regression for higher temperatures up to 565 K was already reported in earlier measurements of the shift of the E_1 and E_2 transition energies for GaN from Logothetidis et al. [138]. Absorption edge measurements from Su et al. [139] performed on thick GaN in the range from room temperature to 964 °C also clearly revealed a linear behavior with slopes ranging from -3.8 to -8.1×10^{-4} eV/K. The low precision of their measurements resulted in a wide spread of the linear factor but no indication of a nonlinear behavior was found. Now this temperature dependent shift can be subtracted from the calculated band edge position of the NL during annealing. The remaining changes after temperature correction should be solely attributed to structural changes inside the layer as depicted in Figure 4.17, bottom graph. The reference temperature is chosen as 550 °C since this is the start and end temperature of the annealing cycle. Obviously a strong increase of the corrected E_0 band edge position during annealing can be observed. Using the temperature correction of -6.6×10^{-4} eV/K to determine the room temperature value for E_0 of the NL grown with the lowest V/III ratio (according to highest growth rate)

---

[3]Usually a non-linear temperature behavior of the band gap shift is observed in the temperature regime between room temperature and 0 K [137]. Thus for the temperature range investigated here such a linear regression is not contradictory.
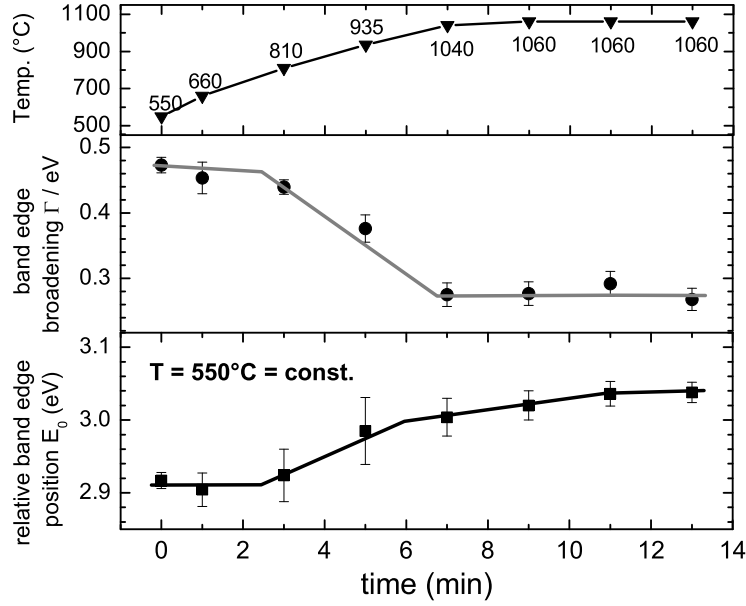
Figure 4.17: NL Band edge position E_0 and band edge broadening as a function of anneal-
ing temperature corrected for linear temperature shifts with respect to 550 °C (linear slope of
-6.6×10^{-4} eV/K). The structural change begins at 800 °C and is almost completed at 1040 °C.
Changes from cubic to hexagonal phases are observed with increase in crystal quality. Due to
the temperature correction the E_0 values shown here cannot be directly compared to the values
in Figure 4.16, right image.

we find $E_{0(RT)} = 3.24$ eV. This is in excellent agreement with the literature values for
cubic GaN (e. g. 3.24 eV in [134]). With decreasing growth rates of the NL this value is
slightly increased. The NL investigated here consists mainly of cubic GaN which trans-
forms into hexagonal GaN during annealing. This transformation starts at about 800 °C
and is completed already at 1040 °C. The slight increase of the band edge value at a
constant temperature of 1060 °C might be attributed to the material desorption which
takes place, leading to smaller crystallites resulting in a size-determined E_0 shift.

Together with the mechanisms of layer smoothing as shown in Figure 4.14 the
whole process can be understood and explained in detail:
The band edge position E_0 changes from a value close to that of cubic GaN to the value
of the hexagonal modification ($E_0 = 3.41$ eV) during annealing. This is accompanied
by an increase of the dense NL thickness while the roughness layer nearly vanishes.
Desorption of material is clearly observed after the structural change has completed
while the layer is still held at 1060 °C for several minutes. Thus the structural change
at lower temperatures must be accompanied by material transport from e. g. inside the
layer to the surface [109, 110, 112]. Obviously this desorption starts from the less sta-

ble cubic phase in the dense layer by transport of gallium atoms to the surface. There the gallium atoms are incorporated into the more stable hexagonal phases on top of the layer. The decrease of the broadening parameter Γ during the material transport indicates the formation of an ordered hexagonal phase in the NL. At the end solely desorption is observed when no further rearrangement from cubic to hexagonal phases can take place. Therefrom it can be deduced that an annealing procedure with a long-time temperature treatment above $1000\,^{\circ}$C will not improve the NL properties. This explains why long-time annealing worsens the quality of subsequently grown epilayer.

4.4   Growth of GaN epitaxial layer using ammonia

Growth of thick GaN epilayer is performed after the complete characterization of the different stages in nucleation layer growth and annealing to confirm the procedure. Therefore the growth process is started directly after nucleation layer annealing by switching the TMGa flux on while changing the carrier gas to hydrogen and instantaneously increasing the ammonia flow to $1\,$sl/min. The growth rate of the epilayer is determined in situ by the occurrence of Fabry-Perot interferences in the ellipsometry spectra $\langle \varepsilon \rangle$. A typical value is $1.2\,\mu$m/h. After one hour of growth the non-oxidized layers are characterized in situ by SE and ex situ with low temperature photoluminescence, XRD and AFM for evaluation of the layer quality. The corresponding photoluminescence spectrum is shown in Figure 4.18, left image. A He-Cd laser with $325\,$nm wavelength corresponding to $3.81\,$eV was used for excitation. At $4\,$K a strong donor bound exciton emission (denoted I_2) dominates the spectrum with a FWHM of $5\,$meV at $3.475\,$eV. In the logarithmic scale (inset of Figure 4.18) additionally the luminescence of free Excitons X_A and X_B on the high energy side can be clearly resolved. Their corresponding FWHM is only $2.5\,$meV and they are shifted in energy by $7.9\,$meV and $16.4\,$meV from the maximum of the bound exciton line. Still some defect related yellow luminescence (YL) can be found around $2.2\,$eV. After cooling the sample to room temperature an interesting feature can be observed in the corresponding ellipsometry spectra of the as-grown and oxide-free GaN. Figure 4.18, right side shows the appearance of an additional absorbance peak around the band edge region (dashed line). Therefore the band edge was calculated using a simple one-oscillator model restricted to $3.4 \pm 0.5\,$eV (dotted line). A gaussian line fit reveals that the course of the dielectric function can be ascribed to the existence of an additional oscillator with a FWHM of approx. $45\,$meV located at $3.42\,$eV (Figure 4.18, dashed line). Summing up the calculated band edge and the absorbance peak oscillator the good agreement between measurement (gray squares) and calculation is obvious (straight line). This peak is only resolved for as-grown non oxidized layers and not correlated with layer interferences. It is obtained for several samples of higher quality and its width remains totally unaffected by variation of the layer thickness, in contrast to the Fabry-Perot
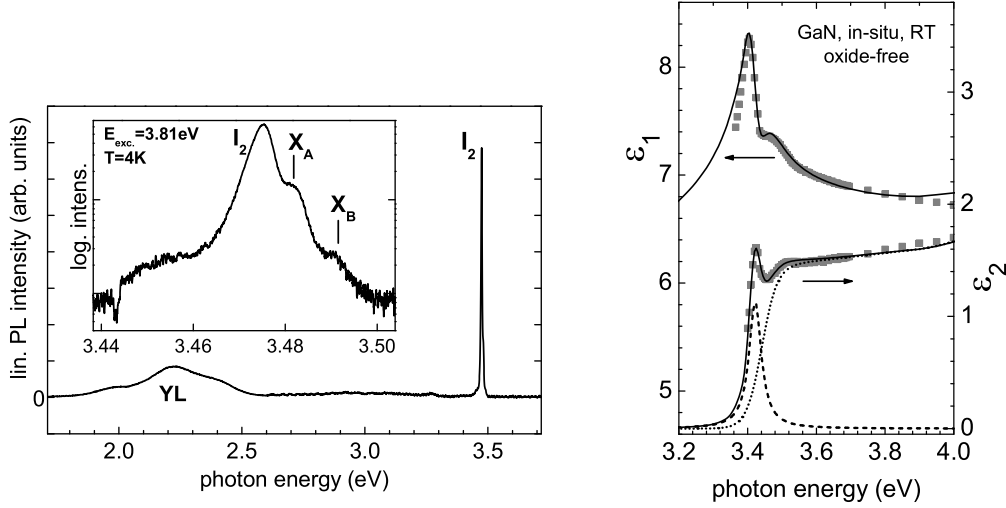
Figure 4.18: Photoluminescence spectra (left) taken at 4 K of a 1.2 μm thick GaN layer on sapphire. Strong donor bound exciton emission I$_2$ dominates the spectrum and free excitons X$_A$ an X$_B$ are observed on the high energy side. The ellipsometry spectra (right) reveal similar features (dashed line) but located approx. 25 meV *below* the band edge (dotted line) already at room temperature. Squares are measured data points.

oscillations.

Assuming that the absorbance edge is located between 3.44 and 3.45 eV at room temperature (dotted line) this oscillator energy is 25 meV below the band edge. In the limited resolution and accuracy of the monochromator adjustment this is in good agreement with the measured 3.475 eV for the donor bound emission line at low temperature. This difference of 25 meV is much larger than the excitonic binding energies and therefore it must be related rather to a defect related transition in the nitride layer than to the bound excitons observed in PL. This is supported by the determined FWHM of 45 meV which is much larger than the room temperature lifetime broadening of a bound exciton or the presence of the X$_A$ or X$_B$ exciton ground states [140]. Indeed there were several defect-related emission lines observed below the band edge which are attributed mostly to GaN dislocations [141] in similar energetic distance to the band edge. The origin of this structure might be found in the relatively high defect density of GaN layer of such thickness. With an increase in thickness and significant reduction in defect density due to layer coalescence this structure is supposed to vanish. So additionally ellipsometry gives the possibility to observe near-gap defects which are not covered by the Fabry-Perot oscillations and thereby gives an estimate for the layer quality.

Finally another indicator for the layer quality is given by the AFM image in Figure 4.19. 2D step flow growth can be observed since the measured terrace height of

0.5 nm is in the range of the lattice constant. On the $5 \times 5\,\mu\text{m}^2$ scan area no significant defects are observed.
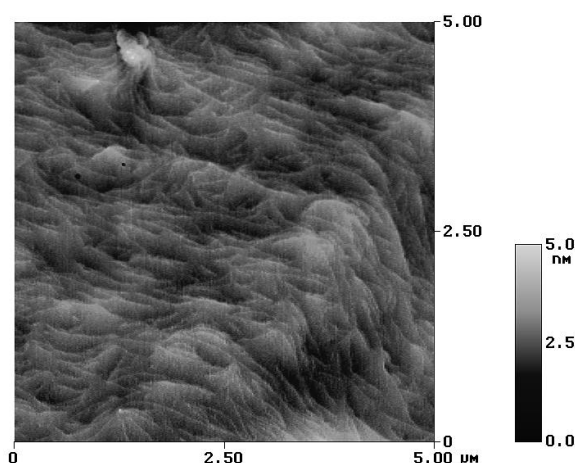

Figure 4.19: $5 \times 5\,\mu\text{m}^2$ AFM image of an $\approx 1.2\,\mu\text{m}$ thick GaN epilayer grown on optimized NL. The overall height scale is 5 nm showing that the steps observed are in the order of magnitude of the lattice constant. No significant defects are observed.

4.5 Growth of GaN epitaxial layer using tertiarybutyl-hydrazine

The standard growth process is performed with ammonia at a V/III ratio of around 2.000 or several sl/min of ammonia. This stimulates the search for alternative precursors with lower decomposition temperature so that a lower V/III ratio can be used with a decrease in precursor consumption. Several potential compounds like hydrazine and its derivatives, e. g. dimethyl- and tertiarybutylhydrazine, were proposed as a substitute for ammonia. Pure hydrazine, which was formerly used as rocket fuel, tends to self-decomposition with high danger of explosion. The more stable compounds with methyl- and tertiarybutyl ligands have much lower vapor pressures of several mbar at room temperature and furthermore they are stable compounds. The (non-symmetric) dimethylhydrazine (UDMHy) [39, 142] as well as tertiarabutylhydrazine [142, 143] have already proven their ability for growth of diluted GaAsN compounds with high quality and its use in low temperature GaN growth should be possible, too. The step wise improvement in precursor quality with lowest oxygen and moisture content in the sub-ppm range finally enabled some experiments with UDMHy provided by Mochem company. In the following the results of GaN growth on sapphire using highly purified UDMHy are briefly described according to the standard growth process which was characterized before.

The development of a low-temperature nucleation layer growth with alternative precursor material is not the most necessary part since the nucleation layer growth takes

layer	precursor	T_{growth} °C	t_{growth} min	V/III ratio
NL	ammonia	550	3	2.000
epilayer	UDMHy	1040	60	60

Table 4.1: Growth parameters listed for the GaN sample grown with the alternative nitrogen precursor UDMHy. NL annealing was performed under ammonia stabilization of 20 mmol/min with nitrogen carrier gas.

place during a few minutes and consumes only a few liters of ammonia. So the reliable NL growth and annealing procedure was retained and the nitrogen precursor was changed from ammonia to UDMHy for the one hour GaN epilayer growth only. In the first experiments the epilayer growth temperature was reduced to 600°C. The sample morphology as well as the structural quality were poor and no photoluminescence signal could be detected. Since both, the sample morphology and the crystallinity strongly depend on the adatom mobility during growth the growth temperature was then kept as high as for epilayer growth using ammonia (1040°C). The respective growth parameters for this sample are given in table 4.1 below: With the use of higher growth temperatures greatly improved sample properties are observed. In the XRD measurements the (0002) reflection FWHM decreased down to 1093 " or 0.3 ° which is an acceptable value for a layer with an approximated thickness of 600 nm. The morphology in AFM showed a drastic improvement from formerly randomly oriented crystals for 600°C growth temperature towards a coalescing layer. Still several residual crystals are
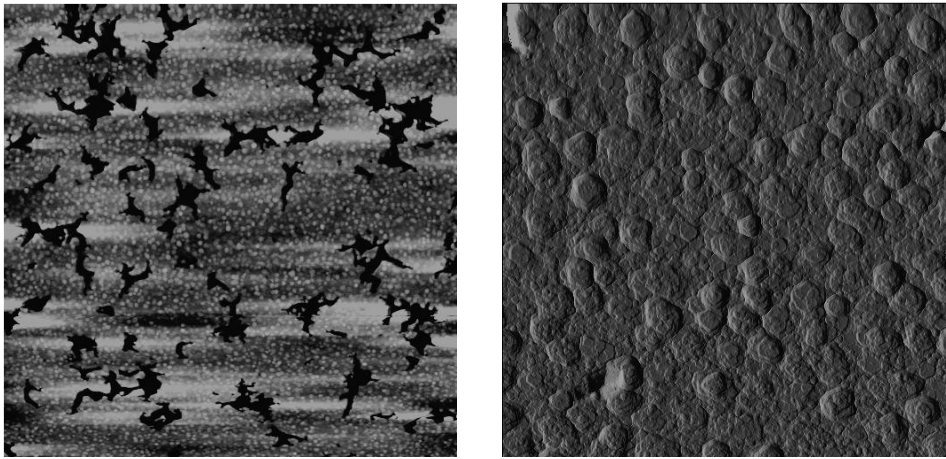

Figure 4.20: Surface morphology of UDMHy grown GaN measured with AFM. The topography image (left, 20x20 μm, 70 nm height scale) shows the onset of layer coalescence at 600 nm layer thickness. The deflection image highlights the remaining roughness on the layer induced by well-oriented crystals of hexagonal shape (right, 3x3 μm, 25 nm height scale).

observed mostly due to parasitic nucleation as shown in Figure 4.20. These residual crystals are of hexagonal shape with a height distribution of 25 nm on the coalesced areas. The improvement in structural quality was accompanied by a drastically improved photoluminescence signal which could be observed now (see Figure 4.21). The
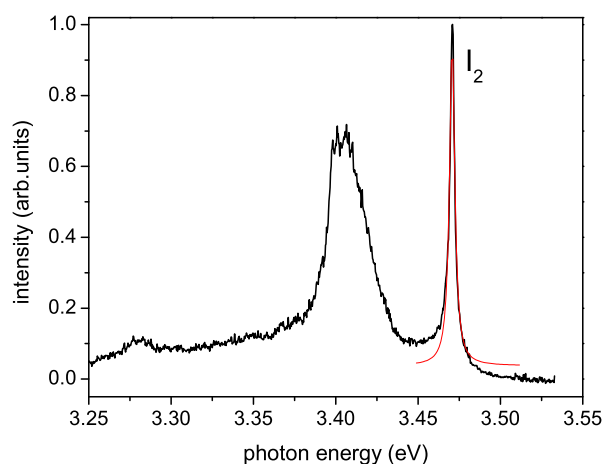

Figure 4.21: Photoluminescence measurement of 600 nm GaN at 6 K grown with UDMHy at 1040°C. The sharp donor bound emission line at 3.47 eV with only 4 meV FWHM is accompanied by a defect induced, broad emission band at 3.4 eV.

measurement at 6 K with an excitation energy of 325 nm from the He-Cd laser showed a strong donor bound emission line at 3.47 eV which is still accompanied by several defect induced emission bands at 3.4 eV and 3.28 eV. The latter one may originate from deep defects which may be attributed to impurities like e. g. carbon. An oxygen-related yellow emission band around 2.3 eV can also be observed (not shown in the graph).

Summary

In situ ellipsometry during GaN MOVPE on sapphire reveals several remarkable peculiarities of the multi-step growth process. During substrate nitridation the threshold temperature and the duration of the substrate nitridation process under ammonia can be measured and precisely controlled, if necessary. The formation of a 4 nm thick crystalline AlN layer is proven from the SE measurements. Furthermore ellipsometry revealed that a low but distinct nitridation of the sapphire substrate already took place through exposure only to hydrogen at high temperatures. This is due to the etching of remaining GaN from earlier epitaxy runs inside the reactor through thermal dissociated hydrogen forming ammonia again. The detailed investigation of nucleation layer growth showed a highly non-linear behavior in the beginning in accordance to previous MBE results. The assumed coalescence of the seeds forming a closed layer is obviously typical for high mismatch epitaxy regardless of the growth method. This seed formation and coalescence varies upon the reactor conditions with drastic influences

on NL growth rate and thickness. For reproducible epitaxy conditions consideration of this influence on the growth rate is a must.

An estimate of the crystalline quality of the NL is given by in situ ellipsometry from which the formation of cubic and hexagonal phases in the NL could be derived. Observing the changes in NL band edge position and defect related broadening Γ, the changes from cubic to hexagonal fractions in the NL depending on the growth rate are shown up according to the findings that best epilayer qualities are achieved only at high NL growth rates. This is clearly correlated with a high cubic proportion in the layer which plays an important role during annealing afterward. Here the phase transformation from cubic to hexagonal material is observed already during temperature ramping, indicating a material transport inside the layer. Therefore enough cubic material has to be provided to allow for a phase transformation towards hexagonal GaN nuclei on the surface. These hexagonal nuclei later act as the seed for epilayer growth which in turn depends on the nuclei density but not necessarily on NL roughness. Thick GaN epilayers reveal high quality when grown on NL prepared according to that improved procedure. Low temperature photoluminescence spectra are dominated by donor bound excitonic emission lines. Corresponding ε_1 and ε_2 spectra of the as-grown non-oxidized layer also show a strong absorption feature directly below the absorption edge which can be attributed to a defect related-transition, allowing for epilayer quality control already during growth.

Chapter 5

Characterization of GaN surfaces in MOVPE and (PA)MBE

Whenever growth processes are studied it is found that surface conditions and surface termination of the material under investigation have to be understood in detail to give a precise description of the whole growth process. This can be easily understood since the epitaxial growth is always an interplay of adhesion, diffusion, adsorption and desorption of reactive species involving atoms of the growing surface [144]. One example of such a complicated process is the influence of the composition of the carrier gas on the bulk properties of GaN and InGaN [145–147]. While the growth of GaN in MOVPE is usually performed under hydrogen carrier gas, for high quality InGaN the use of nitrogen is necessary. Thermodynamic calculations together with experimental results show an increase of the indium content in InGaN leading to the assumption that the surface adatom stoichiometry during growth drastically influences the growth itself. This makes investigations on the growing surfaces even more interesting either to find the driving forces or to reveal the hindering mechanisms for certain growth characteristics.

Several attempts have been made during the last few years to clarify surface structure and surface composition of the III-nitrides during growth. One of the biggest efforts in the case of GaN MOVPE was in the installation of a whole epitaxial growth apparatus onto a synchrotron storage ring for in situ grazing incidence X-ray measurements [148, 149]. From these experiments two different surface reconstructions, a $(1{\times}1)$ and a $\left(\sqrt{3} \times 2\sqrt{3}\right)$R30° were identified to exist on GaN during growth. The corresponding suggested atomic structure models are depicted in Figure 5.1. With increasing ammonia partial pressure a transition from the "standard" $(1{\times}1)$ structure to the $\left(\sqrt{3} \times 2\sqrt{3}\right)$R30° structure can be observed. In this case, $1/3$ of the top atomic layer is removed inducing a missing row structure where four filled atom rows along the $[01]_{surface}$ (corresponds to $[1\bar{1}00]$) direction are followed by two empty ones (com-
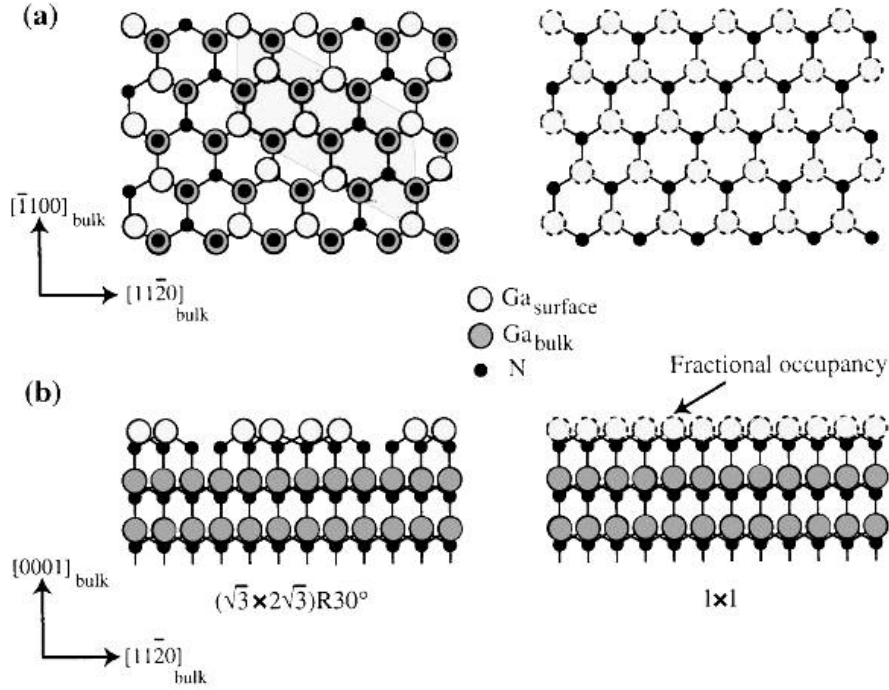
Figure 5.1: The two identified reconstructions for GaN in metal organic vapor phase environment (after Ref. [149]). (a) In-plane structures with a fractional Ga-occupancy on the (1×1) reconstruction. (b) Schematics normal to the surface. While for the (1×1) reconstruction the surface is completely covered with gallium adatoms (right) in the $\left(\sqrt{3} \times 2\sqrt{3}\right)$R30° reconstruction atom rows along the [01]-surface direction are missing.

pare to the left image in figure 5.1). The (1×1) top atomic layer was identified to be a gallium layer, which is consistent with the reduction of gallium coverage with increasing ammonia pressure. But the observed changes for the missing row structure were limited to temperatures as high as 740 °C. Higher temperatures hindered a clear observation of both reconstructions. Furthermore the experimental setup for GIXS during MOVPE requires a synchrotron radiation source and is therefore rather complicated and costly. Thus reproducibility experiments or extension of these results in terms of studies of other nitrides like for example AlN or InN have not been done yet.

Several other groups have used optical methods suitable for in situ monitoring of the nitride surfaces in the gas phase like (shallow-angle) reflectance [150], surface photo absorption [83, 151, 152] or spectral reflectance [82]. Unfortunately these methods allow only for the determination of layer thickness, roughness and, in the case of surface photo absorption, only indirectly for the measurement of surface stoichiometry and bonding sites. They all suffer from the lack of direct access to the atomic structure and only *changes* in stoichiometry can be clearly observed. SPA measurements from

Kobayashi et al. [83] show the tendency of GaN to form a gallium rich surface during growth with increasing temperature. These results will be discussed later in comparison with the ellipsometry results presented here.

Ellipsometry demonstrated the capability to observe and analyze the GaN growth process up to 1050 °C while being surface sensitive down to fractions of a mono layer (see chapter 4). This capability of surface sensitive measurements will be used to find out whether the growing surface consists of nitrogen atoms, of gallium atoms or a mixture of both. Therefore the ellipsometry investigations are first performed during GaN MOVPE and then expanded to the well known, and more examined GaN surfaces during MBE growth. Ellipsometry spectra will be used to compare the surfaces and to transfer the structural results gained in MBE to the MOVPE growth. The existing handicap of GaN polarity (which can be either gallium-face or nitrogen-face as already discussed in more detail in chapter 1 in the (PA)MBE section) makes it essential first to know the surface polarity of the layer under investigation in order to precisely interpret the results.

Evaluating ellipsometry transients

Before a detailed analysis of the GaN MOVPE surfaces can be given, one has to find out whether the preparation of different surface conditions in MOVPE is possible and how it can be controlled and monitored. Furthermore the observation of changes in surface chemistry in the ellipsometry measurements have to quantified before a qualitative analysis can be given. The results of these experiments are shown in the following paragraph 5.1.

In a first effort for preparation of different surface stoichiometries the precursor flux is switched on and off during growth while observing the resulting differences in the ellipsometry response as shown in Figure 5.2. Here it can be seen that the limited temporal resolution of the ellipsometer used (see chapter 2) and some specialities of nitride growth have to be taken into account. First a standard GaN epilayer was grown as described in chapter 4 and then the precursor fluxes were changed while measuring transients of the effective dielectric function at a photon energy of 3.4 eV as follows: after switching off ammonia for 10 s a short pulse (2-3 s) of TMGa is delivered to the surface. For 15 s the reaction is observed and then stabilizing ammonia is switched on again. This procedure is done twice while temperature was varied between 500 °C, 700 °C and 800 °C using hydrogen as the carrier gas. For each temperature, changes within the transients can be observed which are correlated to the precursor switching procedure. For low temperatures (500 °C) these changes are in the range of the noise limit and cannot be resolved. Increase of temperature increases the signal amplitude drastically but unfortunately for 800 °C and higher the surface does not recover to its original state as indicated by the horizontal lines (Figure 5.2). A possible explanation
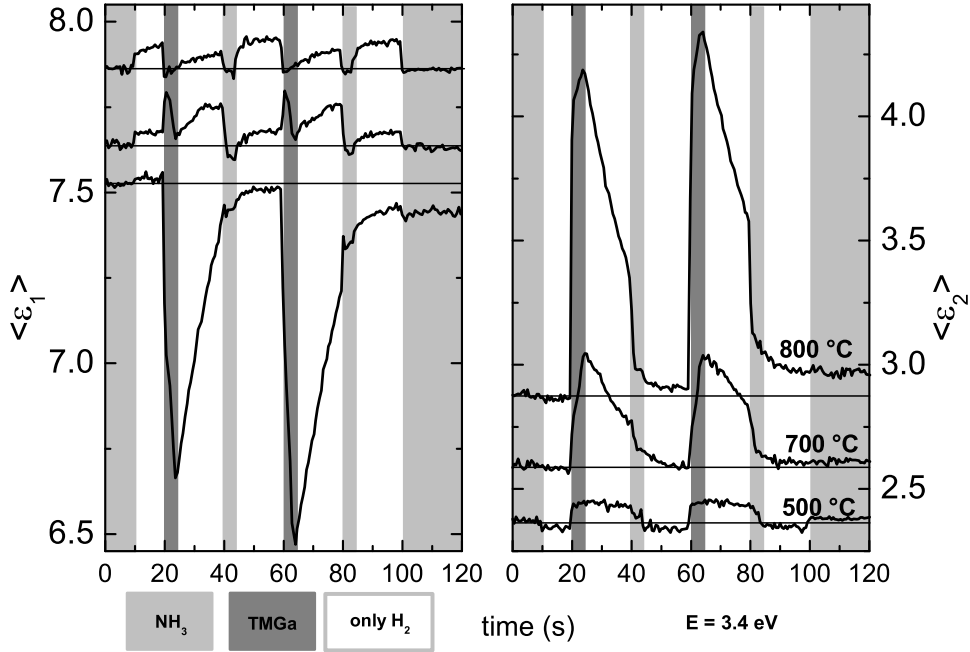
Figure 5.2: Ellipsometry transients of $\langle \varepsilon_1 \rangle$ and $\langle \varepsilon_2 \rangle$ taken during precursor switching at different temperatures under hydrogen carrier gas. After switching off the stabilizing ammonia flow a short pulse of TMGa is delivered to the surface. While at 500 °C the observed changes are close to the noise limit, a drastic increase in $\langle \varepsilon \rangle$ is observed at higher temperatures. Unfortunately irreversible changes on the surface are observed at 800 °C after switching on ammonia again, as the deviation from the horizontal lines indicate.

could be either the formation of gallium droplets strongly influencing the ellipsometric response through mie resonant scattering processes [103] or a surface roughening due to hydrogen etching. Both processes are irreversible under the given conditions. To avoid the problem of roughening either temperatures lower than the real growth temperature of 1050 °C or nitrogen as carrier gas have to be used.

With this knowledge a stable gallium rich surface under controlled flow of TMGa has to be produced. A simple calculation of the amount of gallium atoms offered to the surface allows for estimation of the appropriate time scale and precursor fluxes for the switching process. With the given flux of 22 μmol/min TMGa during the standard growth procedure and assuming total decomposition at 900 °C (which is reasonable [144]) the flux of gallium atoms supplied to the surface is about 5×10^{16}/s. Since one monolayer consists of about 1.14×10^{14} atoms/cm^{-2} [62] this indicates that switching gallium for less than $1/10$ of a second would be long enough to cover the surface com-

pletely with gallium atoms. Here the sample width of the standard 10x10 mm² sapphire substrate as approx. 1/10 of the reactor cross section and the gas flow velocity of approx. 0.8 m/s is taken into consideration. Now reducing the gallium flux to 1/10 of the standard epitaxial flow the time scale for a surface coverage of approx. one monolayer gallium atoms expands into the range of seconds. This is the lowest value possible where a stable and time-constant TMGa gas flow can be assured since it is limited by the dimension of the mass flow and pressure controllers used in the precursor line and therefore has to be accepted. This time should be long enough to observe and analyze the suspected differences related to a possible gallium coverage.

Figure 5.3 now shows two typical transients for two different gallium switching times of 1 and 3 s. When switching on gallium for only one second, a drastic increase
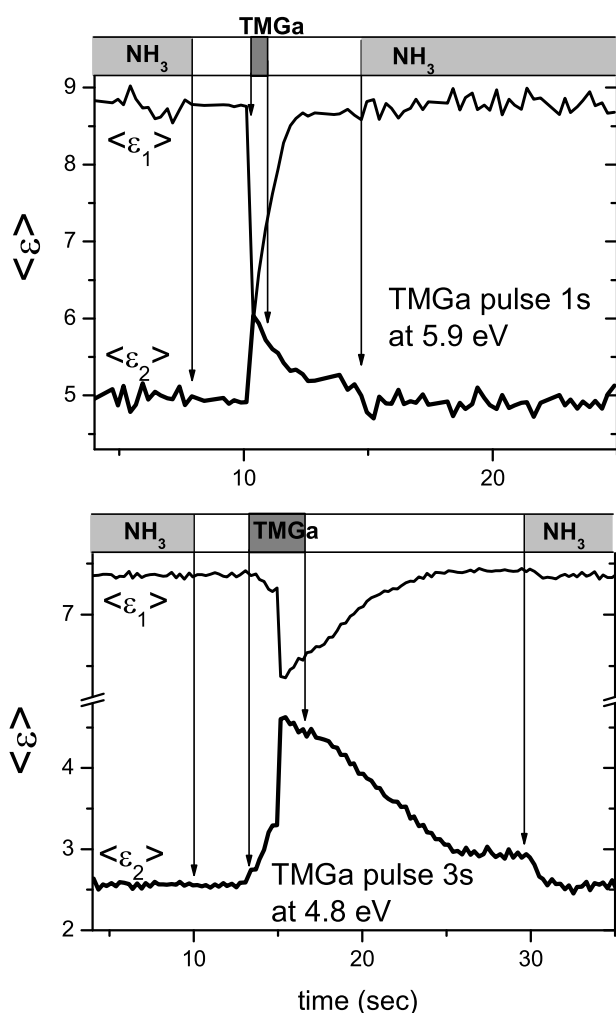
Figure 5.3: $\langle \varepsilon \rangle$ transients for TMGa exposure without ammonia under nitrogen carrier gas at 900 °C for 1 (upper graph) and 3 s (lower graph). For 1 s a single maximum is the only response while in the 3 s transient more structures are resolved. For 3 s gallium exposure the signal decreases during steady gallium flow. No plateau occurs for both transients.

in $\langle\varepsilon_2\rangle$ and decrease in $\langle\varepsilon_1\rangle$ is still observed at the same time, even with the reduced TMGa flow. After the gallium switching cycle without any precursor flow - except for the nitrogen carrier gas - the signal already decays instead of showing an expected plateau under steady conditions (Figure 5.3, bottom graph). The origin of this behavior may be gallium desorption which is expected to begin at these temperatures (typical operating temperatures for gallium Knudsen cells in MBE are between 850 and 950 °C). Furthermore the amplitude of the signal maximum cannot be determined precisely due to the limited temporal resolution of the ellipsometer of approx. 0.3 s. Therefore a second set of transients is taken with a gallium switching time of three seconds for better evaluation (Figure 5.3, top graph). The longer gallium flow shows a similar lineshape but in more detail. Immediately after switching on the TMGa flux an increase in $\langle\varepsilon_2\rangle$ is observed. A first saturation after approximately 1 s can be seen and then the signal increases further. The highest value has been reached after approx. 2 s and the signal decays while the TMGa is still on. The decay slope changes slightly after switching off the TMGa. The surface recovers to its original state when switching ammonia on again.

Obviously the gallium switching process leads to two different surface states, one directly after switching on the gallium source and the second state much later, as if the gallium atoms have to arrange on the surface. As a result of these experiments several restrictions have to be made:

The TMGa flow has to be reduced to the lowest possible value, in our case to $1/10$ (eqiv. $2.2\,\mu$mol/min) of the standard growth flux.

Hydrogen as a carrier gas has to be avoided for long term transient measurements at temperatures above 800 °C. Since the amount of gallium present in the gas phase determines the growth rate and thereby the growth process (as shown in chapter 4) a lack of gallium under the presence of atomic hydrogen and reactive NH_2* produced through thermal dissociation of ammonia etches the surface [152, 153]. As a consequence monitoring of the optical response from GaN surfaces using different precursors cannot be made at but only close to epitaxial conditions.

Finally the highest temperature possible which can be chosen is 900 °C using nitrogen as the carrier gas. Nitrogen reduces surface etching tremendously and at temperatures up to 900 °C no risk of uncontrolled surface deterioration (roughening) exists. Finally this temperature coincides fairly well with the epitaxy temperature of 850 °C used in the MBE experiments described later and thus enables easy comparison of the results obtained with different growth techniques.

5.1 Preparation of different GaN-surface stoichiometries in MOVPE

Using a gallium deposition time of 5 s the two different stages of gallium deposition on the GaN surface can be clearly distinguished. To achieve a spectral response transients are recorded at different photon energies in distances of 0.2 eV. All transients are evaluated according to the one depicted in Figure 5.4. It should be noted that for simplification only values of $\langle \varepsilon_2 \rangle$ are discussed because the different stages of the gallium precursor switching sequence can be more easily distinguished in $\langle \varepsilon_2 \rangle$ than in $\langle \varepsilon_1 \rangle$. Whenever calculations are mentioned they are of course made for both values, $\langle \varepsilon_2 \rangle$ and $\langle \varepsilon_1 \rangle$.

The value of $\langle \varepsilon_2 \rangle$ in Figure 5.4 increases rapidly when the TMGa is turned on, reproducibly displaying a small shoulder in the first second after the turn-on (left square in figure 5.4) and then continuing to increase rapidly for another 1-2 seconds. Since the duration necessary for a mono layer coverage with gallium was approximated to one second the initial increase in $\langle \varepsilon_2 \rangle$ up to the above-mentioned shoulder is probably due to the formation of a gallium rich surface. To determine the value of $\langle \varepsilon \rangle$ for the first process an extended Langmuir fit function for the mathematical description of the adsorption of gases on surfaces is used. This way the expected value of $\langle \varepsilon_2 \rangle$ for one monolayer of gallium can be determined (dotted line in figure 5.4). The increase of the signal after the "shoulder" to a maximum value is then followed by a sudden exponential decrease while the gallium flux is still on. This behavior is attributed either to additional gallium deposited on the surface in the form of unstable layers and then slowly forming droplets, which could explaining the decay. Otherwise it could possibly be ascribed to the presence of hydrogen and the formation of hydrogen-induced reconstructions [154]. The latter could also be supported by the fact, that the described behavior occurs more distinctly but on a larger time scale when using hydrogen as the carrier gas. Finally this decay can be approximated using a simple power law expression as shown by the dashed line in Figure 5.4, leading to a slightly higher value of $\langle \varepsilon_2 \rangle$ than in the beginning of the gallium switching cycle. Then a stable gallium layer would be formed, represented by the $\langle \varepsilon_2 \rangle$ value the curve fit approximates. For this transient, taken at a photon energy of 4.8 eV, an average $\delta \langle \varepsilon_2 \rangle$ can be determined resulting from the two stages of gallium adsorption located between 0.8 and 1.2 units. After the gallium flux is switched off (right circle in figure 5.4), the slope of the decay curve changes drastically, clearly indicating some desorption process and precluding the involvement of adsorbates like hydrogen. Finally, when ammonia is switched on again, the surface recovers to its original state as indicated by $\langle \varepsilon_1 \rangle$ and $\langle \varepsilon_2 \rangle$ being identical to their starting values.

The spectral information from all transients in energy distances of 0.2 eV starting at 3 eV is shown in Figure 5.5. For all transients similar differences between the be-
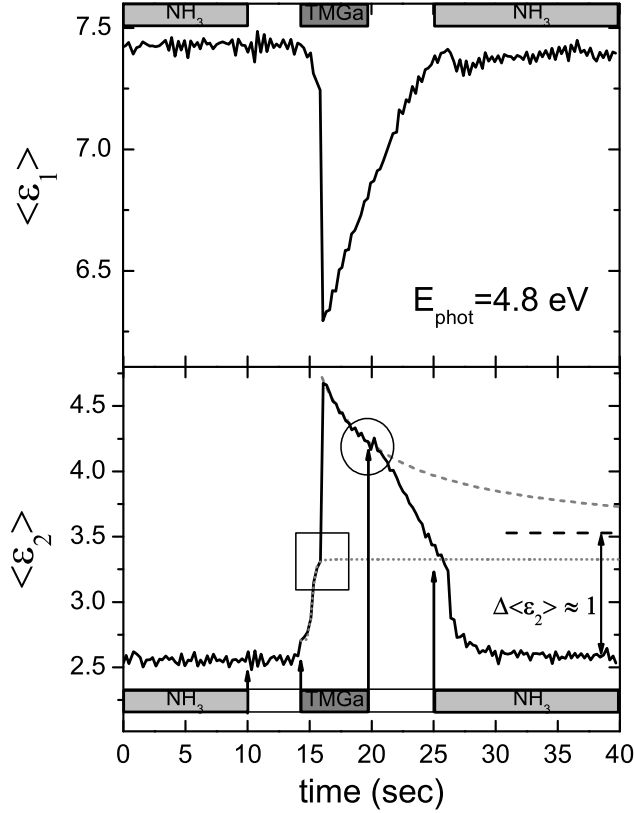
Figure 5.4: $\langle \varepsilon \rangle$ transients taken during switching on TMGa for 5 s at E=4.8 eV. Before switching on gallium ammonia was switched off. The transient clearly reveals two different stages of the gallium rich surface. One directly after switching on gallium (indicated by the square), the other at the end of the gallium cycle (circle). The dotted lines show exponential fits to obtain the respective $\langle \varepsilon_2 \rangle$ value for the stable gallium rich surface.

ginning (squares) and the end (circles) of gallium switching are found. Preparation of the GaN surface with a short gallium flux leads to a reproducible increase of the amplitude of $\langle \varepsilon_2 \rangle$. The low energy range of the effective dielectric function dominated by narrow Fabry-Perot (FP) interferences could not be considered due to several reasons. For a precise description of the FP-range between 1.6 eV and 3 eV, an energy interval of 0.05 eV or less would be necessary, which would need more than 50 transients. Due to a small temperature shift possibly occurring or a change in thickness (the switching cycles correspond in a way to atomic layer epitaxy) non negligible changes in the interference structures can be found. This makes it nearly impossible to attain reproducible values during the time necessary and therefore we omitted this region, concentrating only on the high energy region between the E_0 and E_1 transitions (compare chapter 3).

To evaluate these drastic changes in $\langle \varepsilon_2 \rangle$ due to gallium switching, first the formation of some overlayer roughness with a smoothing afterwards will be ruled out. Comparing the results to a GaN layer with a rough layer on top (see also chapter 3, figure 3.6) this would lead to a significant increase in $\langle \varepsilon_2 \rangle$ above the E_0 gap position, accompanied by a monotonous decrease in $\langle \varepsilon_1 \rangle$ and $\langle \varepsilon_2 \rangle$ around the E_1 transition. Tak-
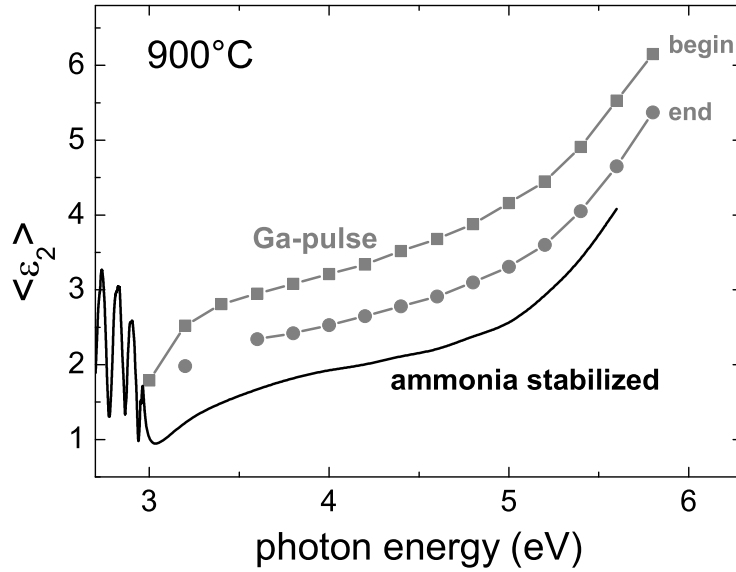
Figure 5.5: Spectral response of $\langle \varepsilon_2 \rangle$ during gallium switching gained through evaluation of several transients taken in 0.2 eV intervals. While the curve indicated by circles shows the $\langle \varepsilon_2 \rangle$ values for the immediate change after the first second, the square curve stands for the value of $\langle \varepsilon_2 \rangle$ after exponentially approximating a stable plateau under constant gallium flux.

ing the maximum peak values after gallium switching (square curve in Figure 5.5) as a first approximation, the observed changes are clearly different from what is expected for a simple roughness formation as shown in Figure 5.6 (gray curves). To achieve similar changes in $\langle \varepsilon_2 \rangle$ values a huge roughness of 8 nm has to be assumed (dotted lines in figure 5.6). But then the gallium-related signal shows no decrease in $\langle \varepsilon_2 \rangle$ when approaching the E_1 transition located at approximately 6.5 eV at 900 °C sample temperature. Furthermore the observed crossing of the $\langle \varepsilon_1 \rangle$ signals around 4 eV for the gallium enriched surface cannot be reproduced by a simple formation of a roughness. Obviously the signal which has formed after the gallium switching must be correlated with the properties of a gallium layer. For calculation of a gallium overlayer influence on the GaN $\langle \varepsilon \rangle$ spectrum the gallium dielectric function has to be known in the energy range of the measurements. Unfortunately, in literature the listed dielectric properties of most metals [98] have a lower boundary of 400 nm or correspondingly 3 eV and only few data points available give low accuracy as depicted in Figure 5.7. This data set does not allow for reliable results for calculation of gallium influences on the GaN surface. Thus the gallium dielectric properties were determined in the energy range

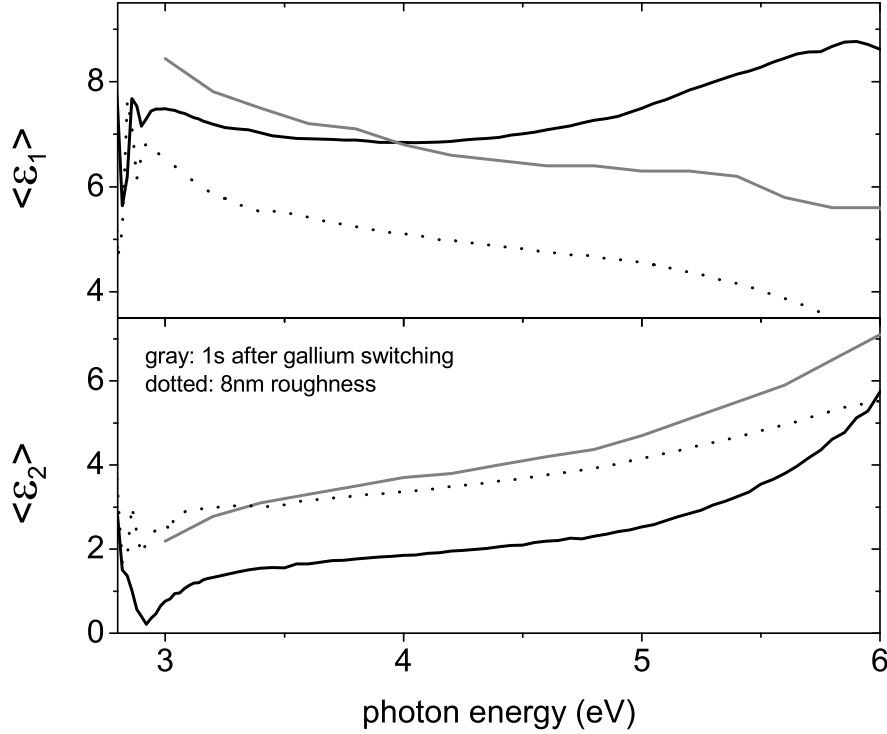gray: 1s after gallium switching
dotted: 8nm roughness

Figure 5.6: $\langle \varepsilon_1 \rangle$ and $\langle \varepsilon_2 \rangle$ spectra obtained taking the respective values for the largest changes after gallium switching (gray lines). The dotted lines show the expected behavior in the case that a very thick (8 nm) roughness has formed on the GaN layer. Neither do the roughness spectra show the occurring crossing in $\langle \varepsilon_1 \rangle$, nor do the gallium switching related spectra show the roughness typical decrease when approaching the E_1 transition.

from 1.6 eV up to 6 eV (205 nm). A thin film of pure (99.999 %) gallium was prepared between two microscopic slides and heated to 50 °C in the MOVPE reactor to form a smooth, homogeneous layer. After cooling down to room temperature (gallium melts at 28.9 °C) the upper slide was removed under pure nitrogen atmosphere inside the glove box of the epitaxy machine and quickly reloaded into the reactor chamber. The spectra achieved are shown in figure 5.7, solid lines. Significantly larger amplitudes in $\langle \varepsilon_1 \rangle$ and $\langle \varepsilon_2 \rangle$ than has been reported previously were observed around 2 eV (dotted lines in figure 5.7, after [98]), while the overall line shape is similar. This is attributed to the accurate preparation procedure, leading to smooth, non-oxidized and crystalline gallium. In Figure 5.8 the results of a calculation of a thin gallium overlayer on GaN using the self-determined gallium dielectric function is compared to the gallium switching results. A significant improvement between calculation (dashed line) and the spectrum under gallium flux (gray line) is found. Assuming a 0.7 nm thin gallium layer on GaN
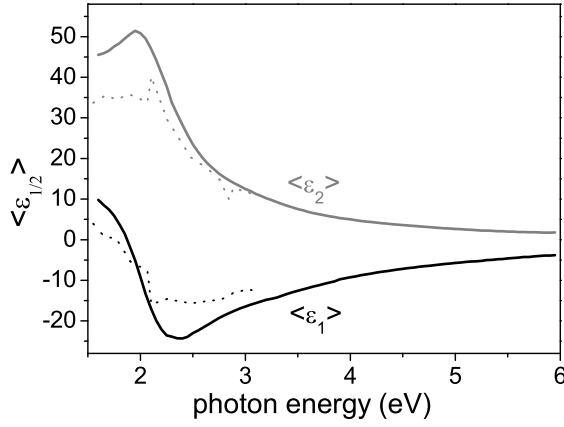
Figure 5.7: Effective dielectric function of pure gallium measured by oxide free preparation in the MOVPE reactor between 1.6 and 6 eV (solid lines). The data published before [98] are shown for comparison (dotted lines). The significantly higher amplitudes of the gallium dielectric function measured in situ indicates that the accurate preparation led to an oxide free gallium layer.

the shift in $\langle \varepsilon_2 \rangle$ can be described well and simultaneously the crossing in $\langle \varepsilon_1 \rangle$ at 4 eV is achieved. As a result of these experiments a clear trend can be observed: while GaN shows no significant differences with or without ammonia stabilization (as one can see in the beginning of each transient, e. g. in Figure 5.4), the switching of gallium leads to changes in the effective dielectric function which can only be attributed to the presence of a gallium overlayer on GaN.

Unfortunately SE still does not give a detailed insight into the real, atomic structure and composition of the surface. Therefore surface analysis methods such as AES and LEED have to be carried out. However, these techniques require an UHV environment. In order to solve this problem GaN surfaces are prepared with (PA)MBE in an UHV chamber connected to an UHV analysis chamber. In situ ellipsometry then is used to compare the surfaces produced in (PA)MBE environment to those under MOVPE conditions.
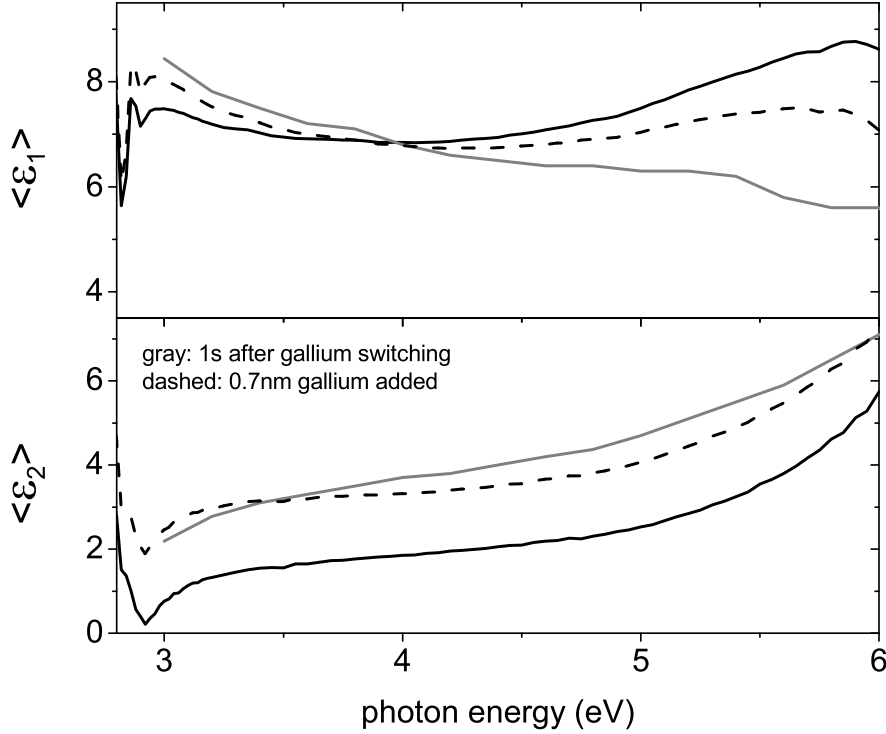
Figure 5.8: $\langle \varepsilon_1 \rangle$ and $\langle \varepsilon_2 \rangle$ spectra obtained taking the respective values for the largest changes after gallium switching (gray lines). Assuming a 0.7 nm gallium overlayer (approx. 2 ML gallium), a better agreement than for the formation of a rough overlayer (figure 5.6) is achieved. In the high energy range still a non negligible difference occurs. Solid line: GaN under nitrogen-rich conditions.

5.2 Preparation of different GaN-surface stoichiometries in (PA)MBE

For an exact identification of the spectral features which seem to be correlated to the gallium surface chemistry in MOVPE, analogous experiments for GaN have been performed in (PA)MBE. The use of ellipsometry as a monitor to compare the different surfaces in MOVPE and (PA)MBE is motivated by similar experiments using RAS on cubic materials. There RAS spectra have been successfully correlated to MBE [77] and CBE [155] prepared surfaces to gain insight into MOVPE growth. This invites a comparison of the GaN MOVPE results with analogous (PA)MBE experiments. In (PA)MBE, access to electron-based characterization tools like Auger Electron Spectroscopy (AES) and Low Energy Electron Diffraction (LEED) is possible. This allows clear determination of surface stoichiometry and symmetry. Since the different surface

reconstructions and their respective surface coverages are well known for MBE (as described before in chapter 1), this should help to identify the ellipsometry measurements made in MOVPE. Finally, combining the results of all experiments, an interpretation of the surface stoichiometry in GaN MOVPE growth is possible.

Experimental procedure

The samples used were similar to those from the MOVPE experiments: thick 1 to 2 μm MOVPE-grown GaN with GaN low temperature nucleation layer on [0001] sapphire substrates. The templates were transferred into the vacuum chamber after MOVPE growth and deoxidized prior to growth. The chamber was equipped with a standard Knudsen cell for gallium evaporation and a nitrogen plasma gun from Oxford instruments operating at 13.56 MHz at a maximum power of 250 W. Both sources were equipped with external shutters. Typical operating nitrogen flux was 5 sccm/min at a growth pressure of 5×10^{-5} mbar. After a brief heating to 600 °C under nitrogen plasma flux the templates were considered to be fully deoxidized and thus ready for rise to epitaxy temperature. This procedure prior to growth was the best compromise between overlayer removal (oxide film, water and carbon contaminations) and possible roughening of the surface at higher temperatures, since prolonged annealing (>10 min) at temperatures above 500°C is reported to lead to non reversible roughening [91]. Usually the GaN oxide removal is reported to be complete at higher temperatures of 800 °C [156] in the presence of ammonia but without obtaining smooth surfaces. After deoxidation the temperature was quickly raised to 810 °C epitaxy temperature while the gallium source shutter was opened at 650°C. These temperatures agree well with the experimental procedure described in [59, 61, 62], from which detailed characterization of GaN surfaces in UHV is known. The whole following surface preparation procedure is monitored with ellipsometric transients at a photon energy of 4.8 eV as shown in figure 5.9. In this transient one clearly sees that ellipsometry highlights every change in surface chemistry, morphology and sample temperature. Heating from room temperature to 600 °C shows only slight changes due to the removal of surface contaminations like moisture and carbon compounds. Having reached 600 °C, the plasma source is opened with no significant influence to the transient. After a few minutes the sample temperature is raised to 810 °C while the gallium source is simultaneously opened with an initial increase of temperature at around 650 °C. This is accompanied by a drastic increase in $\cos \Delta$. After a slight overshoot in temperature indicated by the overshoot in the $\cos \Delta$ transient, ellipsometric spectra are taken to ensure that the sample surface is not destroyed by the applied heating procedure. Then the sample temperature is slowly raised to 850 °C. The gallium flux is changed next between the maximum (according to 950 °C gallium evaporation cell temperature) and the minimum flux where the surface can still be stabilized and no roughening occurs. If roughening would occur this should
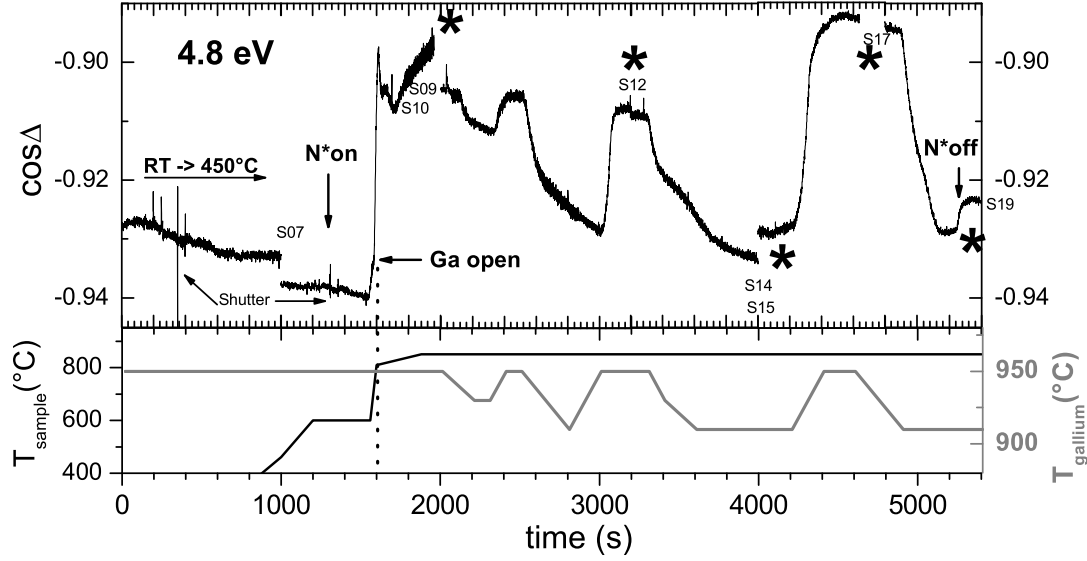
Figure 5.9: Ellipsometric cosΔ transient during GaN (PA)MBE surface preparation at 850°C with highest and lowest gallium flux possible (upper graph). High gallium cell temperature (equivalent to high gallium flow) reproducibly leads to high cosΔ values and vice versa. Ellipsometric spectra (denoted S07-S17 in the upper graph) are taken in between. The applied sample and gallium cell temperatures are shown below.

lead to a drastic increase in cosΔ at low gallium cell temperature. On the contrary, whenever the gallium temperature is lowered, the monitored cosΔ value decreases, clearly showing that no surface roughening occurs. When the transient indicates more or less stable conditions of the surface, several ellipsometric spectra of the sample are taken under either high or low gallium flow (denoted by asterisks). The relative gallium flux ratio between 950 °C and 910 °C is determined to be 3:1 from the absolute gallium vapor pressure [157, 158]. Below 900 °C no gallium flux onto the surface was detectable. Finally in this run the nitrogen plasma is shut off under low gallium flux and the sample is cooled to room temperature simultaneously.

5.3   The GaN dielectric function in (PA)MBE

Two of the spectra taken during surface preparation at high temperature are shown in figure 5.10. All spectra measured during preparation show distinct gallium flux related features above the band gap region (which is located around 3 eV at 850 °C), and they all can be clearly divided into two groups. All spectra taken during high gallium flux preparation (gray line) are shifted by approximately 1 unit in $\langle \varepsilon_2 \rangle$ with respect to those
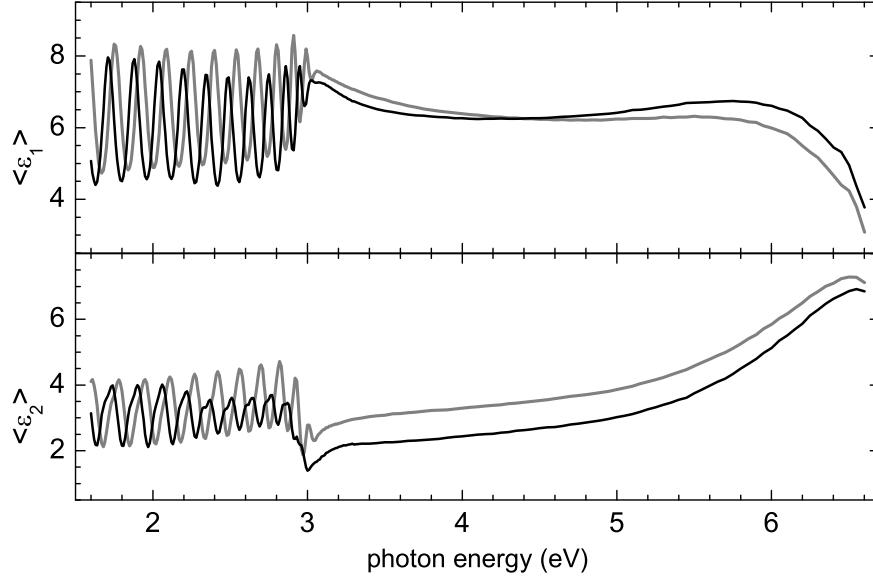
Figure 5.10: Pseudo-dielectric function of the gallium-rich and gallium-poor surfaces during GaN (PA)MBE at 850 °C. Exemplarily two spectra are shown out of all those which can be clearly divided into two groups. The gallium-rich spectra (gray) are shifted in $\langle \varepsilon_2 \rangle$ to higher values while in $\langle \varepsilon_1 \rangle$ a crossing of the gallium-rich and gallium-poor ones (black) at around 4.5 eV can be observed.

taken during low gallium flux (black line). For $\langle \varepsilon_1 \rangle$ a similar arrangement into two groups can be found, especially in the spectral range approaching the E_1 transition. Most interesting is the crossing of the spectra in the range of 4.4 eV which can be observed in MOVPE under TMGa pulses, too.

5.3.1   Preparation of gallium rich surfaces

The lack of exact high-temperature dielectric data of gallium makes exact interpretation of the in situ results very difficult. Thus two different possibilities for interpretation of the observed ellipsometric spectra exist: either a comparative calculation between the two different high temperature states (gallium rich vs. nitrogen rich) is performed. Then a model function must be used which is not based on the gallium dielectric function but somehow correlated to the expected metallic overlayer behavior. Otherwise the layer is "frozen" preserving the different surface states while cooling the sample to room temperature using the gallium dielectric function to explain possible differences. In the first case one benefits from the prolonged stabilization of both surfaces under the respective conditions, which is already indicated by the two spectra in Figure 5.10. It can be reproducibly switched between both solely depending on the gallium flux. Therefore two spectra are taken directly before and after a fast increase from low to high gal-

lium cell temperature to ensure a negligible difference in layer thickness. Thus similar Fabry-Perot layer thickness interferences appear in both spectra of Figure 5.11. These interference regions can then be used for a precise calculation, too. For simulation of
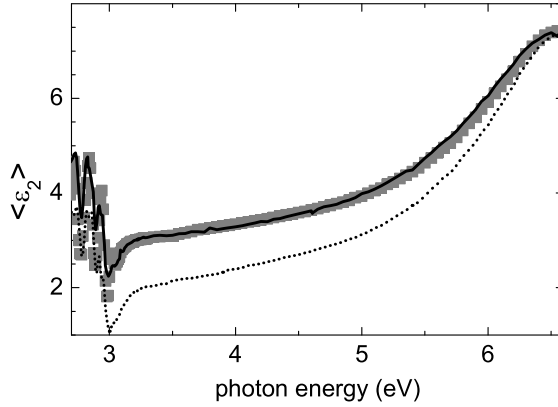

Figure 5.11: $\langle \varepsilon_2 \rangle$ spectra of the nitrogen- (dotted line) and gallium-rich (gray squares) surfaces during (PA)MBE growth. A Drude like metallic layer of 0.4 nm thickness with an electron density of $2 \times 10^{22}\,\mathrm{cm}^{-1}$ is used to describe the change towards the gallium-rich state (solid line).

the occurring differences at the high temperature of 850 °C a metallic overlayer with a Drude-like behavior [159] is used. This layer is mainly characterized by free electrons with a density of $2 \times 10^{22}\,\mathrm{cm}^{-1}$, being typical for metals like gallium. With these assumptions a thin layer of 0.4 nm added to the "nitrogen-rich" spectrum (dotted line) is enough to find a perfect agreement with the "gallium-rich" spectrum (gray squares in Figure 5.11) at high temperatures.

This enables a detailed characterization of the surfaces using AES and LEED after cooling the sample to room temperature. To ensure that the gallium rich state is preserved the preparation procedure was as follows (referring to Figure 5.9): during high gallium cell flux (e. g. S12 in fig. 5.9), the sample heating is switched off and during the steep decrease in sample temperature the gallium evaporation cell is closed immediately after the nitrogen plasma cell at a sample temperature of ≈ 800 °C. During this procedure an ellipsometry transient is taken at a photon energy at 5 eV to assure that no structural changes result from shutting off the cells. Only a temperature-dependent exponential decrease of the $\langle \varepsilon \rangle$ values can be observed due to the energy shift of the inter-band critical points. Heaving reached room temperature, an ellipsometry spectrum is measured and the sample is transferred quickly into the analysis chamber after a base pressure better than $1 \times 10^{-8}\,\mathrm{mbar}$ is reached in the growth chamber. Then LEED and AES measurements are performed as shown in Figure 5.12 at a pressure below $5 \times 10^{-10}\,\mathrm{mbar}$. As already discussed in chapter 1 the metallic overlayer on [0001] GaN during (PA)MBE growth should result in a characteristic super structure in the LEED pattern. In the respective LEED images the (1×1) gallium bilayer structure in form of a "1+1/6" super structure in the $(\sqrt{3} \times \sqrt{3})$-R30° surface pattern can be found.
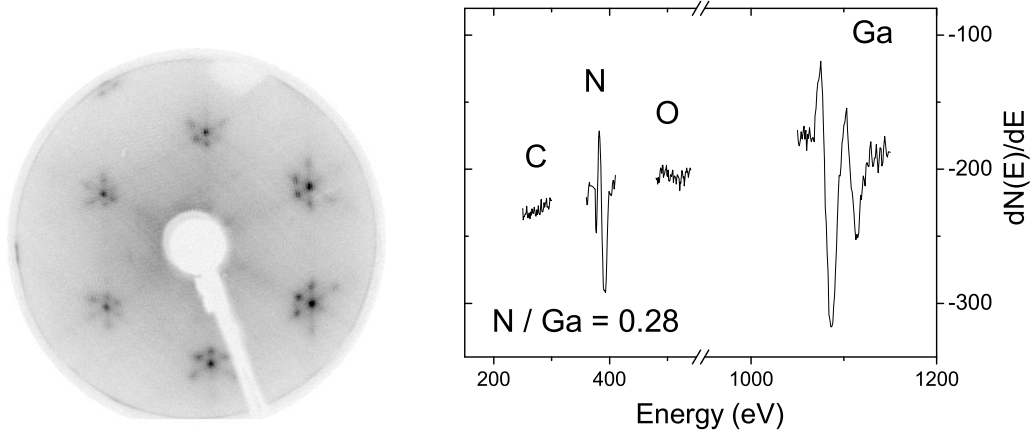
Figure 5.12: Ga-overlayer LEED pattern (63 eV, RT) of as-grown GaN(0001) taken after PAMBE preparation under high gallium flux (950 °C gallium cell temperature). The (1×1) gallium bilayer structure can be seen additionally to the $\sqrt{3} \times \sqrt{3}$-R30° surface pattern while AES shows a relative nitrogen/gallium ratio of only 0.28. Under the presence of the gallium bilayer no further contaminations are found and the surface is smooth (comp. figure 5.13)

These surfaces show a nitrogen/gallium ratio in AES of only 0.28 which indicates the highly gallium-saturated surface termination. No evidence for carbon or oxygen contamination of the surface is found. Finally, a smooth GaN surface with mono atomic terraces is measured by ex situ AFM investigations after this preparation cycle (Figure 5.13). The only defects indicated by the black spots in the AFM image show the center of screw dislocations, which are the main defect type in GaN heteroepitaxy on sapphire. Optical microscopy investigations reveal several isolated gallium droplets at the edges of the sample, indicating excess gallium.
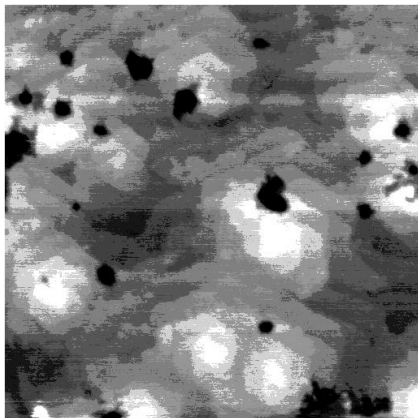
Figure 5.13: $1\mu m^2$ AFM image of as-grown GaN (0001) measured directly after PAMBE preparation with high gallium cell temperature. Smooth surfaces with atomic steps are found (approx. 2 nm height scale black/white). Black spots are related to the center of screw dislocations.

For analysis of the ellipsometry spectra measured after preparation of the gallium rich surface the gallium dielectric function - as was determined before - can be used as shown in Figure 5.14. Furthermore the ellipsometry results can be clearly correlated to the structural investigations. The spectra under these gallium rich conditions at room
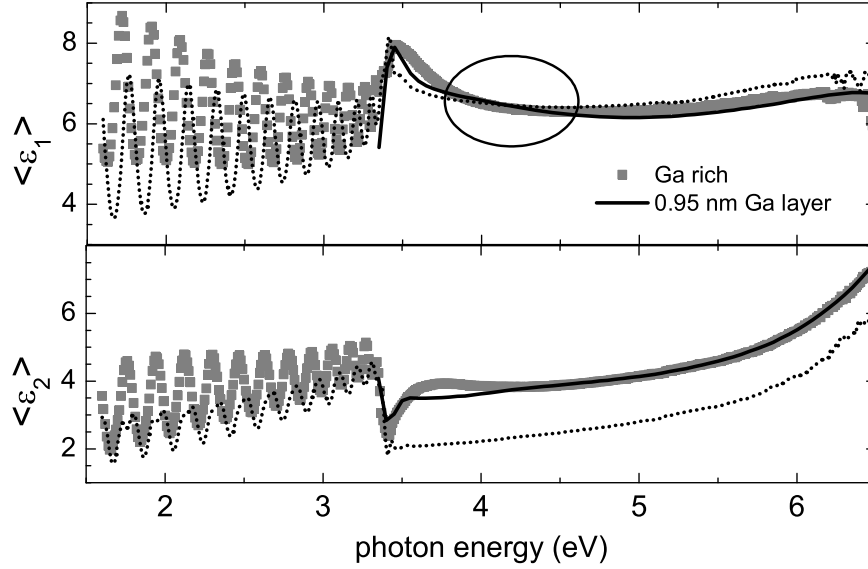

Figure 5.14: $\langle \varepsilon_1 \rangle$ and $\langle \varepsilon_2 \rangle$ spectra of the gallium rich surface (gray squares) vs. "as transferred" surface (dotted line) in MBE at room temperature. A clear shift in the $\langle \varepsilon_2 \rangle$ spectrum of two units above the band edge is observed as well as the crossing of $\langle \varepsilon_1 \rangle$ around 4.3 eV (circle). By adding a 0.95 nm thick gallium adlayer, these two features (shift and crossing) can be simulated (straight line) with a reasonable agreement using the gallium pseudo-dielectric function.

temperature (gray squares) reveal a noticeable difference to the spectrum of the sample before preparation (dotted lines). The $\langle \varepsilon_2 \rangle$ of the gallium-rich spectrum is shifted to higher amplitudes in the range above the band edge by two units. The $\langle \varepsilon_1 \rangle$ spectrum shows the already observed crossing in the range around 4 eV. Since these two spectra are taken at room temperature, the difference between both has been calculated using the self determined gallium dielectric function. A similar line shape above the band edge position can be achieved assuming a 0.95 nm "thick" gallium adlayer which is shown by the solid line in Figure 5.14. Again, we cannot make a reliable statement below the band edge region because the Fabry-Perot interference structures of the sample before and after preparation are strongly different due to the different layer thicknesses. This adlayer is twice as thick as the one observed during growth shown in Figure 5.11. From a phenomenological point of view these different results can be easily explained comparing the two sets of spectra: while at growth temperature the gallium rich spectrum is shifted for approximately one unit, this shift is twice as large for the room temperature spectra. Furthermore, the highly contracted $1 + 1/12$ super

structure in the LEED images cannot be observed like in [59], but only a $1 + 1/6$ super structure appears. Together with the observed gallium droplets on the edge of the sample we assume the formation of a highly saturated gallium surface during cooling to room temperature. This explains both, the different results in the calculations and the different line shapes of the dielectric function during and after growth.

5.3.2 Preparation of nitrogen rich surfaces

Before the results from the gallium rich (PA)MBE surfaces are correlated with the ellipsometry spectra gained during MOVPE growth, the nitrogen rich surfaces must be characterized for completeness. Therefore a similar procedure as before is chosen, except that the nitrogen source is shut off *after* reducing the gallium flux to the lowest possible value as indicated by the end of the transient in Figure 5.9. Afterwards an ellipsometry spectrum is measured at room temperature and the sample is transferred into the analysis chamber to perform AES and LEED. The respective results are shown in Figure 5.15. While the nitrogen vs. gallium ratio is increased to 0.84, which is nearly three times larger than for the gallium rich surface, the LEED image shows no indication of a surface layer super structure, but only the $(\sqrt{3} \times \sqrt{3})$-R30° surface reconstruction. In the AFM image no 2-dimensional growth can be observed any longer,
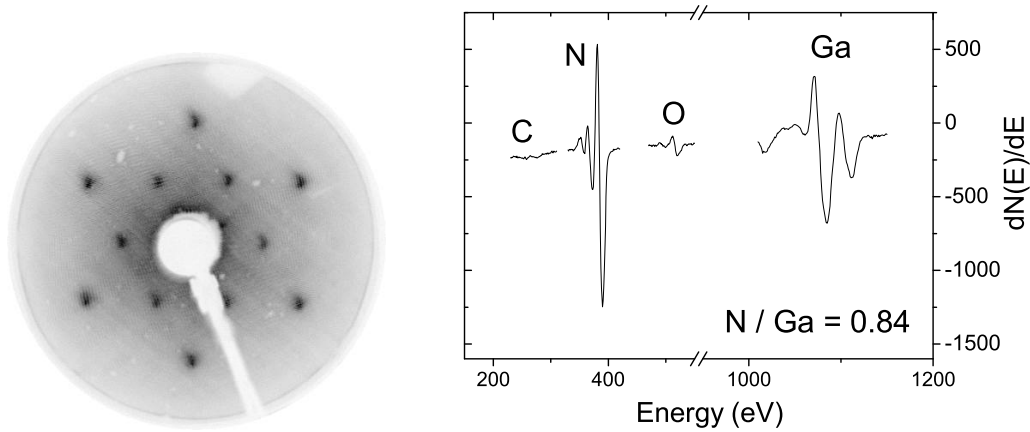

Figure 5.15: Left: $(\sqrt{3} \times \sqrt{3})$-R30° LEED pattern (63 eV, RT) of as-grown GaN(0001) taken after PAMBE preparation with low (910 °C) gallium cell temperature. The six-fold symmetry is clearly resolved and only a $\sqrt{(3} \times \sqrt{3})$-R30° reconstruction can be observed. Right: AES shows a relative nitrogen/gallium ratio of 0.84. The oxygen content detected may be from residual oxygen of the nitrogen source, which adsorbs on the rough, N-rich surface (compare figure 5.16).

but a large roughness of several nm is measured, which results from formation of small
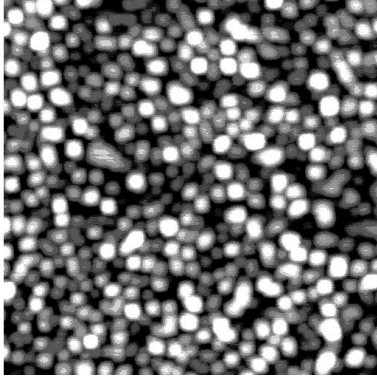
Figure 5.16: $1\mu m^2$ AFM image of as-grown GaN(0001) measured directly after PAMBE preparation with low Ga-cell temperature. The atomic steps observed before preparation are gone, the surface has become rough (approx. 5 nm height scale black/white).

crystals. The strong increase of the surface roughness, leading to an increase of the overall surface area, is a possible explanation for the residual oxygen contamination detected. The ellipsometric spectra before and after preparation in Figure 5.17 show only slight differences. The nitrogen-rich surface spectrum is slightly shifted upwards, which is due to the greatly increased surface roughness as shown by AFM. When approaching the E_1 transition, the $\langle \varepsilon_2 \rangle$ curves tend to cross, which indicates a smaller value for ε_2 typical for roughness overlayers. Thus it can be concluded that two distinct surface terminations have been prepared in MBE together with the respective ellipsometry spectra at high (850 °C) and low (RT) temperature.
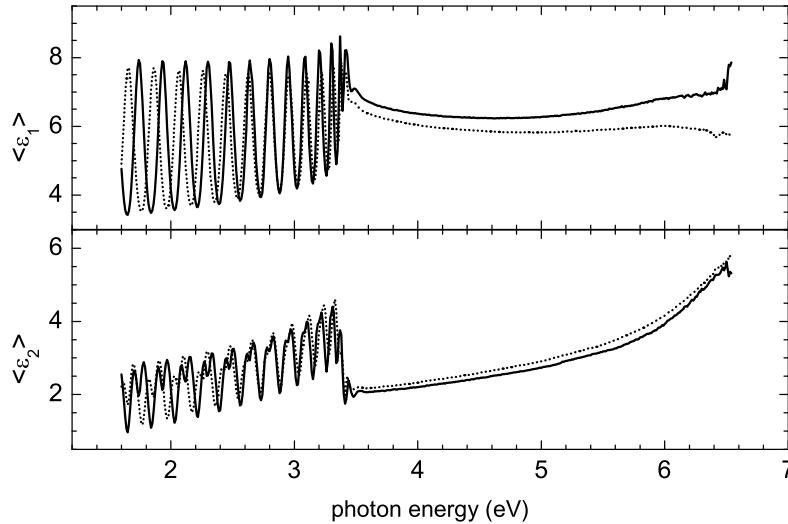
Figure 5.17: $\langle \varepsilon_1 \rangle$ and $\langle \varepsilon_2 \rangle$ spectra of the nitrogen-rich surface (solid lines) vs. "as transferred" surface (dotted) in MBE at room temperature. Only a slight shift in the $\langle \varepsilon_2 \rangle$ spectrum is observed, which is due to the increased surface roughness as proven by AFM in Figure 5.16.

5.4 Comparison of the GaN growth surfaces in MOVPE and (PA)MBE

The possibility to prepare two clearly different surfaces of GaN by solely changing the gallium beam flux, together with a complete surface characterization and interpretation of the ellipsometry spectra, enables interpretation of the MOVPE results by comparison with the in situ (PA)MBE ellipsometry spectra. To simplify the argument, the respective ellipsometry results of $\langle \varepsilon_2 \rangle$ are presented again in Figure 5.18.
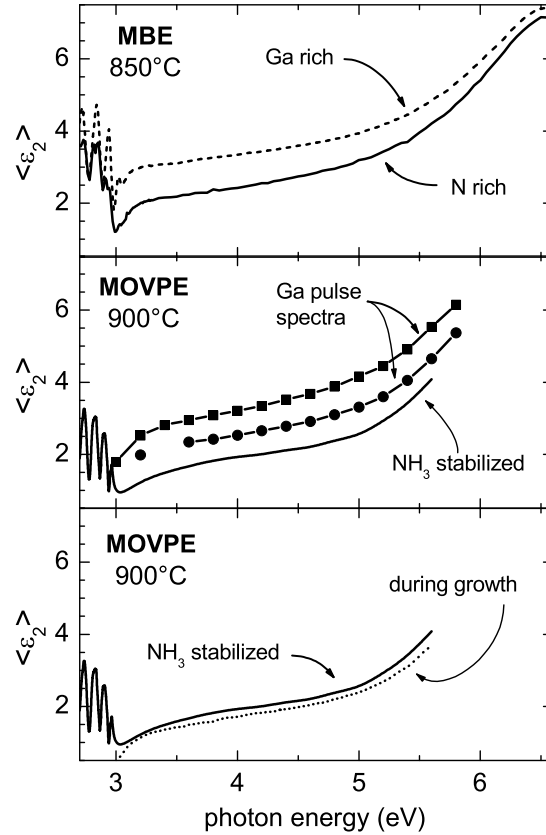

Figure 5.18: Comparison of ellipsometric $\langle \varepsilon_2 \rangle$ spectra during (PA)MBE and MOVPE growth. Preparation of a gallium-rich surface in MOVPE (middle) leads to similar ellipsometry spectra which are known to result from gallium-rich surfaces in MBE (top). The surface in MOVPE during growth is quite similar to what is observed under ammonia stabilization only (bottom) and thus MOVPE GaN proceeds under nitrogen-rich surface conditions.

As one can see from the top and middle spectra preparation of a gallium-rich surface in MOVPE by short pulses of the precursor TMGa in the absence of ammonia leads to spectra similar to those which are known to result from gallium-rich surfaces in (PA)MBE. The first signal increase due to precursor switching (square curve in the middle image of Figure 5.18) can now be attributed to the presence of the gallium double layer structure, which forms immediately after the switching cycle starts. The final value after exponential decrease characterizes the excess gallium-rich state, which is obviously close to gallium droplet formation. Such a behavior was observed in (PA)MBE while cooling the sample to room temperature, accompanied by increasing differences in the $\langle \varepsilon_2 \rangle$ amplitudes (compare Figure 5.14). Thus the excess gallium surface layer, close to the formation of gallium droplets, explains the exponential decay of the MOVPE transients while the gallium precursor is still switched on: the surface layer orders and excess gallium tends to form droplets. The differences in the absolute values in $\langle \varepsilon_2 \rangle$ between gallium rich and nitrogen rich surfaces in (PA)MBE lie between those in MOVPE for the beginning and the end of the gallium switching. A first approximation aimed at a gallium layer thickness of 0.7 nm for preparation of a gallium-rich surface in MOVPE which is much more than the typical double layer of 0.46 nm found by Smith et al. [59] in (PA)MBE growth. Thus a clear definition of the gallium-rich surface structure for GaN MOVPE cannot be given by simply comparing the results in MOVPE and (PA)MBE. At least possible influences of the pyrolysis products from TMGa decomposition like $(Ga(CH_3)_x)$ remain undetermined.

Finally, the most important conclusion can be drawn from the third graph in Figure 5.14 (bottom): the spectra from the ammonia-stabilized GaN surface and from a GaN surface during MOVPE growth are nearly identical. Furthermore, no changes are observed when switching off ammonia for surface stabilization (see for example Figure 5.4). Neither the absence of gallium nor the absence of ammonia during MOVPE has influences on the surface termination, except for roughness formation at high temperatures using hydrogen as carrier gas. This allows to conclude that GaN MOVPE proceeds under nitrogen rich surface conditions, since only adding of gallium leads to significant changes in the ellipsometry response.

This may appear contradictory to the results achieved through SPA measurements by Kobayashi et al. [83] where a transition to gallium rich surfaces with increasing growth temperature is reported for GaN MOVPE. A closer look to the transients they measured reveals time constants for the observed transition of up to 50 s. Since this is more than an order of magnitude slower than what has been observed with ellipsometry in this work, such a transition is believed to result from simple surface roughening which cannot be clearly distinguished by SPA measurements. At least it can be concluded that the nitrogen terminated surface structure during MOVPE growth is probably similar to the simple $(\sqrt{3} \times \sqrt{3})$-R30° reconstruction in GaN (PA)MBE in the absence of gallium terminating the surface during growth.

Chapter 6

Growth of InN on (0001) sapphire

Preface

This and the following chapter 7 will give a brief overview about the progress of InN MOVPE growth and characterization achieved at TUB. Most of the growth experiments were performed in collaboration with M. Drago and research is still on the way with drastic improvement in material quality. Many of the results presented here will bring up more questions which will be answered in the PhD. thesis of M. Drago [160]. The continuous improvement in material properties like layer thickness, composition/impurities, defect density and surface roughness shows that the results presented here are only preliminary. Their presentation will show the state-of-the-art material quality which could be achieved in MOVPE supported by means of in situ spectroscopic ellipsometry. Most of the ellipsometry spectra presented here are interpreted phenomenologically referring to the effective dielectric function $\langle \varepsilon_2 \rangle$. This is due to the lack of the "pure" InN dielectric function and the structural imperfectness of the layers grown. Therefore the following chapter 7 will then give an insight into the dependencies of the InN dielectric properties on sample structure and sample composition as known so far.

6.1 In situ growth observations for InN/sapphire

While searching for the optimum growth parameters in MOVPE all efforts have in common the use of a high amount of reactive nitrogen to suppress InN decomposition. This was achieved either with plasma excited nitrogen radicals [43, 53, 54] or ammonia at an extremely high V/III ratio up to 10^5[50, 55].

   With this knowledge about the necessity of low growth temperatures and high V/III ratios for appropriate growth conditions of InN MOVPE in situ ellipsometry is used to achieve high quality epitaxial layers. In the beginning of this chapter spectroscopic

ellipsometry is used in a quantitative way to accomplish this aim. Since the absorption is related to the imaginary part ε_2 of the dielectric function most of the discussions of the ellipsometry measurements will be made in a phenomenological manner in terms of the measured $\langle \varepsilon_2 \rangle$. Furthermore the use of in situ spectroscopic-ellipsometry will provide a possibility to control and understand the growth peculiarities of InN on sapphire with a relatively small number of experiments. Thereafter the layers grown with the in situ ellipsometry optimized growth procedure will be characterized ex situ to give a state-of-the-art cross reference to what can be achieved for example in MBE. A more detailed description of the optical properties will be given later in chapter 7 when the dielectric function of MOVPE grown InN is to be determined and compared to theoretical predictions (see also chapter 3).

As can be seen from the tables 1.1 and 1.2 in chapter 1 the lattice mismatch between InN and sapphire is as large as 29.2 % taking in account the rotation of the unit cells in the plane perpendicular to the c-axis and therefore nearly twice as large as between GaN and sapphire. Therefore the growth procedure has to start with the classical nitridation of the substrate under hydrogen and 45 mmol ammonia flow at 1050 °C for 10 min to achieve reduced mismatch through the formation of an AlN layer on the surface. (see chapter 4.1). Subsequently the optimum temperature regime has to be found for InN growth. A first approximation for this is already given from literature [41, 42, 46, 50, 55, 161] were growth temperatures from 375 °C to 650 °C are reported. But the different reactors used with different temperature distribution in the gas phase requires the search for the optimum growth temperature regime in the EPIQUIP VP50RP horizontal reactor MOVPE machine used here. Additionally an approximation is given from the Gibbs free energy ΔH (see table 1.1) which is strictly related to the molecular bond strength. ΔH gives an impression how easily thermal dissociation of the compound proceeds. Therefore the relatively low InN growth temperatures reported seem to be reasonable compared to the much higher free energy of the more thermal stable compounds GaN and AlN grown at much higher temperatures. This motivates the growth of a nucleation layer at temperatures far below 500 °C (at least at 400 °C). Since it is known from GaN epitaxy that hydrogen carrier gas etches the growing surface all growth experiments are performed with nitrogen carrier gas. For finding the appropriate epilayer growth temperature the following procedure is used: after nucleation layer growth at 400 °C and 200 mbar (at 41 mmol/min ammonia flow and 0.7 μmol/min TMIn flow rate corresponding to a V/III ratio of 60,000) the temperature is increased to 800 °C keeping the precursor flows constant. Thus NL annealing proceeds during growth. Then the temperature is reduced again while monitoring all changes in the dielectric properties in order to find a region were the highest growth rate can be observed. The corresponding $\langle \varepsilon_2 \rangle$ spectra are shown in Figure 6.1.
The nucleation layer grown at LT is described through a broad interference structure (solid line) with a sharp minimum at 2.7 eV as already known from GaN nucleation
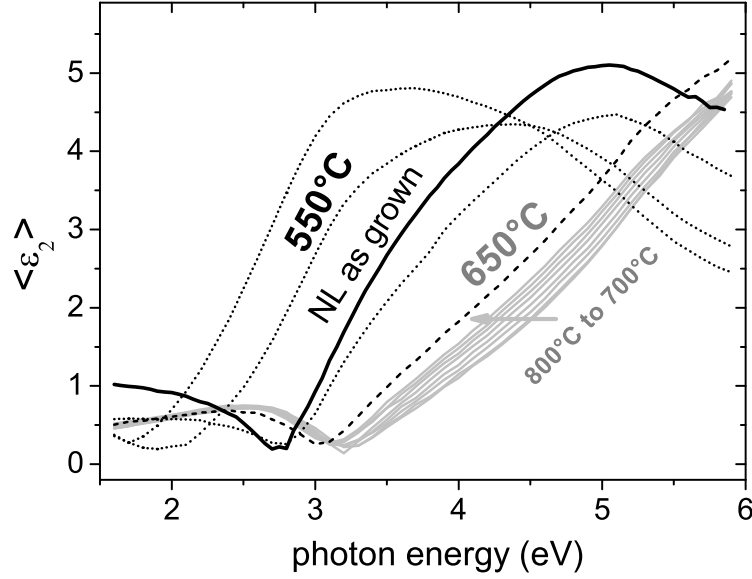
Figure 6.1: Temperature dependent spectra of the InN pseudo-dielectric function $\langle \varepsilon_2 \rangle$ taken during growth between 800 °C to 550 °C. From 800 down to 700 °C nearly no changes are observed (light grey lines). At 650 °C onset of growth can be observed (dashed grey) where the thickness oscillation starts narrowing with the highest growth rate appearing at 550 °C (black spectra). The solid black curve shows the as grown NL at 400°C as starting point.

layer investigated in chapter 4.2. It is not possible to give a detailed description as it was done in chapter 4 for the GaN NL in the absence of the dielectric properties of MOVPE grown InN. So the only conclusion is that growth at 400 °C has lead to the deposition of a layer which shows comparable line shape to a typical GaN NL (compare therefore Figure 4.5) but stretched on the energy scale. Therefore it appears to be approximately half as thick (assuming similar refractive indices). Since for the high temperature of the annealing procedure no growth can be observed the temperature is reduced step wise to 550 °C while continuously measuring spectra every 90 s. Down to 700 °C the shape of the imaginary part of the nucleation layer's pseudo dielectric function remains nearly unchanged. Only a small shift towards lower photon energies is observed. This shift is small enough to suppose that no real growth takes place but only desorption is prevented. At 650 °C this shift of the interference related minima and maxima is increased. The interference structures change their shape as they start to narrow. This is equivalent to a change in the optical properties towards a more dense or even thicker material. This indicates that the onset of real growth can be observed

now. Lowering the temperature to 550 °C this effect is much more pronounced and both, minima and maxima of the pseudo-dielectric function, show a strongly increased shift towards lower photon energies. Furthermore it can be concluded that the optimum growth temperature for highest growth rates under the given precursor fluxes has to be below 550 °C. This is derived from a first in situ approximation of the InN growth rate depending on the growth temperature in Figure 6.2. For evaluation of the growth
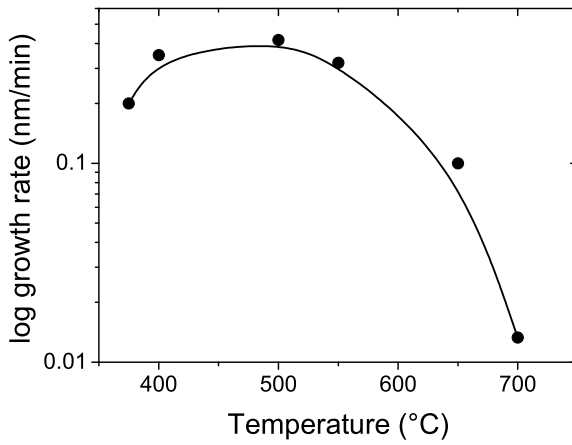

Figure 6.2: InN growth rate determined from in situ ellipsometry spectra between 375 and 700 °C. At 0.7 μmol TMIn flow and a V/III ratio of 60,000 the growth rate shows a plateau between 400 and 550 °C with a maximum of 0.42 nm/min at 500 °C (dots and spline fit as guide to the eye). At 700 °C only very low growth rates of 0.01 nm/min are observed.

rate the use of an "idealized" InN dielectric function for the high temperature regime is necessary. This was obtained using the knowledge about the InN dielectric function from Goldhahn et al. [162] which is shown in Figure 7.2. The corresponding high temperature dielectric function according to the temperature correction of 6×10^{-4} eV/K (deduced in chapter 4.3) was approximated then by a linear shift of 0.35 eV in the photon energy for an average temperature of 600 °C. A temperature induced broadening and damping of the transitions at the band critical points in the dielectric function was not included. Then the layer thickness was calculated for each growth temperature regime to approximate the respective growth rates. This is of course only a hand waving method for an approximation but the results show a clear maximum in the growth temperature region of 500 °C (Figure 6.2). For the given precursor flux this method appears reasonable to optimize the growth temperature.

In fact best results are obtained for 500 °C growth temperature as detailed ex-situ measurements will confirm in the following. With this knowledge in the next step a thick, dense layer of InN has to be achieved. Using the appropriate growth temperature of 500 °C for the MOVPE apparatus the annealing of the nucleation layer was reduced only to this growth temperature. The TMIn flow was increased by a factor of two to achieve a thick layer. Ellipsometry spectra were measured every 10 minutes to monitor the development of layer growth. The result is presented in Figure 6.3 in 4 sets
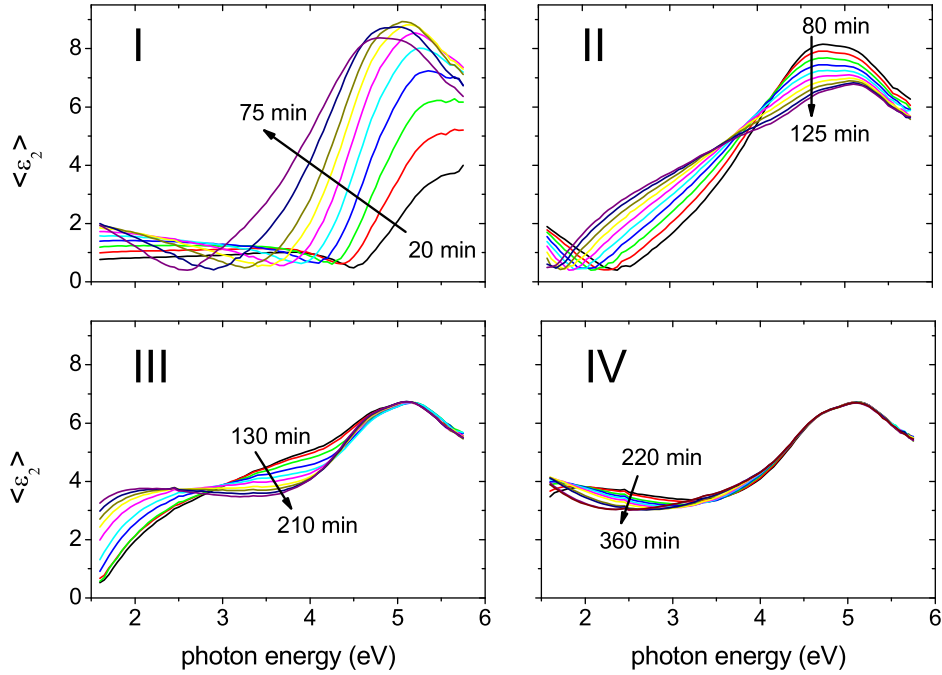
Figure 6.3: Effective dielectric function monitored during six hours growth of InN on sapphire at 500 °C. In the first hour (region I) $\langle\varepsilon_2\rangle$ is dominated by interferences due to the light penetrating the thin layer. Thereafter characteristic spectral features appear around 5 eV when the broad interference splits into two peaks (II). At the end ($III+IV$) these features remain constant while the oscillations in the low energy range are more and more dampened.

of spectra each set showing different phases of growth. Again the discussion of the observed changes in layer properties in situ is done in terms of the imaginary part of the dielectric function $\langle\varepsilon_2\rangle$. Starting again with the broad interference related spectra of the nucleation layer only an increase of the oscillation frequency is observed in the first hour of growth while the overall shape remains unchanged (Figure 6.3 region I). Thereafter the position of the structure around 5 eV remains unchanged and decreases in intensity while the minimum in the low energy range still shifts towards lower energies. Additionally the maximum splits into two clearly distinguishable peaks which cannot be explained any longer as layer interferences (region II). Finally the remaining layer interferences shift towards lower photon energy until they are totally dampened in the measurement range (region $III+IV$). From these in situ observations already some important conclusions can be drawn:

- apparently MOVPE grown InN shows no absorption edge above the low energy measurement limit of $1.6\,$eV (Figure 6.3, IV),

- around $5\,$eV absorption related structures appear which can be related to the predicted higher interband transitions, and

- the InN growth rate is still rather low. After three hours of growth $\langle\varepsilon_2\rangle$ remains affected by interference oscillations in the low energy range caused by light penetrating through the InN layer.

Similar to the procedure from the previous in situ measurement the thicknesses and relative growth rates were calculated from the effective in situ ellipsometry spectra. Ellipsometry yields a total layer thickness of 235 nm after six hours of growth. According to the increased TMIn precursor flow by a factor of two compared to the previous growth run and thus expecting a layer thickness of 300 nm this is in reasonable agreement. The apparent differences in the layer thickness result from the large number of hole-like defects in the layer (see Figure 6.5) which reduces the effective layer thickness measured by ellipsometry. Using the last $\langle\varepsilon\rangle$ spectra during growth as basis for the InN dielectric function at $500\,°$C the relative thickness development of the layer for every $1/2$ an hour was calculated. In Figure 6.4 the evolving relative growth rate during deposition is shown.
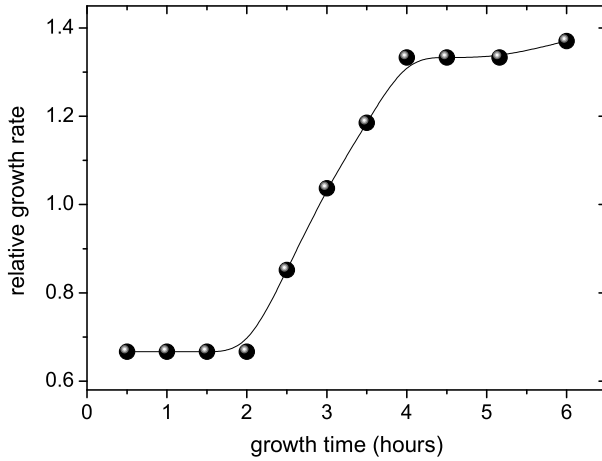
Figure 6.4: Relative growth rate development during $6\,$h of InN growth on sapphire. After the layer starts roughening the growth rate is twice as large as at the beginning in 2D layer growth mode. Ellipsometry yields a total layer thickness of 235 nm after 6 hours. Spline is guide to the eye.

The growth rate evolution is displayed in terms of a relative growth rate since the absolute values determined by ellipsometry of course strongly depend on the position of the InN band edge position influencing the shape and position of the thickness oscillations. Thus the error for the absolute growth rate values is relatively large, especially in the transition range where additionally layer roughening occurs. But a large variation of the growth rate by nearly a factor of two during the whole growth process is

observed. During the first two hours the observed growth rate appears to be rather low with 18 nm/h (eqiv. 0.30 nm/min). After two hours it increases significantly reaching 37 nm/h at the end of this long time growth run. This increase is apparently attributed to a change in the growth mode: at the beginning growth of the thin layer proceeds in a 2D step-flow mode as a result of the improved NL growth procedure. Strain accumulates in the epilayer during growth due to the extremely high lattice mismatch leading to the formation of large defects and parasitic nucleation. SEM measurements as shown in Figure 6.5 have proven the formation of such defects. Thereafter growth proceeds in 3D-mode accompanied by an increase in the growth rate due to the increase in available bond sites. By evaluation of the ellipsometry spectra measured during growth it can be concluded that the critical thickness for layer deterioration under the given conditions is already reached at 50 nm. After cooling the sample to room temperature the clean InN dielectric function was measured as shown in chapter 7 being the basis for further calculations.

Now a general growth recipe resulting from these experiments can be given as follows: to suppress indium memory effects the susceptor is thermally etched at 1050 °C for 20 min under hydrogen flow before each epitaxy run. For epitaxial growth nitrogen has to be used as carrier gas and a total pressure between 200 mbar (nucleation layer growth) and 50 mbar for epilayer growth has to be set. The ammonia flow rate can be kept constant at 41 mmol/min. The low temperatures always enforced a high ammonia flow rate to compensate for the low dissociation ratio at these temperatures, while the TMIn rate was varied between 0.7 (used for the low temperature nucleation layer) and 1.4 μmol/min, corresponding to a highest V/III ratio up to 60,000; at V/III ratios below 30,000 In droplet formation was observed during growth at these temperatures. To achieve defect free InN layers growth of more than 50, maximum 100 nm InN should be avoided up to now.
In the following thick InN layer grown under these conditions are analyzed ex-situ to determine the physical properties of MOVPE InN.

6.2 Ex-situ characterization of InN/sapphire

The samples taken out of the reactor appear black and mirror-like, a clear hint towards a band edge energy E_0 below the visible range of 800 nm or approx. 1.55 eV. Optical microscopy images reveal several small defects of the layer in the μm range. Further investigations taking scanning electron microscopy (SEM) images (Figure 6.5) show a reasonably smooth surface with several small, facetted pits. The morphology observed indicates a coalesced layer formed by initial island growth. In addition to the pits, small crystallites with an average size of about 0.3 μm stick up from the surface showing growth centers induced through parasitic nucleation. The dark edges in the image indicate the beginning lift off of small plates. As a consequence of such a lift

off, on several places on the epilayer holes were found. There islands of typically $3\,\mu$m in diameter have peeled off, responsible for the defects observed in optical microscopy and indicating a large strain in the layer. Similar growth defects have been found in MOVPE growth by Jain et al. already during growth despite the use of different buffer layer approaches [163, 164]. This defect formation is attributed to the already mentioned higher lattice mismatch between InN and the sapphire substrate compared to GaN/sapphire and the up to now non-optimized nucleation layer procedure.
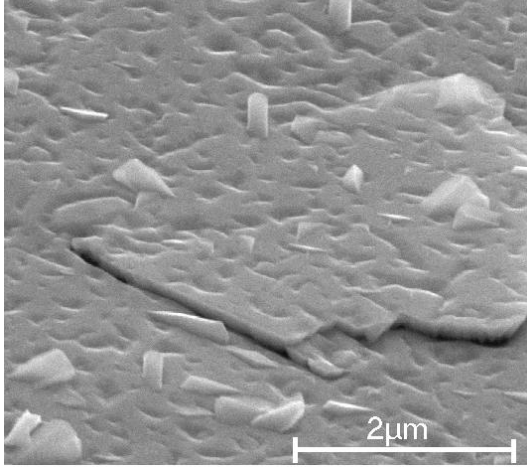
Figure 6.5: SEM image of an InN sample grown at $500\,^\circ$C. Due to the large strain parts of the layer begin to peel off while parasitic nucleation has led to growth of small crystals sticking up from the surface.

Despite these visible defects an evaluation of the structural properties by X-ray rocking curves and Raman spectroscopy reveals a high layer quality. Figure 6.6 shows ω-scans (rocking curves) of the InN (0002) reflection with the respective growth parameters for the four samples listed in the Table 6.1 below. The best samples, grown with the highest TMIn flow possible at 500°C on a nucleation layer as described before, possess a FWHM of about 0.5°. Higher temperatures and lower indium rates lead to a significant broadening of the peaks, whereas samples "a" and "c" are grown under the same conditions but have different thicknesses. The consequence of increasing thickness is a slow deterioration of the crystal quality. Samples thicker than $200\,$nm all have broader and less intense layer reflections. This is also in agreement with the in situ ellipsometry measurements were a slow increase of stray-light, the diminution in the absolute value of the dielectric function and an increase in the ellipsometric parameter $\cos\Delta$ (see chapter 3) is observed during growth. All these changes are mostly affected by surface roughness formation which can be either attributed to parasitic nucleation or the formation of holes. A comparison of the best FWHM of $0.48\,^\circ$ of the ω-scan to the values published from e. g. Nanishi et al. for RF-MBE grown InN thin films shows that MOVPE material can be superior since for similar layer thickness the FWHM is as twice as large in RF-MBE [28]. For an additional proof of the good layer quality achieved Raman studies were performed under parallel ($E_I \parallel E_S$) and crossed ($E_I \perp E_S$) polarization configuration. In Figure 6.7 a pronounced appearance of the E_2
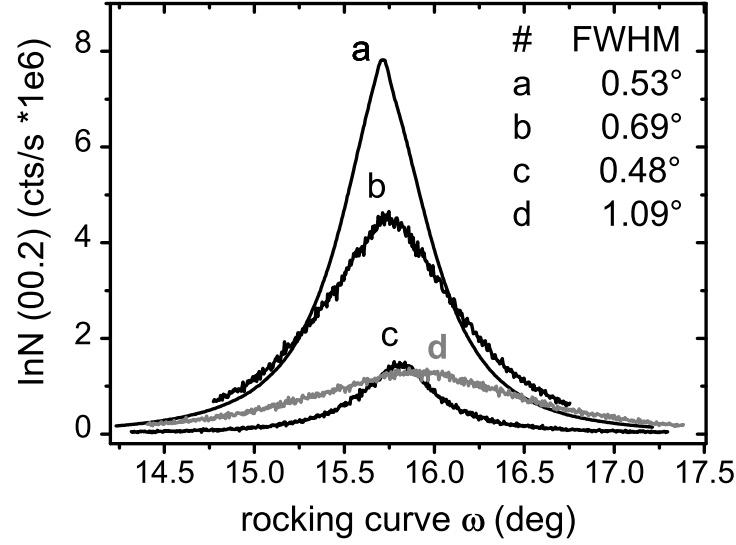
Figure 6.6: XRD ω-scan of the (0002) reflex of four different InN samples grown at 500 and 550 °C, respectively. Increased thickness broadens the FWHM (b vs. a) as well as high temperature growth at 550 °C (d). Here bulging of the layer is suspected to be the origin for the increase in FWHM. The respective growth parameters are given in table 6.1 below.

Sample	FWHM (0002) (°)	thickness (nm)	T_{growth} (°C)	TMIn flux (μmol/min)
a	0.53	200	500	1.4
b	0.69	200	500	1.05
c	0.48	50	500	1.4
d	1.09	200	550	0.7

Table 6.1: Growth parameters listed for the four InN samples characterized via XRD as shown in Figure 6.6. The ammonia flow was kept const. at 41 mmol/min for each sample.

and A_1 (LO) Phonon modes of hexagonal InN is shown indicating the growth of a well ordered, wurtzite layer without cubic inclusions. The A_1 TO mode (at $440\,cm^{-1}$) is forbidden for $k\|z$ [165] and does not appear. The polarized spectra (inset in (Figure 6.7) correspond well to the selection rules of hexagonal InN verifying the structural results. No hint for residual cubic modifications such as broad A_1 LO modes are observed as reported from [42]. Through variation of the excitation energy from $2.02\,eV$ ($614\,nm$) to $2.54\,eV$ ($488\,nm$) the layer quality was inspected along the growth direction. It can
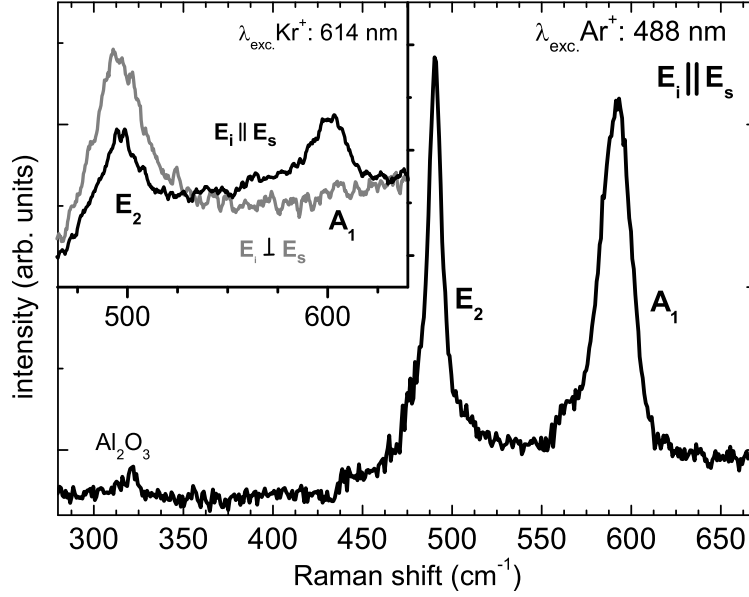
Figure 6.7: Raman spectra taken for parallel polarization ($E_I \| E_S$) showing high intense A_1 and E_2 LO modes of hexagonal InN. The crossed polarization (inset) agrees well with the expected selection rules (after [165]). The lower excitation energy of the 614 nm laser line shows broadened FWHM according to higher defect density with increased penetration depth.

be observed that the FWHM of the A_1 and E_2 modes decreases with increasing photon excitation energy. Since the penetration depth of the light decreases with increasing energy this indicates a significant defect reduction with increasing layer thickness. The fact that the sapphire optical phonon is not observed at $406 \, \text{cm}^{-1}$ and only a small residue can be found at around $320 \, \text{cm}^{-1}$ demonstrates that the light does not penetrate through the layer and is nearly fully absorbed indicating high layer coalescence. The absolute FWHM of the phonon modes is $10 \, \text{cm}^{-1}$ for the E_2 mode and $20 \, \text{cm}^{-1}$ for the A_1 mode, respectively. This is in reasonable agreement with values of $5 \, \text{cm}^{-1}$ for the E_2 mode from $0.7 \mu\text{m}$ thick layer grown in MBE as published from Davydov et al. [166] showing similar layer quality for the thin MOVPE InN. Superior values as published from Kurimoto et al. suffer from missing complementary optical characterization of the MOCVD grown layer.

Summary

In conclusion of the in situ ellipsometric monitored growth experiments of InN on sapphire one can state that with a small number of experiments high quality MOVPE grown InN could be achieved. This was mainly due to the phenomenological approach of observing the absorption related $\langle \varepsilon_2 \rangle$ spectra and correlating them to the predicted InN dielectric function after [12, 162]. The wurtzite layers with good crystalline quality are grown at low temperature of 500 °C and high V/III ratios up to 60,000. They possess a specular, shiny black surface with good morphology, a FWHM of 0.5° for the (0002) rocking curve reflection and narrow Raman modes which appear in agreement with the symmetry selection rules. Up to now higher growth temperatures result in significant broadening of the FWHM. Layers thicker than 0.3 μm showed cracks and small parts peeled off obviously due to a large strain between layer and substrate. This requires improvement of the nucleation layer growth procedure possibly including an optimized substrate nitridation and an increase of the nucleation layer thickness or a change in nucleation layer material to GaN or AlN. Additionally the observed parasitic nucleation has to be reduced. One way could be a controlled rise of the growth temperature to improve adatom mobility on the surface and to favor a slight etching process like it is known from GaN epitaxy. In GaN epitaxy a significant smoothing of the layers results from the etching effect of atomic hydrogen. As mentioned in the beginning of this chapter growth optimization still goes on including the processes listed before. This is part of the PhD. thesis of M. Drago which will be published soon [160]. A comprehensive lecture of these new results is given in [167–172].

Chapter 7

Dielectric function of InN

Up to now only little is known about the dielectric properties of InN. Few publications [162, 173] deal with the dielectric function of InN grown with either MBE or MOVPE. Furthermore the published results are restricted in the high energy range to 5.5 eV (see Figure 7.2) and the existing discrepancies due to the different preparation techniques as shown there are not fully understood, yet. Therefore this chapter will briefly summarize and describe these results. Then a first approximation of the ellipsometry measurements from chapter 6 is given where more features on the high energy side of the dielectric function show up which have to be investigated. Thus an exact determination of the dielectric function for MOVPE InN and a comparative study of the dielectric properties of the differently grown materials seem to be of importance. Influences like surface roughness and oxidation effects as well as the "band edge question" are discussed here. Finally a proposal for the DF in the range from 0.7 to 6.5 eV based on MOVPE grown InN will be given together with an analysis of the energetic position of the band critical points (BCP analysis).

Some results published on the InN dielectric function

As already mentioned in chapter 3 theoretical calculations of the band-structure are quite helpful to understand and interpret the experimental results derived from optical measurements. With the upcoming band edge discussion for InN a first theoretical calculation of Bechstedt et al. [12] was published in 2003 where a small band gap was predicted as shown in Figure 7.1, left image. Furthermore these calculations expected InN to have intense interband transitions at photon energies around 5 eV. Since up to now different experimental results are published for InN being far from showing congruent electronic properties (cf. Figure 7.2) which should be investigated in more detail. With the low energy correction of the InN band edge position another band dispersion calculation from Fritsch et al. was then published were these transition energies are
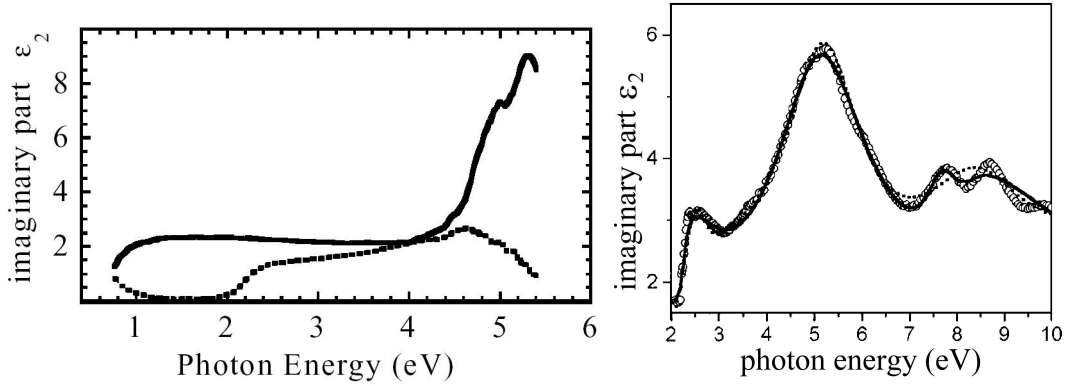
Figure 7.1: Left: theoretical prediction of the imaginary part of the DF for wurtzite InN (after Bechstedt et al. [12]). While the E_0 position is expected to be around 1 eV several intense absorption maxima are calculated in the energy range below 10 eV for the light polarized parallel (solid line) as well as perpendicular (dashed line) to the c-axis. A corresponding band structure calculation (after [174]) shows several possible transition energies between higher bands.

correlated with the respective valence and conduction band transitions [174]. The calculated band structure is also shown in Figure 7.1, right image. Additionally several publications appeared allowing for comparison of the dielectric properties between differently prepared InN films. Some of these results are summarized in Figure 7.2:

The publication of Goldhahn et al. [162] compared the dielectric function of MBE grown InN from the group of W. J. Schaff from Cornell University with sputtered material from the group of T. L. Tansley from Macquarie University (left graph in Figure 7.2). Obviously the specific growth techniques strongly influenced the material properties. Apart from the difference of the band edge position the sputtered material shows no features in the high energy range of the dielectric function.

The properties of MOVPE grown material from the group of Guo et al. (right image in Figure 7.2, taken from [173]) indicate a band edge of around 2 eV in accordance with absorption measurements [175] and also point towards the existence of high energy structures around 5 eV. Furthermore for the first time an apparent similarity between the ab-initio calculations from Bechstedt et al. [12] and the measurements on the MBE grown material could be observed.

All these contradictory results show the need for improve in material quality and a detailed analysis of the InN dielectric function from MOVPE grown material.

Figure 7.2: Left: Comparison of the imaginary part of the dielectric function of MBE grown (solid line) and sputtered InN (dashed line) after [162]. Right: Imaginary part of the dielectric function of MOVPE grown InN (together with differently modeled dielectric function , solid and broken lines) showing a band edge position around 2 eV and intense structures in the high energy range (after [173]). While MBE and MOVPE grown InN show apparent similarities to the theoretical prediction (cf. Figure 7.1) the dielectric function of sputtered InN is totally different.

7.1 Determination of the InN bandgap

To evaluate the InN dielectric function in the range of the expected band edge we used an infrared (IR) ellipsometry ex situ setup which was provided in cooperation by *SEN-TECH instruments* GmbH, Berlin. The IR measurement range from 0.5 eV up to 3.5 eV gave a wide overlap in the pseudo-dielectric function to the in situ determined values to guarantee matching of both measurements and to ensure that the sample properties did not alter too much during transfer to *SENTECH* company. The transfer was organized in a nitrogen filled preserving jar and the sample was measured directly after taking out of the jar. So possible oxidation influences on the band edge position were reduced to a minimum. In Figure 7.3 the composed IR (dotted lines) to UV (solid lines) measurements of the pseudo-dielectric function are shown together with the calculated dielectric function (gray lines) in the band edge region. The two measurements match quite well in the region between 1.6 and 3.5 eV concluding that the sample transfer procedure was chosen right. Examining the as-measured effective DF at a first glance one can divide the DF in two regimes for a first interpretation of the measurement:
In region one, which is above 2 eV and corresponds more or less to the VIS-UV range of the in situ ellipsometer, the effective DF is dominated by the three intense interband transitions located between 4.5 eV and 6.5 eV. In region two below 2 eV the effective DF is dominated by a huge interference oscillation. This is mostly due to the low layer thickness which is approximated from SEM images (see also Figure 6.5) to be 150 nm for this sample. Thus the light partially penetrates the whole layer, gets reflected at
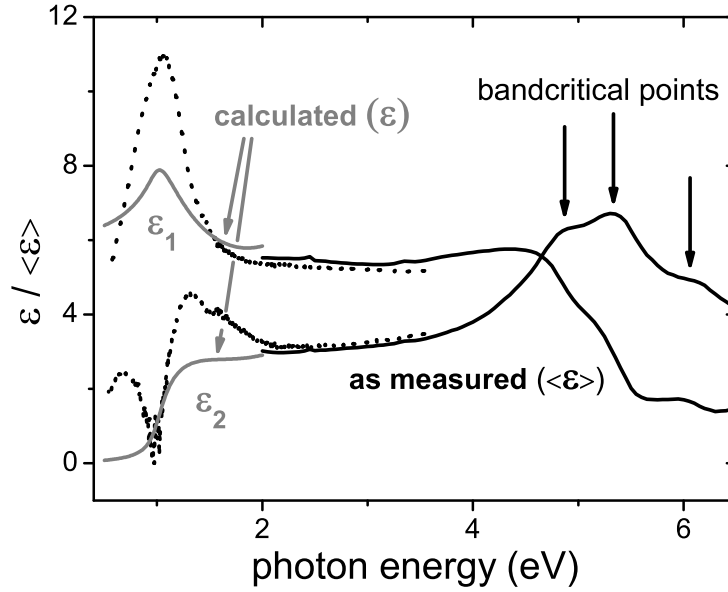
Figure 7.3: InN pseudo-dielectric function from IR (dashed lines) to UV (solid lines) with evaluation of the dielectric function near the band edge region (gray lines). The near band gap region region was calculated according to the Tanguy model determining an E_0 of 1.05 eV and a relatively high broadening Γ of 180 meV.

the substrate interface and leaves the layer even for photon energies where absorption would be expected. This behavior is partially increased through the holes formed in the layer already during growth. Therefrom and from the SEM image we can conclude that a simple four layer stack (substrate, layer, roughness, vacuum as it was proposed in chapter 3) will not sufficiently allow to evaluate the exact dielectric properties and several simplifications have to be made. This concerns the distribution and size of the parasitic crystals on top which are not comparable to the classical expression of a surface roughness. The same holds true for a separation of the large holes in terms of an EMA model which is not possible due to the size of the holes, being in the range of several μm and even larger than the ellipsometry wavelength. Even an assumption of a linear mixture of InN and voids (vacuum) would not lead to totally reliable results because the InN/voids ratio can not be determined properly from the SEM images and also the size of the defects varies in a wide range. Consequently the calculated total layer thickness determined from ellipsometry will always be to small, namely being 95 nm for the 150 nm SEM determined thickness value. The 1 nm rms roughness value on top of the layer determined with ellipsometry appears to be much to small com-

pared to the approximately 20 nm ($5 \times 5 \mu m^2$ scan region) value determined by AFM. Obviously the large crystals do not contribute to the optical surface roughness so much. This is supported by AFM measurements in smaller areas between the parasites were significantly lower roughness values are measured.

For evaluation of the band edge position a first approximation can be given guide-to-the-eye: in the $\langle \varepsilon_2 \rangle$ spectrum a sharp edge in the interference related structures can be observed around 1 eV. In the first step for exact evaluation of the band edge position the energy range was restricted to the region were the band edge was expected, namely below 2 eV. Therefore we used the same Tanguy model function/approximation which already proofed its suitability in chapter 4 for determination of the band edge position of the defective GaN NL. The resulting dielectric function (gray lines) shows up with a band edge energy position at 1.05 eV and a broadening parameter Γ of 180 meV which reflects the highly perturbed crystal structure of the InN layer. As already indicated by the fact that the interference oscillation is totally dampened at 2 eV the band edge value E_0 of this MOVPE grown InN layer is far below the formerly accepted 1.86 eV from [11] but very close to the theoretically predicted value of around 1 eV from Bechstedt et al. [12]. Even if this is not in accordance with the recently published values of 0.76 eV by Davydov et al. [49, 176] these differences can be explained very easy:
First of all the photoluminescence measurements published show very broad structures where no excitonic recombination lines can be resolved. This indicates a high defect density which is accompanied by a high carrier concentration in the mid 10^{20} range resulting in a very strong Burstein-Moss shift. Therefore the published result of 0.76 eV from Davydov et al. is already Burstein-Moss shift corrected and higher values are measured for layers with high carrier concentration.
A second possibility is a recombination mechanism which is bound to a defect center like a deep donor induced either by oxygen impurities as known from the early stages of GaN growth [141] or by excess nitrogen due to the imperfect growth mechanism of InN performed at very high V/III ratios (see chapter 6 and 1 and [177]). Both explanations allow for a shift of the observed emission wavelength in a wide range which can not be easily taken in account when evaluating the ellipsometry spectra.
Additionally some of the samples from which photoluminescence measurements report a band edge far below 1 eV show absorption edges shifted to higher energies [178]. For a better and more accurate description of these parameters as well as the absolute position and "intensity" of the higher interband positions the layer quality has to improve because all these deficiencies can not be considered in a simple optical model. Since only a few samples were grown and no systematic growth dependency studies were performed in the frame of this thesis (this will be done in the PhD. thesis of M. Drago [160]) the results presented here can not claim for completeness. Meanwhile spatially resolved cathodoluminescence spectroscopy studies on similarly grown MOVPE InN by M. Phillips et al. [172] revealed a much lower band edge position of around 0.8 eV

for these films.

Unfortunately more peculiarities of InN have to be taken in account like a relatively quick oxidation of the layer which also influences the dielectric properties. This is discussed in the next paragraph.

7.2 Oxidation effects in InN

Up to now nearly all ellipsometric measurements have been performed in situ in the MOVPE reactor avoiding contamination with air and moisture. The first ex situ investigation has been the IR measurement in the InN band edge region in the previous paragraph. The remaining question is: does a freshly grown InN layer react with air and if so how can this reaction be determined via ellipsometry? Therefore we measured the
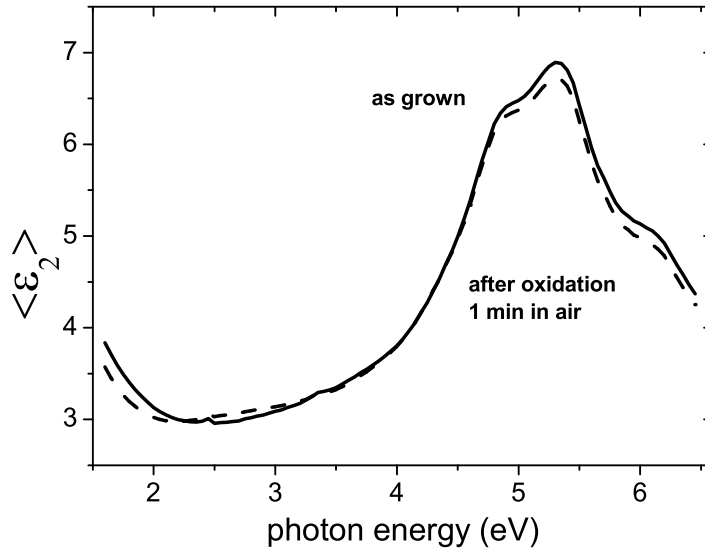
Figure 7.4: InN $\langle \varepsilon_2 \rangle$ in the VIS-UV range directly after growth (solid line) and after 1 min exposure to air (dashed lines). A huge decrease of intensity in the range of the higher interband transitions and an increase in intensity in the region below shows the influence of an adlayer.

effective DF of freshly grown InN after cooling to room temperature inside the reactor. Then the reactor was opened for 1 min and the sample was exposed to air. Again the DF was measured as shown in Figure 7.4, dashed line.

We observe a typical adlayer formation (see also chapter 3) which is characterized by a dampening of the higher transition intensity (around 5 eV) and an increase in the energy range below. The difference in the interference related increase in $\langle \varepsilon_2 \rangle$ close

to the E_0 position may be also due to slight variations in layer thickness when measuring at different spots of the sample. For determination of the adlayer thickness the knowledge of the material formed on top of the InN epilayer is necessary. The most favorable solution is the formation of some In_XO_Y compound like it is also known from for example GaAs adlayer formation [179]. Since the oxidation of InN at 450°C is already reported to form In_2O_3 which can be detected in XRD diffraction patterns [180] the formation of a similar composition out of the MOVPE grown InN is expected, too. Since no optical data for determination of the dielectric properties for an adlayer calculation are available for In_2O_3 a single crystalline layer had to be prepared. This was then measured with our ellipsometry setup. Therefore a thin (100 nm) InN epilayer on sapphire was heated step wise to temperatures as high as 450°C in dry air atmosphere. After every 10 min it was cooled down to room temperature performing ellipsometric measurements. The whole process of oxidation could be clearly resolved in every heating cycle finally being completed after 2 hours as shown in Figure 7.5. Here the higher
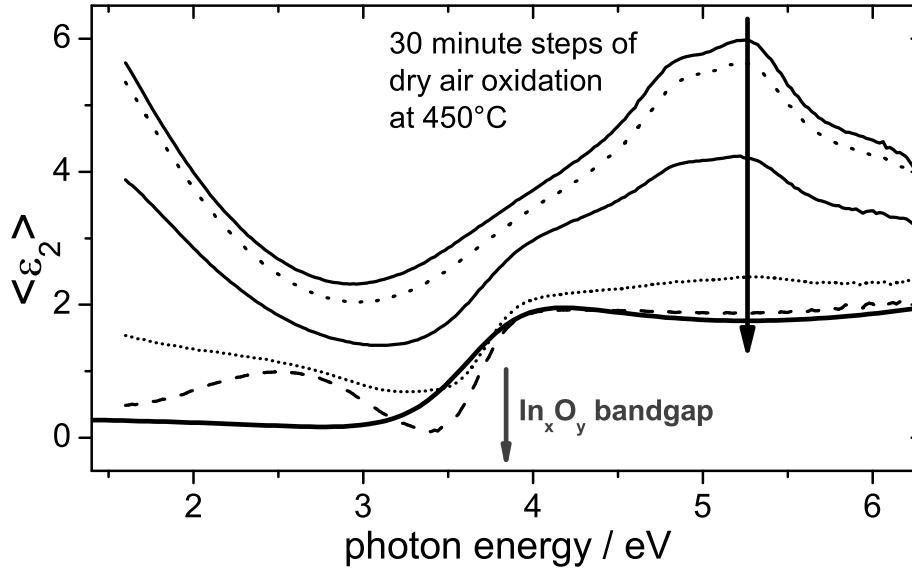
Figure 7.5: $\langle\varepsilon_2\rangle$ spectra during oxidation of a 100 nm thin InN epilayer. Oxidation was performed at 450°C in dry air while ellipsometry measurements were performed in between every 10 min at room temperature. Each graph shown here corresponds to 1/2 h oxidation time. The lowest (solid) line shows the calculated In_2O_3 dielectric function .

interband transitions of InN vanish accompanied by a shift of the intense interference oscillations to higher energies. This is a clear hint towards a shift of the InN band edge position with increasing oxygen content. Finally a step like absorbance edge appears close to 4 eV pointing at the oxide band edge position. A calculation of the oxygen

layer properties using a 4-layer model of sapphire, In_2O_3 plus a 50% In_2O_3/air mixture for describing a roughness overlayer and air leads to a slightly increased overall layer thickness of 120 nm. The oxide layer was assumed to be a relaxed lorentzian type which consists of a set of two oscillators. By varying the respective oscillator parameters they can be adjusted in their energetic position and their oscillator strength which allows for easy calculation of the band edge position and the refractive indices below and above this band edge position. As a result we find the oxide band edge to be 3.9 eV which is in congruence to the findings from Zollner [179] who determined the influence of native oxides on the pseudo-dielectric function of III-phosphide, -arsenide and -antimonide semiconductors. There the mixed oxide phases on the surface are clearly observed for the less stable compounds (InAs, InSb) pointing towards a decrease in band edge position with lower binding energy (for InSb the oxide overlayer band edge was determined to approximately 4.5 eV). For the temporal description of this oxidation process a linear mixture of the InN effective dielectric function and the oxide dielectric function had to be assumed. Thus the oxidation process does not proceed layer-by-layer but obviously along some defects in the whole InN epilayer. The so gained indium-oxide dielectric function (solid line in Figure 7.5) now allows for calculation of oxide overlayer effects on the Indium nitride pseudo-dielectric function. Also an influence on the band edge position through alloying can be presumed now.

The oxidation process itself is proven by XRD measurements, showing a decrease in the rocking curve intensity of the InN (00.6) reflection by nearly two orders of magnitude and a strong increase in the oxygen signal in EDX measurements for the fully oxidized sample as shown in Figure 7.6. Here a small oxygen and carbon contamination can be detected after transfer into the SEM for the pure InN sample (gray lines) together with a relatively high nitrogen signal (one should keep in mind that the nitrogen "Streuquerschnitt" is rather small compared to the other detected elements). After oxidation (solid black line) the oxygen as well the carbon and indium signals are increased and the nitrogen peak is vanished. The sample can be described as fully oxidized.
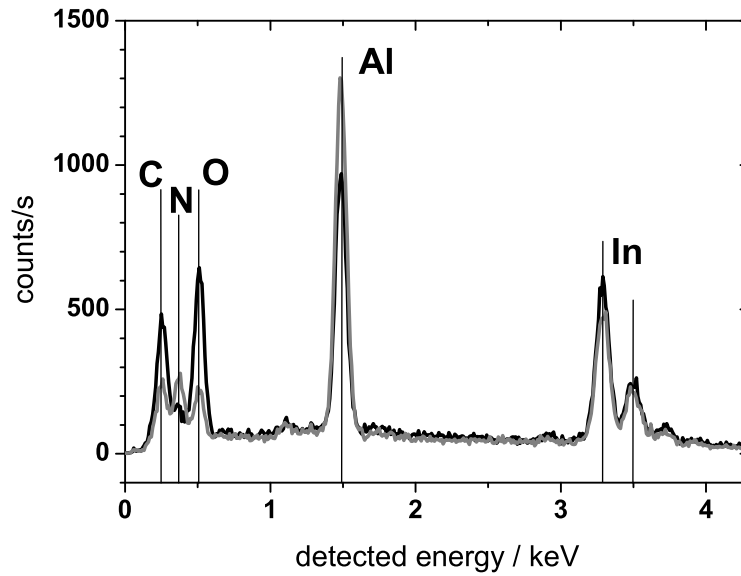
Figure 7.6: EDX spectra of the "pure" InN (gray line) showing a distinct nitrogen peak between the carbon and oxygen contaminations due to the transfer in air. After oxidation this peak is vanished and the other ones are increased. The sample is totally oxidized.

7.3 Band critical point analysis of InN

As can be seen already in Figure 7.3 the pseudo-dielectric function of InN exhibits several intense maxima in the high energy range. They point towards higher interband transitions at high symmetry points in the Brillouin zone (see also chapter 3). Their energetic position can be determined either guide to the eye (of course with low accuracy) or by calculating the 2nd derivative of ε_1 and ε_2 . The latter is the more precise and correct way but both methods require the dielectric function of a smooth, ideal layer. Therefore the already known overlayer effects like e. g. roughness for calculating the dielectric function of smooth, ideal InN have to be considered. This was done according to the NL roughness determination in chapter 4 where a simple but useful connection between the EMA roughness and the physical surface roughness determined by AFM was established. For this purpose a 3 nm thin roughness EMA overlayer was assumed which was simply subtracted from the as measured pseudo dielectric function as can be seen in the left graph in Figure 7.7. This value is of course only an approximation based on the fact that the InN layer grown are quite smooth between the center of parasitic nucleation where large crystals appear. When calculating the 2nd derivative
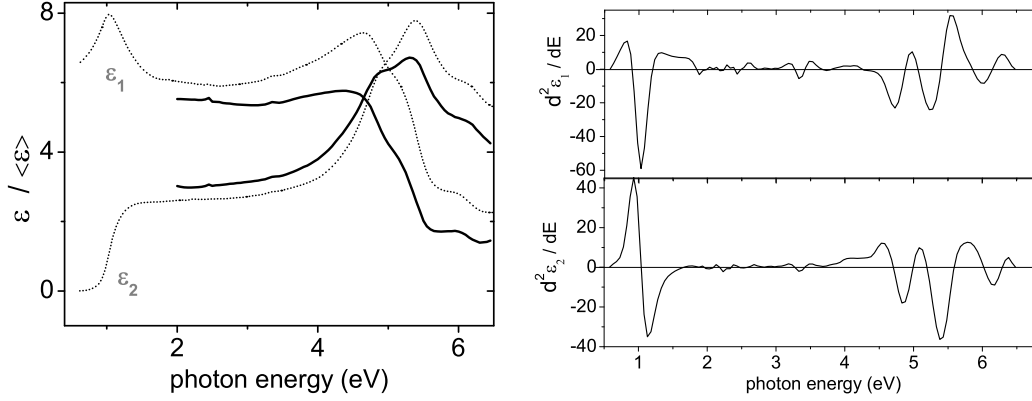
Figure 7.7: Left: dielectric function of MOVPE grown InN after correction of a 3 nm rough overlayer (dotted line) according to the results from chapter 4. Right: 2nd derivative of the corrected dielectric function clearly showing three higher interband transitions and allowing determination of their exact energetic position.

$d^2\varepsilon/dE^2$ of the corrected InN dielectric function no hint is given for additional transitions. To the following transitions T_0 - T_3 the energetic positions can be assigned by a simple lorentzian fit procedure of the 2nd derivative: 1.08 eV (according to the band edge position of 1.05 eV) for T_0, 4.85 eV for T_1, 5.40 eV for T_2 and finally 6.17 eV for T_3.

In comparison to the previously published InN dielectric function from Gold-hahn et al. [162] (as shown in Figure 7.2) the existence of a third interband transition above 6 eV is proven now in accordance with the theoretical calculations from Bechst-edt et al. [12] (cf. chapter 3). There three interband transition are expected in the energy range between 4 eV and 6 eV. A closer look to the data from Guo et al. (also Figure 7.2) also revealed a small shoulder around 6 eV for the MOVPE grown InN. Comparing these results with the latest theoretical band dispersion calculations of Fritsch et al. (cf. Figure 7.1 in chapter 3) [174] these higher interband transitions may be related according to their energetic positions as follows: T_1 may originate from transitions at the U and M point of the Brillouin zone while T_2 originates from L and U transitions and T_3 possibly from M, Γ or H transitions. All these experimental values agree quite well with the theoretical ones within a deviation of 0.1 eV or less.

Summary

Having determined the band edge position of thin MOVPE grown InN to 1.05 eV (at room temperature) the previous work will of course not clarify the band edge question. The difference of around 0.3 eV to the nowadays often cited 0.75 eV observed from

photoluminescence measurements at low and room temperature [49, 176, 178] may be related to the high amount of structural defects in the layer. Furthermore many researchers report on a similar discrepancy between photoluminescence and absorption measurements which is somewhere in the order of 0.2 eV [178] for identical samples. More experiments with improved material (higher thickness, reduced defect density) are necessary to determine the electronic properties of "pure" InN. Also the oxidation process which took place in the whole layer indicates a relatively high structural defect density of the samples presented here. Since MOVPE grown InN also exhibits a strong absorption feature around 1.2 eV [181] the origin of the band edge question will not be detected in the next month and give rise to further discussions. One major point of interest will be the influence of impurities like for example oxygen or excess nitrogen [177] on the structural and electronic properties. With the precise determination of the energetic position of the higher interband transitions the congruence between the theoretical predictions and experiment is proven emphasizing once more the necessity of theory paving the way towards new discoveries.

Summary

In situ spectroscopic ellipsometry (SE) during nitride MOVPE on sapphire allows to monitor the whole growth process and reveals several remarkable characteristics. During sapphire nitridation with ammonia the threshold temperature and the duration of the process have been determined resulting in a 4 nm thick, crystalline AlN layer. Furthermore ellipsometry demonstrated the influences of the growth setup on the individual process conditions: high temperature "cleaning" of sapphire under hydrogen atmosphere resulted already in a slight nitridation layer through dissociated GaN from inside the reactor forming ammonia. These variations upon the reactor conditions influenced the seed formation and nucleation layer coalescence on sapphire with consequences for the nucleation layer growth rate and thickness. For reproducible epitaxial conditions and optimum layer quality consideration of this influence on the growth rate is absolutely necessary and SE allows to monitor the layer growth for this purpose.

During growth of thin GaN nucleation layer (NL) an estimate of the crystalline quality is given by ellipsometry. The existence of cubic and hexagonal phases in the NL were determined with their ratio strongly depending on the growth conditions such as the V/III ratio and the growth rate. Highest cubic fractions were observed at high NL growth rates. This is of importance since best epilayer qualities are achieved only at high NL growth rates which is clearly correlated with a high cubic proportion in the NL. In the subsequent NL annealing procedure of the NL the transformation from the cubic phase into a hexagonal phase could be tracked in situ showing that the procedure is already accomplished between 800 °C and 950 °C. There is no need of a further long term high temperature processing since nucleation layer degradation at high temperatures is observed when the phase transformation has completed.

Thick GaN epilayers showed a high crystalline quality when grown on optimized NL. Low temperature photoluminescence spectra were dominated by narrow donor bound and free X_A and X_B excitonic emission lines. The corresponding pseudo-dielectric function of the as-grown non-oxidized GaN epilayer revealed a strong absorption feature directly below the absorption edge which can be attributed to a defect related-transition, allowing for epilayer quality control already during growth.

A comparison of differently prepared GaN surfaces in MOVPE and (PA)MBE via the comparison of the ellipsometry spectra during preparation allowed for an indirect

determination of surface stoichiometry during GaN MOVPE. The ellipsometry spectra in MOVPE under growth and ammonia-stabilized conditions were similar to those prepared in (PA)MBE under gallium-poor conditions. MOVPE spectra measured under short trimethylgallium pulses in the absence of ammonia were similar to the (PA)MBE results which are well known to be gallium-rich and which could be ascribed to the formation of a 0.9 nm thin gallium adlayer. The most important conclusion from these experiments is that GaN MOVPE must proceed under nitrogen-rich conditions with a surface structure similar to the $(\sqrt{3} \times \sqrt{3})$-R30° which is known from (PA)MBE.

By means of in situ SE the growth process of InN on sapphire could be optimized, too. With a small number of experiments high quality MOVPE grown InN could be achieved which revealed a band edge feature in the dielectric function around 1.05 eV. The discrepancy to the nowadays more accepted value of 0.7 eV to 0.8 eV could be attributed to the remaining defects inside the InN layers. Analyzing the growth process of InN MOVPE on sapphire with in situ SE it was found that only a narrow growth temperature window around 500 °C allowed high growth rates. A significant layer deterioration during InN growth through strain accumulation caused by the high lattice mismatch could be detected. This was achieved through growth rate calculations showing a drastic increase at the transition from 2-D layer to 3-D island growth.

Finally the dielectric function of MOVPE InN was calculated from such layers showing an absorption edge of 1.05 eV and three higher interband transitions at 4.85 eV for T_1, 5.40 eV for T_2 and 6.17 eV for T_3. The absolute positions of these transition energies appeared to vary with the layer quality so that the error for their determination should be in the range of ± 0.1 eV. Nevertheless they can be attributed to transitions at the U and M points, the L and U and possibly from M, Γ or H points of the Brillouin zone according to recent theoretical calculations. The line shape of the dielectric function of MOVPE InN is in agreement with what was calculated in ab-initio theory.

One result from the InN growth experiments is the necessity of improved InN epilayers to determine the InN physical properties with high accuracy. Another one is the necessity of theory to achieve progress in crystal growth when publishing new predictions.

Of course this work is not a complete study of the III-nitrides epitaxial growth and many unsolved questions will remain. This includes the growth of thick epilayers of cubic materials such as $(\beta-)$InN and $(\beta-)$GaN where no reliable material studies are available up to now. Then a detailed investigation of AlN growth cannot be performed in the way as is done for GaN since the band gap position of AlN of 6.2 eV permits the observation of the electronic transitions during growth due to light absorption in the gas phase. Also the investigation in InN growth is only preliminary because research is still going on and the results presented here are part of work done together with M. Drago. In his thesis much more detailed growth investigations of InN MOVPE will be given.

Bibliography

[1] *Blu-Ray CD-ROM*, Sony Corp., presented at: Consumer Electronics CES2005, Nevada, USA.

[2] B. E. Foutz, S. K. O´Leary, M. S. Shur, and L. F. Eastman, Transient electron transport in wurtzite GaN, InN, and AlN, J. Appl. Phys. **85**(11), 7727–7734 (1999).

[3] M. A. Khan, M. S. Shur, J. N. Kuznia, J. Burm, and W. J. Schaff, Temperature activated conductance in GaN/AlGaN heterostructure field effect transistors operating at temperatures up to 300 °C, Appl. Phys. Lett. **66**, 1083–85 (1995).

[4] O. Briot, *Group III nitride semiconductor compounds - physics and applications*, Oxford science publications, ed. by B. Gil, 1st edition, 1997.

[5] H.Morkoç, *Nitride Semiconductors and Devices*, Springer, 1st edition, 1999.

[6] O. Ambacher, Growth and applications of group III-nitrides, J. Phys.D: Appl. Phys. **31**, 2653–2710 (1998).

[7] J. H. Edgar, *Properties of Group III Nitrides*, Electronic Materials Information Service (EMIS), 1994.

[8] S. Nakamura and G. Fasol, *The Blue Laser Diode - GaN Based Light Emitters and Lasers*, Springer Verlag Berlin-Heidelberg, ISBN 3-540-61590-3, 1997.

[9] S. Strite and H. Morkoç, GaN, AlN, and InN: a review, J. Vac. Sci. Technol. B **10**(4), 1237–1266 (1992).

[10] I. Akasaki, Progress in crystal growth of nitride semiconductors, J. Cryst. Growth **221**, 231–239 (2000).

[11] T. L. Tansley and C. P. Foley, Optical band gap of indium nitride, J. Appl. Phys. **9**, 3241 (1986).

[12] F. Bechstedt, J. Furthmüller, M. Ferhat, L. K. Teles, L. M. R. Scolfaro, J. R. Leite, V. Y. Davydov, O. Ambacher, and R. Goldhahn, Energy gap and optical properties of In$_x$Ga$_{1-x}$N, phys. stat. sol. (a) **195**(3), 628633 (2003).

[13] T. Matsuoka, H. Okamato, and M. Nakao, Growth of wurtzite InN in MOVPE and its optical characteristics, phys. stat. sol. (c) **0**(7), 2806–2809 (2003).

[14] K. L. Westra, R. P. W. Lawson, and M. J. Brett, The effects of oxygen contamination on the properties of reactively sputtered indium nitride films, J. Vac. Sci. Technol. A **6**(3), 1730 (1988).

[15] S. Kumar, L. Mo, Motlan, and T. L. Tansley, Elemental composition of reactively sputtered InN thin films, Jpn. J. Appl. Phys. **35**, 2261–2265 (1996).

[16] T. Yamaguchi, C. Morioka, K. Mizuo, M. Hori, T. Araki, and Y. Nanishi, Growth of InN and InGaN on Si substrate for solar cell applications, IEEE Proc. Int. Symp. Comp. Semicond. , 214–219 (2003).

[17] S. Nakamura, Analysis of real-time monitoring using interference effects, Jpn. J. Appl. Phys. **30**(7), 1348–1353 (1991).

[18] S. Nakamura, *In situ* Analysis of real-time monitoring using interference effects, Jpn. J. Appl. Phys. **30**(8), 1620–1627 (1991).

[19] *AIXTRON* company, "Aixtron 3000", http://www.aixtron.de/.

[20] M. Benamara, Z. Liliental-Weber, J. H. Mazur, W. Snider, and J. Washburn, The role of the multi buffer layer technique on the strain of GaN, Mat. Res. Soc. Symp. Proc. **595**, W5.8.1–6 (1999).

[21] P. Kung, D. Walker, M. Hamilton, J. Diaz, and M. Razeghi, Lateral epitaxial overgrowth of GaN films on sapphire and silicon substrates, Appl. Phys. Lett. **74**, 570 (1999).

[22] R. F. Davis, T. Gehrke, K. J. Linthicum, P. Rajagopal, A. M. Roskowski, T. Zheleva, E. A. Preble, C. A. Zorman, M. Mehregany, U. Schwarz, J. Schuck, and R. Grober, Review of pendeo-epitaxial growth and characterization of thin films of GaN and AlGaN alloys on 6H-SiC(0001) and Si(111) substrates, MRS Internet J. Nitride Semicond. Res. **6**(14) (2001).

[23] A. Strittmatter, S. Rodt, L. Reißmann, D. Bimberg, H. Schröder, E. Obermeier, T. Riemann, J. Christen, and A. Krost, Maskless epitaxial lateral overgrowth of GaN layers on structured Si(111) substrates, Appl. Phys. Lett. **78**, 727 (2001).

[24] A. Dadgar, A. Strittmater, J. Bläsing, M. Poschenrieder, O. Contreras, P. Veit, T. Riemann, F. Bertram, A. Reiher, A. Krtschil, A. Diez, T. Hempel, T. Finger, A. K. M. Schubert, D. Bimberg, F. A. Ponce, J. Christen, and A. Krost, Metal organic chemical vapor phase epitaxy of gallium-nitride on silicon, phys. stat. sol. (c) **0**(6), 1583–1606 (2003).

[25] U. W. Pohl, K. Knorr, and J. Bläsing, Metalorganic vapor phase epitaxy of GaN on LiGaO$_2$ substrates using tertiarybutylhydrazine, phys. stat. sol. (a) **184**(1), 117–120 (2001).

[26] A. G. Bhuiyan, A. Yamamoto, and A. Hashimoto, A novel two-step method for improvement of MOVPE grown InN film on GaP(111)B substrate, phys. stat. sol. (b) **228**(1), 27–30 (2001).

[27] DÁns-Lax, *Taschenbuch für Chemiker und Physiker, Band I*, Springer, Berlin, ed. by E. Lax and C. Synowietz, 1967.

[28] Y. Nanishi, Y. Saito, and T. Yamaguchi, RF-molecular beam epitaxy growth and properties of InN and related alloys, Jpn. J. Appl. Phys. **42**(5A), 2549–2559 (2003).

[29] S. Nakamura, GaN growth using GaN buffer layer, Jpn. J. Appl. Phys. **30**, L1705 (1991).

[30] Y. Park and D. Pavlidis, Mass Spectroscopy Study of GaN Metalorganic Chemical Vapor Deposition, J. Electron. Mat. **25**(9), 1554 (1996).

[31] V. S. Ban, Mass spectrometric studies of vapor-phase crystal growth, J. Electrochem. Soc. **119**, 761 (1972).

[32] M. Kamp, M. Mayer, A. Pelzmann, and K. J. Ebeling, Fundamentals, material properties and device performances in GaN MBE using on-surface cracking of ammonia, MRS Internet J. Nitride Semicond. Res. **2**(26) (1997).

[33] J. Karpinski, J. Jun, and S. Porowski, Equilibrium pressure of N$_2$ over GaN and high pressure solution growth od GaN, J. Cryst. Growth **66**, 1–10 (1984).

[34] E. D. Bourret-Courchesne, K.-M. Yu, S. J. C. Irvine, A. Stafford, S. A. Rushworth, L. M. Smith, and R. Kanjolia, MOVPE of GaN on sapphire using the alternate precursor 1,1-dimethylhydrazine for OMVPE growth, J. Electron. Mat. **221**, 246–250 (2000).

[35] U. W. Pohl, K. Knorr, C. Möller, U. Gernert, W. Richter, J. Bläsing, J. Christen, J. Gottfriedsen, and H. Schumann, Low-temperature Metalorganic vapor

phase epitaxy (MOVPE) of GaN using tertiarybutylhydrazine, Jpn. J. Appl. Phys. **38**(2A), 105–107 (1999).

[36] U. W. Pohl, C. Möller, K. Knorr, W. Richter, J. Gottfriedsen, H. Schumann, K. Rademann, and A. Fielicke, Tertiarybutylhydrazine: a new precursor for the MOVPE of group III-nitrides, Mat. Sci. Eng. **B59**, 20–23 (1999).

[37] S. Nishide, T. Yoshimura, Y. Takamatsu, A. Ishige, K. Pak, N. Ohshima, and H. Yonezu, Study of the pyrolysis of tertiarybutylhydrazine and GaN film growth, J. Cryst. Growth **189/190**, 325–329 (1998).

[38] E. D. Bourret-Courchesne, K.-M. Yu, S. J. C. Irvine, A. Stafford, S. A. Rushworth, L. M. Smith, and R. Kanjolia, MOVPE growth and luminescence properties of GaAsN alloys with higher nitrogen concentrations, phys. stat. sol. (a) **176**, 231–235 (1999).

[39] N. Y. Li, C. P. Hains, K. Yang, J. Lu, P. W. Li, and J. Cheng, Organometallic vapor phase epitaxy growth and optical characteristics of almost 1.2 μm GaInNAs three-quantum-well laser diodes, Appl. Phys. Lett. **75**(8), 1051–1054 (1999).

[40] Z. H. Lan, W. M. Wang, C. Sun, S. C. Shi, C. W. Hsu, T. T. Chen, K. H. Chen, C. C. Chen, Y. F. Chen, and L. C. Shen, Growth mechanism, structure and IR photoluminescence studies of InN nanorods, J. Cryst. Growth **269**, 87–94 (2004).

[41] W.-K. Chen, Y.-C. Pan, H.-C. Lin, J. Ou, W. H. Chen, and M.-C. Lee, Growth and X-ray characterization of an InN film on sapphire prepared by metalorganic vapor phase epitaxy, Jpn. J. Appl. Phys. **36**, L1625 (1997).

[42] W.-K. Chen, H.-C. Lin, Y.-C. Pan, J. Ou, C.-K. Shu, W. H. Chen, and M.-C. Lee, Raman and X-ray studies of InN films grown at different temperatures by metalorganic vapor phase epitaxy, Jpn. J. Appl. Phys. **37**, 4870 (1998).

[43] M. Sato, Epitaxial growth of InN by plasma-assisted metalorganic chemical vapor deposition, Jpn. J. Appl. Phys. **36**, L595–L597 (1997).

[44] M. Sato, Carrier density of epitaxial InN grown by plasma-assisted metalorganic chemical vapor deposition, Jpn. J. Appl. Phys. **36**, L658–L660 (1997).

[45] H. Lu, W. J. Schaff, J. Wang, H. Wu, W. Yeo, A. Pharkya, and L. F. Eastman, Improvement on epitaxial grown of InN by migration enhanced epitaxy, Appl. Phys. Lett. **77**(16), 2548 (2000).

[46] J. Aderhold, V. Y. Davydov, F. Fedler, H. Klausing, D. Mistele, T. Rotter, O. Semchinova, J. Stemmer, and J. Graul, InN thin films grown by metalorganic molecular beam epitaxy on sapphire substrates, J. Cryst. Growth **222**, 701–705 (2001).

[47] O. K. Semchinova, J. Aderhold, J. Graul, A. Filimonov, and H. Neff, Photoluminescence, depth profile, and lattice instability of hexagonal InN films, Appl. Phys. Lett. **83**(26), 5440 (2003).

[48] J. Wu, W. Walukiewicz, K. M. Yu, J. W. Ager, E. E. Haller, H. Lu, W. J. Schaff, Y. Saito, and Y. Nanishi, Unusual properties of the fundamental band gap of InN, Appl. Phys. Lett. **80**(21), 3967 (2002).

[49] V. Y. Davydov, A. A. Klochikhin, R. P. Seisyan, V. V. Emtsev, S. V. Ivanov, F. Bechstedt, J. Furthmüller, H. Harima, A. V. Mudryi, J. Aderhold, O. Semchinova, and J. Graul, Absorption and emission of hexagonal InN. Evidence of narrow fundamental band gap, phys. stat. sol. (b) **229**(3), R1–R3 (2002).

[50] A. Yamamoto, Y. Murakami, K. Koide, M. Adachi, and A. Hashimoto, Growth temperature dependences of MOVPE InN on sapphire substrates, phys. stat. sol. (b) **228**(1), 5–8 (2001).

[51] S. Keller, I. Ben-Yaacov, S. P. DenBaars, and U. K. Mishra, Flow modulation epitaxy of InN/GaN heterostructures; towards InN based HEMTs, Proc. Int. Workshop on Nitride Semiconductors (IWN2000), IPAP Conf. Series **1**, 233–236 (2000).

[52] O. Briot, B. Maleyre, and S. Ruffenach, Indium nitride quantum dots grown by metalorganic vapor phase epitaxy, Appl. Phys. Lett. **83**(14), 2919 (2003).

[53] T. Yodo, Y. Kitayama, K. Miyaki, H. Yona, Y. Harada, K. E. Prince, K. Scott, and A. Butcher, Visible emission near 1.9-2.2 eV from hexagonal InN films grown by electron cyclotron resonance plasma-assisted molecular-beam epitaxy, J. Cryst. Growth **269**, 145–154 (2004).

[54] H.-J. Kwon, Y.-H. Lee, O. Miki, H. Yamano, and A. Yoshida, Raman spectra of indium nitride thin films grown by microwave-excited metalorganic vapor phase epitaxy on (0001) sapphire substrates, Appl. Phys. Lett. **69**(7), 937 (1996).

[55] S. Yamaguchi, M. Kariya, S. Nitta, T. Takeuchi, C. Wetzel, H. Amano, and I. Akasaki, Structural properties of InN on GaN grown by metalorganic vapor-phase epitaxy, J. Appl. Phys. **85**(11), 7682 (1999).

[56] B. Maleyre, o. Briot, and S. Ruffenach, MOVPE growth of InN films and quantum dots, J. Cryst. Growth **269**, 15–21 (2004).

[57] A. R. Smith, V. Ramachandran, R. M. Feenstra, D. W. Grewe, A. Ptak, T. Myers, W. Sarney, L. Salamanca-Riba, M. Shin, and M. Skowronski, Surface reconstructions during molecular beam epitaxial growth of GaN(0001), MRS Internet J. Nitride Semicond. Res. **3**(12), 1–7 (1998).

[58] A. R. Smith, R. M. Feenstra, D. W. Grewe, M.-S. Shin, M. Skowronski, J. Neugebauer, and J. E. Northrup, GaN(0001) surface structures studied using scanning tunneling microscopy and first-principles total energy calculations, Surf. Sci. **423**, 70–84 (1999).

[59] A. R. Smith, R. M. Feenstra, D. W. Grewe, M. S. Shin, M. Skowronski, J. Neugebauer, and J. E. Northrup, Reconstructions of GaN(0001) and (000$\bar{1}$) surfaces: Ga-rich metallic structures, J. Vac. Sci. Technol. B **16**(4), 2242 (1998).

[60] A. R. Smith, R. M. Feenstra, D. W. Grewe, M.-S. Shin, M. Skowronski, J. Neugebauer, and J. E. Northrup, Determination of wurtzite GaN lattice polarity based on surface reconstruction, Appl. Phys. Lett. **72**(17), 2114 (1998).

[61] A. R. Smith, R. M. Feenstra, D. W. Grewe, J. Neugebauer, and J. E. Northrup, Reconstructions of the GaN [000$\bar{1}$] surface, Phys. Rev. Lett. **79**, 3934 (1997).

[62] R. M. Feenstra, Review of structure of bare and adsorbate-covered GaN(0001) surfaces, MRS Internet J. Nitride Semicond. Res. **7**(3), 1–39 (2002).

[63] E. S. Hellmann, The polarity of GaN: a critical review, MRS Internet J. Nitride Semicond. Res. **3**(11) (1998).

[64] M. J. Murphy, B. E. Foutz, K. Chu, H. Wu, W. Yeo, W. J. Schaff, O. Ambacher, L. F. Eastman, T. J. Eustis, R-Dimitrov, M. Stutzmann, and W. Rieger, Normal and inverted AlGaN/GaN based piezoelectric field effect transistors grown by plasma induced molecular beam epitaxy, MRS Internet J. Nitride Semicond. Res. **4S1**(G8.4) (1999).

[65] T. Sasaki and T. Matsuoka, Substrate-polarity dependence of metal-organic vapor-phase epitaxy-grown GaN on SiC, J. Appl. Phys. **64**, 4531 (1988).

[66] M. AsifKhan, J. N. Kuznia, D. T. Olson, and R. Kaplan, Deposition and surface characterization of high quality single crystal GaN layers, J. Appl. Phys. **73**, 3108 (1993).

[67] M. Seelmann-Eggebert, J. L. Weyher, H. Obloh, H. Zimmermann, A. Rar, and S. Porowski, Polarity of (00.1) GaN epilayers grown on a (00.1) sapphire, Appl. Phys. Lett. **71**(18), 2635–2637 (1997).

[68] F. A. Ponce, C. G. VandeWalle, and J. E. Northrup, Atomic arrangement at the AlN/SiC interface, Phys. Rev. B **53**, 7473–7478 (1996).

[69] F. A. Ponce, D. P. Bour, W. T. Young, M. Saunders, and J. W. Steeds, Determination of lattice polarity for growth of GaN bulk single crystals and epitaxial layers, Appl. Phys. Lett. **69**(3), 337 (1996).

[70] M. Sumiya, K. Yoshimura, N. Ogusu, S. Fuke, K. Mizuno, M. Yoshimoto, H. Koinuma, and L. T. Romano, Effect on buffer-layer engineering on the polarity of GaN films, J. Vac. Sci. Technol. A **20**(2), 456 (2002).

[71] B. Daudin, J. L. Rouvière, and M. Arlery, The key role of polarity in the growth process of (0001) nitrides, Mat. Sci. Eng. **B43**, 157–160 (1997).

[72] N. Grandjean, J. Massies, Y. Martinez, P. Vennegues, M. Leroux, and M. Laugt, GaN epitaxial growth on sapphire (0001): the role of the substrate nitridation, J. Cryst. Growth **178**(3), 220 (1997).

[73] R. Held, G. Nowak, B. E. Ishaug, S. M. Seutter, A. Parkhomovski, A. M. Dabiran, P. I. Cohen, I. Grzegory, and S. Porowski, Structure and composition of GaN(0001) A and B surfaces, J. Appl. Phys. **85**(11), 7697 (1999).

[74] J. Neugebauer, T. Zywietz, M. Scheffler, and J. Northrup, Theory of surfaces and interfaces of group III-nitrides, Appl. Surf. Sci. **159-160**, 355–359 (2000).

[75] T. Zywietz, J. Neugebauer, M. Scheffler, J. Northrup, and C. G. Van de Walle, Surface structures, surfactants and diffusion at cubic and wurtzite GaN, MRS Internet J. Nitride Semicond. Res. **3**(26) (1998).

[76] Q. K. Xue, Q. Z. Xue, S. Kuwano, T. Sakurai, T. Ohno, I. S. T. Tsong, X. G. Qiu, and Y. Segawa, Imaging wurtzite GaN surfaces by molecular beam epitaxy-scanning tunneling microscopy, Thin Solid Films **367**, 149–158 (2000).

[77] P. Vogt, *Atomic structure of the (001) surfaces of InP, GaP and InGaP*, PhD thesis, TU Berlin, 2003.

[78] C. Meyne, *Optische in-situ Untersuchungen zum Quantenpunkt-Wachstum von II-VI-Halbleitern in der Metallorganischen Gasphasenepitaxie*, PhD thesis, TU Berlin, 2002.

[79] J.-T. Zettler, Characterization of epitaxial semiconductor growth by reflectance anisotropy spectroscopy and ellipsometry, Prog. Cryst. Growth Charact. Mat. **35**, 27 (1997).

[80] D. E. Aspnes, Characterisation of semiconductors and semiconductor structures by photometric and ellipsometric techniques, in *Proc. SPIE: International conference on physical concepts of materials for novel Optoelectronic device applications*, 1990.

[81] U. Rossow, N. V. Edwards, M. D. Bremser, R. S. Kern, H. Liu, R. F. Davis, and D. E. Aspnes, In-plane optical anisotropies of $Al_xGa_{1-x}N$ films in their regions of transparency, Mat. Res. Soc. Symp. Proc. , 835–840 (1997).

[82] H. Na, H. J. Kim, S. Y. Kwon, E. Yoon, Y. Moon, and M. H. Kim, In-situ, real-time spectral reflectance monitoring of GaN growth, J. Korean Phys. Soc. **37**(6), 971 (2000).

[83] N. Kobayashi and Y. Kobayashi, In-situ optical monitoring of surface morphology and stoichiometry during GaN metal organic vapor phase epitaxy, Appl. Surf. Sci. **159-160**, 398–404 (2000).

[84] N. Kobayashi and Y. Kobayashi, SPA monitoring of GaN MOVPE surface, Mat. Res. Soc. Symp. Proc. , II 2.2 (1997).

[85] R. D. L. Kronig, On the theory of dispersion of X-rays, J. Opt. Soc. Am. + Rev. Sci. Instr. **12**(6), 547–557 (1926).

[86] R. M. A. Azzam and N. M. Bashara, *Ellipsometry and Polarized Light*, North-Holland personal library, Elsevier Science B.V. Amsterdam, 1977.

[87] P. Drude, Ueber Oberflächenschichten, Ann. Phys. Chem. **36**, 532–560, 865–877 (1889).

[88] S. Peters, *VUV Spektroskopische Ellipsometrie zur Charakterisierung von Gruppe-III-Nitriden und in-situ Wachstumsuntersuchung*, PhD thesis, TU Berlin, t.b.p., 2006.

[89] P. Y. Yu and M. Cardona, *Fundamentals of Semiconductors*, Springer Verlag, 2nd edition, 1999.

[90] L. vanHowe, The occurrence of singularities in the elastic frequency distribution of a crystal, Phys. Rev. **89**(6), 1189–1193 (1953).

[91] T. Wethkamp, *Optical properties of group-III-nitrides in the visible to vacuum-ultraviolet spectral range investigated by spectroscopic ellipsometry*, PhD thesis, TU Berlin, 1999.

[92] L. X. Benedict, *Ab initio* calculation of $\epsilon_2(\omega)$ including the electron-hole interaction: Application to GaN and CaF_2, Phys. Rev. B **59**(8), 5441–5451 (1999).

[93] L. X. Benedict, T. Wethkamp, K. Wilmers, C. Cobet, N. Esser, E. L. Shirley, W. Richter, and M. Cardona, Dielectric function of wurtzite GaN and AlN thin films, Sol. State Commun. **112**(3), 129–133 (1999).

[94] M. Cardona, *Modulation Spectroscopy*, Solid State Physics, Suppl. 11, Academic Press, New York, 1969.

[95] M. L. Cohen, Ultraviolet optical properties and electronic band structure of magnesium oxide, Phys. Rev. **155**(3), 992 (1967).

[96] Bergmann and Schäfer, *Lehrbuch der Experimentalphysik, Bd. 3, Optik*, de Gruyter, Berlin, New York, 1993.

[97] M. Born and E. Wolf, *Principles of Optics*, Pergamon Press, Oxford, 1987.

[98] E. Palik, editor, *Handbook of Optical Constants of Solids I*, Academic Press, Inc., San Diego, 1985.

[99] E. Palik, editor, *Handbook of Optical Constants of Solids II*, Academic Press, Inc., San Diego, 1991.

[100] F. S. Ohuchi and R. H. French, Summary abstract: effect of oxygen incorporation in AlN thin films, J. Vac. Sci. Technol. A **6**(3), 1695 (1987).

[101] C. Tanguy, Optical dispersion by wannier excitons, Phys. Rev. Lett. **22**, 4090 (1995).

[102] C. Tanguy, Refractive index of direct bandgap semiconductors near the absorption threshold: influence of excitonic effects, IEEE Journal of Quantum Electronics **32**(10), 1746 (1996).

[103] A. Röseler, *Infrared Spectroscopic Ellipsometry*, Akademie Verlag, Berlin, 1990.

[104] D. A. G. Bruggemann, Berechnung verschiedener physikalischer Konstanten von heterogenen Substanzen, Ann. Phys. (Leipzig) **24**, 636 (1935).

[105] U. Rossow, G. Bauer, and W. Richter, editors, *Optical Characterization of Epitaxial Semiconductor Layers*, Springer-Verlag, Berlin, 1996.

[106] T. Trepk, *Optical properties of III-V semiconductors at high temperatures*, PhD thesis, TU Berlin, 2005.

[107] I. Akasaki, H. Amano, Y. Koide, H. Hiramatsu, and N. Sawaki, Effects of AlN buffer layer on crystallographic structure and on electrical and optical properties of GaN and $Ga_{1-x}Al_xN$ ($0 < x \leq 0.4$) films grown on sapphire substrate by MOVPE, J. Cryst. Growth **98**(1-2), 209 (1989).

[108] H. Amano, N. Sawaki, I. Akasaki, and Y. Toyoda, Metalorganic vapor phase epitaxial growth of a high quality GaN film using an AlN buffer layer, Appl. Phys. Lett. **48**, 353 (1986).

[109] A. Munkholm, C. Thompson, C. M. Foster, J. A. Eastman, O. Auciello, G. B. Stephenson, P. Fini, S. P. DenBaars, and J. S. Speck, Determination of the cubic to hexagonal fraction in GaN nucleation layers using grazing incidence x-ray scattering, Appl. Phys. Lett. **72**(23), 2972–2974 (1998).

[110] X. H. Wu, D. Kapolnek, E. J. Tarsa, B. Heying, S. Keller, B. P. Keller, U. K. Mishra, S. P. DenBaars, and J. S. Speck, Nucleation layer evolution in metal-organic chemical vapor deposition grown GaN, Appl. Phys. Lett. **10**(4), 1371 (1996).

[111] X. H. Wu, P. Fini, S. Keller, E. J. Tarsa, B. Heying, U. K. Mishra, S. P. DenBaars, and J. S. Speck, Morphological and structural transitions in GaN films grown on sapphire by metal-organic chemical vapor deposition, Jpn. J. Appl. Phys. **35**, L1648 (1996).

[112] X. H. Wu, P. Fini, E. J. Tarsa, B. Heying, S. Keller, U. K. Mishra, S. P. DenBaars, and J. S. Speck, Dislocation generation in GaN heteroepitaxy, J. Cryst. Growth **189/190**, 231–243 (1998).

[113] L. Cheng, G. Zhang, D. Yu, and Z. Zhang, Alternative microstructure of GaN nucleation layers grown by low pressure metal-organic vapor phase epitaxy on sapphire substrate, Appl. Phys. Lett. **70**(11), 1408–1410 (1997).

[114] M. S. Yi, H. H. Lee, D. J. Kim, S. J. Park, D. Y. Noh, C. C. Kim, and J. H. Je, Effects of growth temperature on GaN nucleation layers, Appl. Phys. Lett. **75**(15), 2187 (1999).

[115] M. Lada, A. G. Cullis, and P. J. Parbrook, Effect of anneal temperature on GaN nucleation layer transformation, J. Cryst. Growth **258**, 89–99 (2003).

[116] L. Sugiura, K. Itaya, J. Nishio, H. Fujimoto, and Y. Kokubun, Effects of thermal treatment of low-temperature GaN buffer layers on the quality of subsequent GaN layers, J. Appl. Phys. **82**(10), 4877 (1997).

[117] S. Fuke, H. Teshigawara, K. Kuwahara, Y. Takano, T. Ito, M. Yanagihara, and K. Ohtsuka, Influences of initial nitridation and buffer layer deposition on the morphology of a (0001) GaN layer grown on sapphire substrate, J. Appl. Phys. **83**(2), 764 (1998).

[118] K. Uchida, A. Watanabe, F. Yano, M. Kouguchi, M. Tanaka, and S. Minagawa, Nitridation process of sapphire substrate surface and its effect on the growth of GaN, J. Appl. Phys. **79**(7), 3487 (1996).

[119] S. Keller, B. P. Keller, Y. F. Wu, B. Heying, D. Kapolnek, J. S. Speck, U. K. Mishra, and S. P. DenBaars, Influence of sapphire nitridation on properties of GaN grown by metal organic chemical vapor deposition, Appl. Phys. Lett. **68**(11), 1525–1527 (1996).

[120] F. Degave, P. Ruterana, G. Nouet, J. H. Je, and C. C. Kim, Nucleation of GaN on (0001) sapphire during MOCVD growth: an atomic force and high resolution electron microscopy study, Mat. Res. Soc. Symp. Proc. **639**, G.3.41.1 (2001).

[121] F. Demangeot, M. A. Renucci, J. Frandon, and O. Briot, GaN layer growth in relation to buffer deposition temperature, Mat. Sci. Eng. **B43**, 246–249 (1997).

[122] T. Ito, M. Sumiya, Y. Takano, K. Ohtsuka, and S. Fuke, Influence of thermal annealing on GaN buffer layers and the property subsequent GaN layers grown by metal organic vapor deposition, Jpn. J. Appl. Phys. **38**, 649–653 (1999).

[123] A. E. Wickenden, D. K. Wickenden, and T. J. Kistenmacher, The effect of thermal annealing on GaN nucleation layers deposited on (0001) sapphire by metal organic chemical vapor deposition, J. Appl. Phys. **75**(10), 5367 (1994).

[124] G. Koblmüller, P. Pongratz, R. Averbeck, and H. Riechert, Delayed nucleation during molecular beam epitaxial growth of GaN observed by line-of-sight quadrupole mass spectroscopy, Appl. Phys. Lett. **80**(13), 2281 (2002).

[125] C. Heinlein, J. P. Grepstad, S. Einfeldt, D. Hommel, T. Berge, and A. P. Grande, Preconditioning of c-plane sapphire for GaN molecular beam epitaxy by electron cyclotron resonance plasma nitridation, J. Appl. Phys. **83**, 6023 (1998).

[126] M. Yeadon, M. T. Marshall, F. H. S. Pekin, H. Morkoc, and J. M. Gibson, In-situ observation of AlN formation during nitridation of sapphire by ultrahigh vacuum transmission electron microscopy, Mat. Res. Soc. Symp. Proc. , 99–104 (1998).

[127] M. E. Twigg, D. Koleske, A. Wickenden, R. L. Henry, and S. C. Binari, Correlation between nucleation layer structure, dislocation density and electrical resistivity for GaN films grown on a-plane sapphire by metal organic vapor phase epitaxy, Appl. Phys. Lett. **79**(26), 4322 (2001).

[128] S. Figge, T. Böttcher, S. Einfeldt, and D. Hommel, In-situ and ex-situ evaluation of the film coalescence for GaN growth on GaN nucleation layers, J. Cryst. Growth **221**, 262–266 (2000).

[129] D. D. Koleske, M. E. Coltrin, A. A. Allerman, K. C. Cross, C. C. Mitchell, and J. J. Figiel, *In situ* measurements of GaN nucleation layer decomposition, Appl. Phys. Lett. **82**(8), 1170–1172 (2003).

[130] D. D. Koleske, M. E. Coltrin, K. C. Cross, C. C. Mitchell, and A. A. Allerman, Understanding GaN nucleation layer evolution on sapphire, J. Cryst. Growth **273**, 86–99 (2004).

[131] M. H. Kim, C. Sone, J. H. Yi, and E. Yoon, Changes in the growth mode of low temperature GaN buffer layers with nitrogen plasma nitridation of sapphire substrates, Appl. Phys. Lett. **71**, 1228 (1997).

[132] T. Hashimoto, Y. Terakoshi, M. Yuri, M. Ishida, O. Imafuji, T. Sugino, and K. Itoh, Quantitative study of nitridated sapphire surfaces by x-ray photoelectron spectroscopy, J. Appl. Phys. **86**(7), 3670 (1999).

[133] K. S. Kim, C. S. Oh, K. J. Lee, G. M. Yang, C. H. Hong, K. Y. Lim, and H. J. Lee, Effects of growth rate of a GaN buffer layer on the properties of GaN on a sapphire substrate, J. Appl. Phys. **83**(12), 8441 (1999).

[134] M. Muñoz, Y. S. Huang, F. H. Pollack, and H. Yang, Optical constants of cubic GaN/GaAs(001): experiment and modeling, J. Appl. Phys. **93**(5), 2549 (2003).

[135] S. Keller, D. Kapolnek, B. P. Keller, Y. Wu, B. Heying, J. S. Speck, U. K. Mishra, and S. P. DenBaars, Effect of the trimethylgallium flow during nucleation layer growth on the properties of GaN grown on sapphire, Jpn. J. Appl. Phys. **35**, L285–L288 (1996).

[136] X. H. Wu, L. M. Brown, D. Kapolnek, S. Keller, B. Keller, S. P. DenBaars, and J. S. Speck, Defect structure of metal-organic chemical vapor deposition-grown epitaxial (0001)GaN/Al$_2$O$_3$, J. Appl. Phys. **80**(6) (1996).

[137] Y. P. Varshni, Temperature dependence of the energy gap in semiconductors, Physica **34**, 149–154 (1967).

[138] S. Logothetidis, J. Petalas, M. Cardona, and T. D. Moustakas, Optical properties and temperature dependence of the interband transitions of cubic and hexagonal GaN, Phys. Rev. B **50**(24), 18017–18028 (1994).

[139] C.-H. Su, W. Paöosz, S. Zhu, S. L. Lehozcky, I. Grzegory, P. Perlin, and T. Suski, Energy gap in GaN bulk single crystal between 293 and 1237 K, J. Cryst. Growth **235**, 111–114 (2002).

[140] A. V. Rodina, M. Dietrich, A. Göldner, L. Eckey, A. Hoffmann, A. L. Efros, M. Rosen, and B. K. Meyer, Free excitons in wurtzite GaN, Phys. Rev. B **64**, 115204–1 (2001).

[141] M. A. Reshchikov and H. Morkoç, Luminescence properties of defects in GaN, Appl. Phys. Lett. **97**, 061301 (2005).

[142] F. Poser, *Stickstoffeinbau in GaAs - Eigenschaften und Charakterisierung des Wachstums in der Metallorganischen Gasphasenepitaxie*, PhD thesis, TU Berlin, 2005.

[143] T. Schmidtling, M. Klein, U. W. Pohl, and W. Richter, Metal organic vapor phase epitaxy of GaAsN/GaAs Quantum wells using Tertiarybutylhydrazine, MRS Internet J. Nitride Semicond. Res. **5S1**, W3.43 (2000).

[144] G. B. Stringfellow, *Organometallic Vapor-Phase Epitaxy: Theory and Practice*, Academic Press, Inc., 2nd edition, 1999.

[145] S. Nakamura and T. Mukai, High-quality InGaN films grown on GaN films, Jpn. J. Appl. Phys. **31**, L1457–59 (1992).

[146] A. Koukitu, N. Takahashi, T. Taki, and H. Seki, Thermodynamic analysis of the MOVPE growth of $In_xGa_{1-x}N$, J. Cryst. Growth **170**, 306–311 (1997).

[147] F. Scholz, V. Haerle, F. Steuber, H. Bolay, A. Dornen, B. Kaufmann, V. Syganov, and A. Hangleiter, Low pressure MOVPE of GaN and and GaInN/GaN heterostructures, J. Cryst. Growth **170**, 321–324 (1997).

[148] A. Munkholm, C. Thompson, J. A. Eastman, G. B. Stephenson, P. Fini, J. S. Speck, O. Auciello, P. H. Fuoss, and S. P. DenBaars, Surface structure of GaN (0001) in the chemical vapor deposition environment, Phys. Rev. Lett. **83**(4), 741–744 (1999).

[149] A. Munkholm, C. Thompson, G. B. Stephenson, J. A. Eastman, O. Auciello, P. Fini, J. S. Speck, and S. P. DenBaars, Transition between the $1{\times}1$ and $\left(\sqrt{3}\times 2\sqrt{3}\right)$R30° surface structures of GaN in the vapor-phase environment, Physica B **283**, 217–223 (2000).

[150] Y. Kobayashi, T. Akasaki, and N. Kobayashi, Thermal stability of low-temperature GaN and AlN layers during metal organic vapor phase epitaxy monitored by *in situ* shallow-angle reflectance using ultraviolet light, Jpn. J. Appl. Phys. **37**(10B), L 1208–L 1210 (1998).

[151] N. Kobayashi, Surface photoabsorption monitoring of $III - V$ and $GaN MOVPE$ surfaces, J. Cryst. Growth **195**, 228–233 (1998).

[152] Y. Kobayashi and N. Kobayashi, Influence of N_2 carrier gas on surface stoichiometry in GaN MOVPE studied by surface photoadsorption, J. Cryst. Growth **189-190**, 301–304 (1998).

[153] J. E. Northrup, R. DiFelice, and J. Neugebauer, Energetics of H and $NH-_2$ on GaN(10-10) and implications for the origin of nanopipe defects, Phys. Rev. B **56**(8), R4325 (1997).

[154] C. G. Van de Walle and J. Neugebauer, First-principle surface phase diagram for hydrogen on GaN surfaces, Phys. Rev. Lett. **88**(6), 066103–1 (2002).

[155] M. Zorn, *Optical in-situ studies and on-line growth control of binary and ternary semiconductors with respect to the (001) surface*, PhD thesis, TU Berlin, 1999.

[156] K. Prabhakaran, T. G. Andersson, and K. Nozawa, Nature of native oxide on GaN surface and its reaction with Al, Appl. Phys. Lett. **69**(21), 3213–3214 (1996).

[157] J. L. Margrave, editor, *The Characterization of High-Temperature Vapors*, John Wiley & Sons, New York, 1967.

[158] R. E. Honig and D. A. Kramer, Vapor Pressure Data for the Solid and Liquid Elements, RCA Review **30**, 285–305 (1969).

[159] R. W. Collins and K. Vedam, Optical Properties of Solids, Encycl. of Appl. Phys. **12**, 285–336 (1995).

[160] M. Drago, *MOVPE of InN with spectroscopic ellipsometry in situ control*, PhD thesis, TU Berlin, to be published, 2006.

[161] A. G. Bhuiyan, A. Hashimoto, and A. Yamamoto, Indium nitride (InN): A review on growth, characterisation and properties, J. Appl. Phys. **94**(5), 2779–2808 (2003).

[162] R. Goldhahn, S. Shokhovets, V. Cimalla, L. Spiess, G. Ecke, O. Ambacher, J. Furthmüller, F. Bechstedt, H. Lu, and W. J. Schaff, Dielectric function of

"narrow" band gap InN, Mat. Res. Soc. Symp. Proc. **743**, L.5.9.1 – L.5.9.6 (2003).

[163] A. Jain and J. M. Redwing, Study of the growth mechanism and properties of InN films grown by MOCVD, Mat. Res. Soc. Symp. Proc. **798**, Y12.8.1–Y12.8.6 (2004).

[164] A. Jain, S. Raghavan, and J. M. Redwing, Evolution of surface morphology and film stress during MOCVD growth of InN on sapphire substrates, J. Cryst. Growth **269**, 128–133 (2004).

[165] G. Kaczmarczyk, A. Kaschner, S. Reich, A. Hoffmann, C. Thomsen, D. J. As, A. P. Lima, D. Schikora, K. Lischka, R. Averbeck, and H. Riechert, Lattice dynamics of hexagonal and cubic InN: Raman scattering experiments and calculations, Appl. Phys. Lett. **76**, 2122 (2000).

[166] V. Y. Davydov, V. V. Emtsev, I. N. Goncharuk, A. N. Smirnov, V. D. Petrikov, V. V. Mamutin, V. A. Vekshin, S. V. Ivanov, M. B. Smirnov, and T. Inushima, Experimental and theoretical studies of phonons in hexagonal InN, Appl. Phys. Lett. **75**(21), 3297–3299 (1999).

[167] M. Drago, T. Schmidtling, U. W. Pohl, S. Peters, and W. Richter, InN metalorganic vapour phase epitaxy and ellipsometric characterisation, phys. stat. sol. (c) **0**, 2842 (2003).

[168] M. Drago, C. Werner, T. Schmidtling, U. W. Pohl, and W. Richter, InN Growth and Annealing Investigations using in-situ Spectroscopic Ellipsometry, J. Cryst. Growth **272**, 87 (2004).

[169] M. Drago, P. Vogt, and W. Richter, MOVPE growth of InN with ammonia on sapphire, subm. to phys. stat. sol. (c) , Conf. Proc. of E–MRS Fall, Warszawa.

[170] M. Drago, C. Werner, M. Pristovsek, U. W. Pohl, and W. Richter, Development of InN metalorganic vapor phase epitaxy using in-situ spectroscopic ellipsometry, Cryst. Res. and Tech. , in print (2005).

[171] M. Drago, C. Werner, M. Pristovsek, U. W. Pohl, and W. Richter, InN growth on sapphire using different nitridation procedures, subm. to phys. stat. sol. (c) , Conf. Proc. of ICNS–6, Bremen (2006).

[172] M. R. Phillips, M. H. Zareie, O. Gelhausen, M. Drago, T. Schmidtling, and W. Richter, Scanning tunneling and cathodoluminescence spectroscopy of indium nitride, J. Cryst. Growth **269**, 106 (2004).

[173] A. B. Djurišić and E. H. Li, Modeling the optical constants of hexagonal GaN, InN, and AlN, J. Appl. Phys. **85**(5), 2848–2853 (1999).

[174] D. Fritsch, H. Schmidt, and M. Grundmann, Band dispersion relations of zinc-blende and wurtzite InN, Phys. Rev. B **69**, 165204 (2004).

[175] Q. Guo and A. Yoshida, Temperature dependence of band gap change in InN and AlN, Jpn. J. Appl. Phys. **33**(5), 2453–2456 (1994).

[176] V. Y. Davydov, A. A. Klochikhin, V. V. Emtsev, S. V. Ivanov, V. V. Vekshin, F. Bechstedt, J. Furthmüller, H. Harima, A. V. Mudryi, A. Hashimoto, A. Yamamoto, J. Aderhold, J. Graul, and E. E. Haller, Band gap of InN and In-rich $In_xGa_{1-x}N$ alloys (0.36<x<1), phys. stat. sol. (b) **230**(2), R4–R6 (2002).

[177] M. Kuball, J. W. Pomeroy, M. Wintrebert-Fouquet, K. S. A. Butcher, H. Lu, and W. J. Schaff, A raman spectroscopy study of InN, J. Cryst. Growth **269**, 59–65 (2004).

[178] T. Matsuoka, H. Okamato, M. Nakao, H. Harima, and E. Kurimoto, Optical bandgap energy of wurtzite InN, Appl. Phys. Lett. **81**(7), 1246–1248 (2002).

[179] S. Zollner, Model dielectric functions for native oxides on compound semiconductors, Appl. Phys. Lett. **63**(18), 2523–2524 (1993).

[180] E. Kurimoto, M. Hangyo, H. Harima, M. Yoshimoto, T. Yamaguchi, T. Araki, Y. Nanishi, and K. Isoda, Spectroscopic observation of oxidation process in InN, Appl. Phys. Lett. **84**(2), 212–214 (2004).

[181] O. Briot, B. Maleyre, S. Ruffenach, B. Gil, C. Pinquier, F. Demangeot, and J. Frandon, Absorption and raman scattering processes in InN films and dots, J. Cryst. Growth **269**, 22–28 (2004).

List of Figures

List of Tables

Acknowledgements

This page is mainly dedicated to Prof. Richter and his group. It was a pleasure to work with and for all of them supporting anyone who was in trouble.

In the long (unsorted !) list of all those who contributed to this work some should not forgotten to be mentioned, especially:

Prof. Dr. M. Kneissl who rapidly agreed to report on my thesis,

Dr. Patrick Vogt whose engaged work on the properties of group-III phosphorus containing semiconductors enabled the experimental MBE setup for the successful GaN (PA)MBE surface experiments and who also enforced me to write this thesis in TeX,

Pello (Dr. Christian Meyne) for the wonderful experimental variety he brought into the lab mostly ending up with wrenches and screwdrivers spread around,

Dr. Florian Poser for the immediate PC-support whenever he saw my eyebrows starting to lift up while staring at the screen and for several famous cycling events ("Vatertagstouren"),

Dr. Karsten Fleischer for the Raman-support and teaching me not to think only in windows,

Dr. Christoph Cobet for the (PA)MBE X-Mas evenings,

Dottore Massimo Drago for radiating italian flair with "spaghetti carbonara" and unexpectedly keeping the VP50RP alive and in best condition,

Prissi (Dr. Markus Pristovsek) for the steady signal overload he produced,

and all of them (including those which are not mentioned explicitly here) for the steady physical input and the discussions either during lunch or late at night.
That's the way science should be!

Last but not least I have to thank my whole family for supporting me and the DFG for financing the Sfb 296 and some of my money.